Development of Asymmetric-Order Approximated Analytical Model of Vegetation Isoline for Satellite Remote Sensing of Land Surface

by

Munenori Miura

A dissertation submitted in partial fulfillment
of the requirements for the degree of
Doctor of Philosophy
(Information Science and Technology)
in Aichi Prefectural University
2020

Doctoral Committee:

Professor Hiroki Yoshioka, Chair
Professor Kazuhito Murakami
Professor Naohiro Toda

ACKNOWLEDGEMENTS

I would like to express my sincere gratitude to my advisor Dr. Hiroki Yoshioka for guiding my work and preparing many opportunities through which my skills in learning, teaching and leading as well as researching are enhanced comprehensively. Appreciation on his efforts for my experiences and skill developments is absolutely beyond description. Special thanks are due to two co-chairmans, Dr. Kazuhito Murakami and Dr. Naohiro Toda for their enthusiastic efforts for reviewing my research. I would like to thank Dr. Kenta Obata who contributed since beginning of this research. Finally, I am deeply grateful to my family for their support and encouragement.

TABLE OF CONTENTS

CHAPTER

LIST OF FIGURES

Figure

LIST OF TABLES

<u>**Table**</u>

ABSTRACT

The first-order vegetaion isoline equation has been utilized for various purposes that involve retrieval of biophysical parameters. Although the simplicity of its derivation results in usability and applicability, the derived formulation suffers from errors when the brightness of soil layer located under the canopy becomes high. These errors are caused by truncation of the second- and higher-order interaction terms that represent photon interactions between the canopy layer and the soil surface. In order to meet accuracy criteria posed generally to satellite data products, these errors must be reduced considerably. The objective of this study is to improve the accuracy of vegetation isoline equations without sacrificing its simplicity. To achieve the objective, this study takes three steps: derivation of vegetation isoline equation with higher-order interaction term, optimization of the derived isoline equation, and extension of wavelength combination.

The derivation of a new isoline expression was carried out by including the second-order interaction term in a context of red and near-infrared (NIR) reflectance subspace. In this study, the second-order interaction term was, however, considered only in the NIR wavelength, instead of including in both the red and NIR wavelengths. This 'asymmetric' form of second-order approximation resulted in error reduction considerably comparing to the first-order vegetation isoline equation. This study also investigated the mechanism that brings accuracy improvement of the asymmetric-order vegetation isoline equation. It was found that the asymmetrical inclusion of the second-order interaction term only in the NIR wavelengths, shifts the approximated reflectance spectra favorably. The resulted approximated spectra becomes much closer to the true vegetation isoline than the symmetrical case due to an over correction effect of the reflectance in the NIR wavelength. This study further validated this finding by numerical experiments with a radiative transfer model. As a result, the error in the asymmetric approximation is reduced to one fifth of the first-order vegetation isoline equation.

As the second step of this study, the optimization was attempted by introducing a single factor into the derived asymmetric-order vegetation isoline equation. This factor was adjusted to minimize root mean square error over the ranges of input parameters based on the radiative transfer model. The numerical experiments also

revealed that the errors in the optimized asymmetric-order vegetation isoline equation were reduced in magnitude to nearly 1/25 of the errors obtained from the first-order vegetation isoline equation, and to nearly one-fifth of the error obtained from the non-optimized (original) asymmetric-order vegetation isoline equation. The errors in the optimized asymmetric-order isoline were compared with the magnitudes of the signal-to-noise ratio (SNR) of four existing sensors aboard the Earth observation satellites. These results indicated that the error in the asymmetric isoline could be reduced to the level of the SNR by adjusting the factor.

Finally, the derivation of the asymmetric-order vegetation isoline was extended to the combinations of wavelength other than the red and NIR. The extended range of wavelength investigated in this study was from 400 nm to 1200 nm. The optimum value of the factor introduced in the previous step was numerically determined in the same procedure. The results indicated that the value of the optimization factor is not constant over the range: It varies significantly by the combination of two wavelengths. Although the accuracy of the asymmetric-order vegetation isoline before optimization became even lower than the first-order vegetation isoline in certain combinations of wavelength, the use of the optimization factor results in high accuracy for the entire wavelength range. It was concluded that the newly derived vegetation isoline can achieve accuracy hight enough for the use of various applications comparing to the level of SNR of existing sensors. Further studies will be needed to identify the accuracy of the retrieved biophysical parameters such as leaf area index by the derived vegetation isolines.

CHAPTER I

Introduction

1.1 Global Environmental Issues

In 2013, Intergovernmental Panel on Climate Change (IPCC) reported that the global warming of the Ecosystem is not a doubtful issue any longer [1]. The report also indicated that the dominant factor of the global warming is the influence of the human activity, which would consequently raise the global average temperature to 0.3°C∼ 4.8°C by the end of this century. If the global warming continues at the current rate, the climate or weather reaches to the level such that the human society suffers from its influence through the temperature rising, the ocean surface rising, and the acidification of ocean water. Since the accumulated total emissions of the greenhouse gas for the cause of global warming is proportional to the rising of global average temperature, the future temperature level is heavily depended on the accumulated total amount of greenhouse gas emission [1–4]. In order to act and react to these global events, the level of the greenhouse gas emission should be monitored precisely where the satellite remote sensing plays a major roll [5].

The Earth observation organization was established to address important issues about Earth observation, namely, global environment change by human activity, their influences on the climate change, and improvement of prediction accuracy of the climate change. For example, greenhouse gas has been observed continuously to understand the relation between the influence of greenhouse gas and global warming. For those purposes, the amount of carbon absorption and exhalation from land surface needs to be accurately estimated in global scale, where the satellite remote sensing plays an important role. Among many observation targets, the carbon absorption, exhalation, and accumulation by vegetation and soil have been considered as hight priority target. These must be observed continuously for better understanding and ultimately for better management of its functional role in the global working [6].

1.2 Trend of Earth Observation Satellites

The Earth observation by satellite remote sensing began in early 1970's. It has been mainly carried out by large size and hence heavy satellites. The remote sensing has been accelerated dramatically since 1980's. Figure1.1 summarizes the major Earth observation satellites used for Earth observation and their operation terms. Considering the weights of Earth observation satellites, the Landsat series lunched in 1973 was approximately one ton. It increases to nearly three times, 2.8 tons, in 2013 for the latest predecessor Landsat-8. This trend has continued until the Terra and Aqua satellites which exceeded 5 tons. Along with the size and weight inflation, the development and launch cost also went up to nearly 10 billions yen for one unit of satellite (designated operation period is five to ten years). Consequently, the Earth observation satellites have been developed, lunched and operated by the national initiative, often influenced heavily by political decisions and budget limitation.

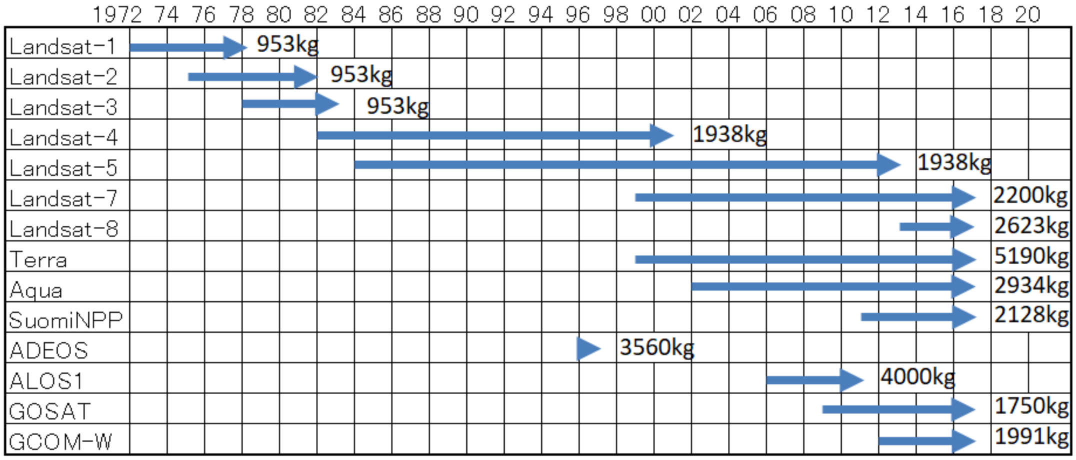

Figure 1.1: The weight and operate term of typical Earth observation satellite

Since late 1990's this trend in the satellite remote sensing has been changed gradually. The size of satellite trends to be smaller with the technology advancement mainly on the hardware. The weight of small satellite is around 100 kg ∼ 500 kg, and the development cost is reduced to around a few billions of yen. Remarkably, the satellites of private enterprise becomes extremely smaller in the last 5 years. Moreover, miniaturization of satellite size has progressed drastically. Those satellites, called nano/micro satellites, have been paid much attention from various industries. The weight of those satellite reaches to 100 kg and under. For instance, the weight of the satellite, ASNARO, which is lunched in 2014, is 450 kg and its size is 1 m × 1m ×

3 m. The weight of some satellites even reached to less than 1 kg. The development cost can be reduced to around a hundred million yen, approximately 1 % of the large sized satellite.

The down sizing trend of Earth observation satellite leads to further cost reduction mainly for launch and operation. As a result, the use of multiple satellites, known as satellite constellation, has been a realistic choice in the last ten years. To form a sensor system by the constellation, multiple satellites should be launched into difference orbits at the once. By a constellation system, both the spatial resolution and observation frequency can be enhanced simultaneously: These two are no longer in trade-off. One such example is a constellation system developed by a private sector, Planet Labs, in the united states. The company lunched more than 60 units of so-called ‘nano satellite’ in 2016 to facilitate global sensor network in the space. Later, a Japanese company AXELSPACE has also announced their plan with more than 50 nano satellites to be launched in 2020. Developing countries have also been planning for their own satellite constellation, including China [7–12], India [13–15], and Thailand [16].

Observation frequency will be increased with those satellite constellations. Table1.1 summarizes this trends. The observation frequency by the well-established Landsat series is once in a 16-day revisit cycle. In this case, if land surface could not be observed once because of cloudy weather, it may not be able to observe more than a month. On contrary, since the observation frequency has been improved by the satellite constellations, more frequent observation is possible. Even if one satellite misses the observation chance because of the cloud, we will have an observation chance in the next day by another satellite of the same constellation system. This evolutionary technique prompts advancement in software aspect. Especially, calibration technique and parameter retrieval algorithm should be changed into more suitable form in the context of constellation.[17].

1.3 Earth Observation by Satellite Remote Sensing

An Earth observation satellite often carries several sensors, and the wavelength ranges observed by those instruments varies from short to long wavelengths that depends specifically on the designated targets for each sensor. For example, the satellite, Greenhouse gases Observing Satellite (GOSAT), observe reflected radiation in the rage of the visible to thermal wavelength to measure the distribution of greenhouse gases. Global Change Observation Mission Satellite (GCOM-C) as one of the Japanese satellite was designed to observe atmosphere, ocean or land surface [18].

Table 1.1: Revisit Cycle of Earth Observation Satellite

satellite	period [minutes]	revisit cycle [days]
Landsat-1,-2,-3	101	18
Landsat-4,-5	98.9	16
Landsat-7,-8	99	16
Terra	98.8	16
Aqua	98.8	16
Suomi-NPP	101	16
ADEOS	100.8	41
ALOS1	98.7	46
GOSAT	98.18	3

In the united sates, NOAA, Terra, Aqua, and Landsat series are the most popular satellites among many. By conducting those satellite missions, the long term Earth observation data have been acquired continuously for nearly five decades. The contribution of those missions have been and will be indispensable to establish long term data record for the global climate change [19].

1.4 Biophysical Parameter Retrieval Algorithms

Amount of fixed carbon to the ground can be estimated through the estimation of vegetation amount. In the land discipline of satellite remote sensing, vegetation status has been monitored by spectral vegetation index (VI). The VI has been used since early era of Earth observation, and has been a standard data product in various satellite missions [20]. Most of the VIs were developed based on reflectance observation in the red and NIR wavelength bands. In fact, the most popular VI, normalized difference vegetation index (NDVI) [21] , uses the red and NIR bands. Since its introduction in 1970's, it has been repeatedly used to estimate vegetation distribution, structure, composition, diversity, and productivity [20, 22]. NDVI is defined as reflectance ratio by

$$NDVI = \frac{\rho_N - \rho_R}{\rho_N + \rho_R}, \tag{1.1}$$

where ρ represents reflectance variable, and the subscripts R and N indicate red and NIR band, respectively.

Although NDVI has been successfully used for vegetation monitoring for more than four decades, it is also known to be influenced by various external factors, such as viewing and illumination conditions, aerosol amount, soil brightness, spectral band-pass filters, and so on. Among those, the most significant disturbance is the soil brightness which is in a numerical model often assumed to be located underneath vegetation canopy. It is well known that NDVI varies significantly as the soil brightness changes. Since the introduction of NDVI, numerous VIs have been proposed to minimize the influences of soil brightness on the VI value. One such example is soil adjusted vegetation index (SAVI) proposed by Huete in 1988 and its variants [23–25]. Atmospherically resistant vegetation index [26] was also proposed to reduce atmospheric influence. In this way, vegetation indices have been improved by a lot of effort, however, it is usually for vegetation indices to being used by limiting the physical principle. Some researchers reported that VIs are more suitable for regional and local targets which are composed of limited variations of target classes than for global monitoring of land surface [19, 27].

In recent years, due mainly to significant reduction of computational cost, direct inversion of numerical radiative transfer models has been used to retrieve biophysical parameters from remotely sensed reflectance spectra. The direct inversion technique are more flexible than the VIs in terms of model parameters and has advantages in theoretical justification [28]. Photon transport process is a complex mechanism which requires numerical solution to the linear transport equation. The direct inversion algorithm considers a whole parameter sets in the model to determine the most suitable combination. The retrieved biophysical parameter is more accurate than an empirical technique. On contrary, a VI does not usually require a whole parameter set to determine its coefficients [29]. Hence it tends to be simple and easy to apply to actual data processing, while retrieval accuracy is sacrificed in some extent. In general, the simplicity and accuracy are trade-off: Retrieval of biophysical parameter (by VI and direct inversion) is also the case [30]. Fulfilling both simplicity and accuracy is still a challenging theme in this field of study.

1.5 Vegetation Isoline

‘Vegetation isoline’ describes a relationship between two reflectances of different wavelength observed under a constant vegetation. Figure1.2 represents the relationship of vegetation reflectance spectra between red band and NIR band. This line is composed of reflectance spectra obtained by fixing the vegetation amount at a certain value and varying the soil brightness. Thus, each isoline represents the reflectance spectra of the same vegetation amount. Because of this, the line is called vegetation isoline [31, 32]. Because one vegetation isoline represents a constant vegetation amount, the information about vegetation isoline can be used to retrieve biophysical

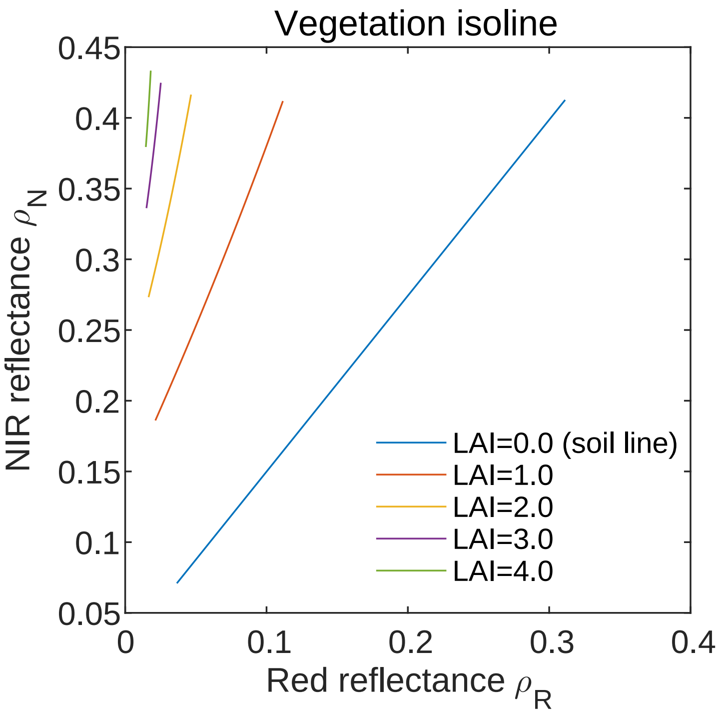

Figure 1.2: Plots of vegetation isoline for five LAI values.

parameters as an inversion technique based on a physical model. Figure1.3 shows NDVI plots as a function of LAI by assuming three different soil brightness. As can be seen in Fig.1.3, the NDVI values show variations along with the differences in soil brightness, which is a major reason of accuracy loss.

This 'soil influence' has been investigated by many researchers. One remarkable progress has been achieved by Huete et al. in late 1980's [31–33]. They conducted field experiments to physically alter the soil brightness in cotton field. They nicely explained how the vegetation isolines are formed by the variations of soil spectra. Since then, several improvement have been made to the NDVI formulation to take into account the soil influence [23–25, 34, 35]. In the recent years, Zhangyan et al. [36] clearly stated that in order to improve accuracy in VIs, one should make the VI's isolines similar to the vegetation biophysical isolines [36]. In 2000, Yoshioka et al. [37] introduced a formal derivation of the vegetation isoline equation in red-NIR reflectance subspace. Since then, both analytical and numerical studies on the vegetation isolines have been conducted by several researchers. This study is one such attempt to contribute its improvement.

Accuracy loss in VI is also brought by difference in spectral response function when two sensors are interchangeably used to form a single observation dataset. In

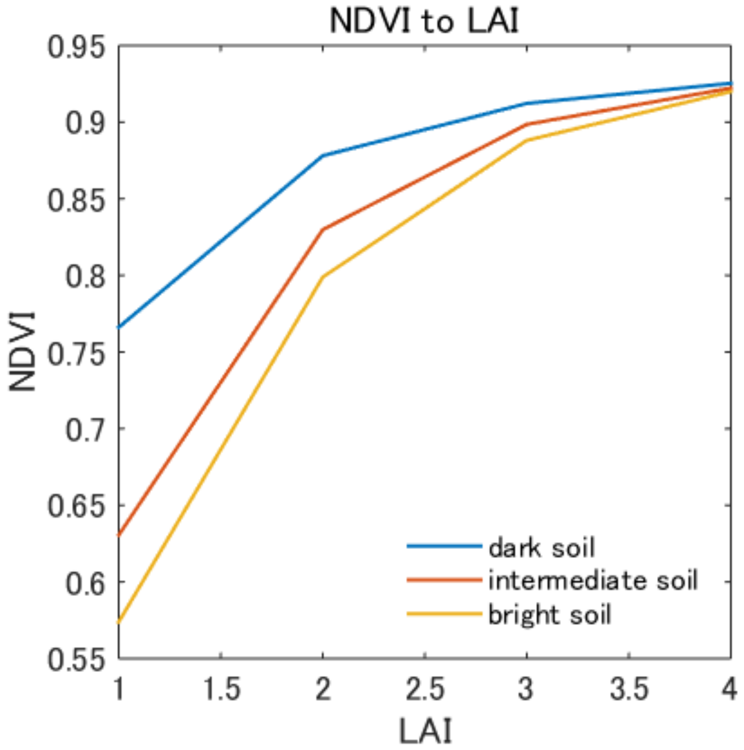

Figure 1.3: Plot of NDVI as a function of LAI for three different soil brightness (dark, intermediate, bright).

general, this case cannot be avoided because designated lifetime of Earth observation satellite is about five to seven years. If one wants to analyze satellite data for the term longer than a satellite lifetime, then one needs to combine data sets of at least two sensors. The accuracy loss caused by the difference in spectral responses of the two sensors is also unavoidable in such a case. This issue has been investigated by many researchers. As a result, translation methods from one sensor's output to another have been proposed [38–40]. In recent years, several researchers have investigated physically-based translation algorithm mainly based on reflectance relationship (isoline equation) to resolve some of the issues in this theme [41, 42]. In 2018, Fan et al. introduced the translation technique with vegetation isoline equations as one of the physically-based inter-calibration methods [43].

The concept of vegetation isoline has been used for estimation of biophysical parameters such as leaf area index, fraction of green cover, chlorophyll contents [30, 44]. These studies have been conducted based on the first-order approximated vegetation isoline equations. The resulted estimation is thus suffers from the error caused by the approximation. In order to reduce the error in the vegetation isoline, the form of the derived expression is expected to be rather complex. This complexity is resulted from the inclusions of higher-order interaction terms during the derivation. As it is described at the end of Section 1.3, the simplicity of the derived expression and its accuracy are in a trade-off relationship. This trade-off makes the investigation of vegetation isoline and its application difficult to proceed. This study is to overcome this difficulty: The ultimate goal of this study is to achieve accuracy improvement which is high enough to be used in a actual data processing while maintaining the simplicity of the derived expression.

1.6 Objectives

The objectives of this study are threefold. The first objective is to derive a new vegetation isoline equation with higher order interaction terms. The second one is to improve its accuracy by introducing a single adjustment factor into the derived formulation. The third is to extend the wavelength range into the entire visible to near infrared region. In the following Chapter, the derivation of the vegetation isoline will be explained in detail. Then, in Chapter III, the accuracy improvement of the derived expression will be explained. Specifically, an adjustment factor will be introduced. Its error reduction mechanism will also be analyzed based on a radiative transfer model. The derivation and accuracy improvement in Chapters II and III will be conducted by assuming a pair of red (655 nm) and NIR (865 nm) wavelength. In Chapter IV, this restriction will be extended to the wavelength range of 400 nm to 1200 nm. Finally, in Chapter V, this study will be concluded with some remarks on future efforts.

CHAPTER II

Vegetation Isoline Equations with First- and Second- Order Interaction Terms for Modeling a Canopy-Soil System of Layers in the Red-NIR Reflectance Space

2.1 Introduction

Biophysical parameter retrieval from remotely sensed reflectance spectra is a fundamental goal in the field of land remote sensing. Qin et al. [45] categorized the available retrieval algorithms into four groups based on the approaches taken: 1) techniques that relied on a spectral vegetation index and its correlation with biophysical parameters, such as the leaf area index (LAI) [23–25, 35, 46, 47]; 2) algorithms that used lookup tables [48, 49]; 3) neural networks [50–52]; and 4) direct inversions of numerical models (e.g., models of radiative transfer (RT)) using optimization methods [28, 45, 49, 53, 54] . These approaches present advantages and disadvantages over other approaches in terms of accuracy, computational costs, complexity, and applicability. The common feature of all categories of approach is that a better model increases the accuracy of the retrieved parameters. For this reason, significant efforts have been applied toward improving the accuracy of physical and numerical models.

The concept of vegetation isolines [23, 34, 55–58] forms the basis of the spectral vegetation index (VI) [23, 34, 47, 58], which has been widely used as a proximity measure (model) of surface biophysical parameters [59]. The isoline concept has been used as an analytical tool for investigating the influence of the soil on the retrieved parameters [36, 60–65]. From this standpoint, vegetation isoline equations provide a model for the relationship between reflectances at different wavelengths. Several reports have attempted to use isolines in the analysis of the VI [62, 65] and in parameter retrieval [30, 66]. Recently, these relationships were applied to intercalibration studies of the VI values obtained from different sensors [41, 42, 67]. Thus, the accuracy of the vegetation isoline equation must be improved in order to improve parameter retrieval algorithms and better understand the factors that affect intercalibration studies.

Yoshioka et al. [37] found that the derived isoline by the isoline equations loses accuracy in intermediate ranges of the LAI. Loss of accuracy in the isoline equation arises from truncations of the terms that correspond to multiple interactions among the photons reflected from the canopy layer (at the bottom surface) and the soil surface. These terms are referred to as higher-order interaction terms [37] in this study. The isoline equations derived by Yoshioka et al. [37, 62, 68] retain the interaction terms up to the first-order terms. The truncation, however, simplifies the derivation and yields a final form that is useful as an analytical tool [41, 42, 62, 65, 67]. One drawback of this truncation, however, is the loss of accuracy, which must be improved while simultaneously retaining the simplicity of the model. This study seeks to do just this.

We conducted a series of pilot studies [69–71] to explore possible improvements to the higher-order terms in the isoline equations. Derivations were developed for use in several cases. Three model issues have yet to be clarified. First, the relationship between the previously derived isoline, which includes a first-order interaction term, and the newly derived isoline, which includes higher-order interactions, is not yet understood. Second, the mechanism by which the errors were reduced upon inclusion of the higher-order term has not yet been identified. In some cases, isolines containing fewer interaction terms to describe one of the two bands showed significantly better accuracy. This mechanism must be explored systematically. This study examines these matters from an analytical and numerical perspective. The isoline equation derived here is even simpler than the equation introduced in the pilot studies; thus, this equation may be readily applied to new analyses. Finally, numerical procedures for determining the isoline parameters were not discussed in the pilot studies. These matters require further study for application purposes.

The objective of this study is to improve the first-order isoline equation by including second-order interaction terms while maintaining the model simplicity. This objective was achieved through a novel approach. Instead of retaining the second-order interaction terms of both the red and near-infrared (NIR) bands, we retained the term only for the reflectance of the NIR band. The asymmetric treatment of the second-order interaction significantly improved the model accuracy without sacrificing the simplicity of the derived expression. This study describes the formal steps used to derive the improved version of the vegetation isoline equation and validate its accuracy by conducting numerical experiments based on a coupled leaf and canopy radiative transfer model, PROSAIL [72].

The remainder of this discussion presents a review of a previously derived vegetation isoline equation [37, 62], referred to as a first-order isoline equation in this study. Two forms of higher-order approximations are derived. The results of numerical experiments using an RT model are then shown to evaluate the degree to which the accuracy was improved by the introduction of the higher-order approximations. The mechanism by which the accuracy was improved by the approximations is discussed in detail. Finally, the findings of this study are summarized.

2.2 Analytical Model and First-Order Vegetation Isoline

2.2.1 Analytical canopy reflectance model

This study begins with an analytical form of the top of the canopy (TOC) reflectance model, which has been used extensively in this field of study [73],

$$\rho_\lambda = \omega\rho_{v\lambda} + \omega\frac{T_\lambda^2 R_{s\lambda}}{1 - R_{s\lambda}R_{v\lambda}} + (1-\omega)R_{s\lambda}, \tag{2.1}$$

where the variables and notations mainly follow those given in [37, 62], except for the fraction of vegetation cover represented by ω in this study. The variable ρ_λ represents the TOC reflectance at the wavelength λ, $\rho_{v\lambda}$ represents the 'pure' canopy reflectance, which can only be obtained by assuming perfect absorbance beneath the canopy layer, $R_{s\lambda}$ and R_{v_λ} represent the bi-hemispherical reflectance of the soil and canopy layers, respectively. The variable $R_{v\lambda}$ is somewhat special among these variables because it represents the albedo of the bottom surface of the canopy layer. The details of the model are illustrated in Fig. 2 of the reference [37]. T_λ^2 represents the two-way transmittance of the canopy layer at the indicated wavelength, λ. We next defined the area-averaged two-way transmittance at a point,

$$\overline{T_\lambda^2} = \omega T_\lambda^2 + 1 - \omega. \tag{2.2}$$

The word 'area-averaged' indicates that the bare soil region, $(1-\omega)$, provides 'perfect' two-way transmittance properties, and the averaged transmittance of the partially vegetated area may be modeled using a weighted average of T_v^2 and 1.0, with weighted values of ω and $(1-\omega)$. In the following section, we briefly explain the vegetation isoline equation introduced previously [37, 62].

2.2.2 Vegetation isoline equation with a first-order interaction term in the red-NIR reflectance subspace

The isoline equation introduced in this subsection is referred to as the first-order isoline because only a single interaction term with the soil surface is included.

The model was derived by explicitly including the first-order interaction term as the second term of the right-hand-side (RHS) of Eq. (2.3),

$$\rho_\lambda = \omega\rho_{v\lambda} + \omega T_\lambda^2 R_{s\lambda} + \frac{\omega T_\lambda^2 R_{s\lambda}^2 R_{v\lambda}}{1 - R_{s\lambda}R_{v\lambda}} + (1-\omega)R_{s\lambda}, \tag{2.3}$$

where the second term of the RHS in Eq. (2.3) indicates the first-order interaction term. The second and higher interaction terms, represented by the third term of the RHS, is further defined as a truncated-order term,

$$O(R_{s\lambda}^2) = \frac{T_\lambda^2 R_{s\lambda}^2 R_{v\lambda}}{1 - R_{s\lambda}R_{v\lambda}}. \tag{2.4}$$

Equation (2.3) can be simplified using Eq. (2.2),

$$\rho_\lambda = \omega\rho_{v\lambda} + \overline{T_\lambda^2} R_{s\lambda} + \omega O(R_{s\lambda}^2). \tag{2.5}$$

Two equations were used to describe the red (denoted by the subscript R) and near-infrared wavelengths (N),

$$\rho_R = \omega\rho_{vR} + \overline{T_R^2} R_{sR} + \omega O(R_{sR}^2), \tag{2.6}$$

$$\rho_N = \omega\rho_{vN} + \overline{T_N^2} R_{sN} + \omega O(R_{sN}^2). \tag{2.7}$$

The soil line assumption of [74] was applied,

$$R_{sN} = aR_{sR} + b, \tag{2.8}$$

where a and b represent the slope and offset of the soil line, respectively. Equations (2.6), (2.7), and (2.8) were used to eliminate the soil reflectances R_{sR} and R_{sN} to obtain the first-order approximated vegetation isoline equation,

$$\rho_N = a\gamma_1\rho_R + D_1 + \epsilon_1, \tag{2.9}$$

where γ, D, and ϵ_1 are defined by

$$\gamma_1 = \overline{T_N^2}/\overline{T_R^2}, \tag{2.10}$$

$$D_1 = b\overline{T_N^2} + \omega\left(\rho_{vN} - a\gamma_1\rho_{vR}\right), \tag{2.11}$$

$$\epsilon_1 = \omega\left[O(R_{sN}^2) - a\gamma_1 O(R_{sR}^2)\right]. \tag{2.12}$$

Finally, we obtained an approximated form of the vegetation isoline equation by truncating the higher-order interaction term,

$$\rho_N \approx a\gamma_1\rho_R + D_1. \tag{2.13}$$

The first-order isoline model suffers from truncation errors. For example, Yoshioka et al. [37] indicated that the truncation error increases at higher soil reflectance values, and the relative error can reach 5%. Their findings suggest that the errors in the retrieved biophysical parameters calculated based on the isoline formula, can reach the same magnitude. The truncation errors in the isoline formula should, therefore, be minimized to obtain more accurate parameter retrievals using the isolines.

The truncation error pattern obtained from the first-order isoline model was numerically characterized using a radiative transfer model PROSAIL [72]. Figure 2.1 shows the first-order isoline and reflectance spectra simulated using the model in the red and NIR reflectance subspaces. The empty circles denote the simulated reflectance, which was considered to be a 'true' spectrum. The solid lines indicate the first-order isoline at various LAI values of the pure canopy component ranging from 0 to 4 at intervals of 0.5. The left and right figures present the results obtained from different fraction of vegetation cover (FVC, ω) values: full coverage ($\omega = 1$) or half coverage ($\omega = 0.5$), respectively. A detailed description of the simulation conditions is provided in the latter section. These results confirmed that the error (the discrepancy between the empty circles and the solid lines) in the first-order isoline could be reproduced numerically using the model presented in this study.

The error trend was characterized by plotting the distance between the isolines and the true spectra, as shown in Fig. 2.2 at LAI=1.0 (solid line) and LAI=4.0 (dashed line) for both the fully covered and partially covered cases. The error was plotted as a function of the soil reflectance in the red band. The figure clearly reveals two characteristics: First, the error increased as the soil became brighter. Second, the error at LAI=1.0 always exceeded that obtained for LAI=4.0. Because these trends have been analyzed previously [37, 62], we summarize the conclusions briefly: (1) the influence of the higher-order interaction terms increased for brighter soils; and (2)

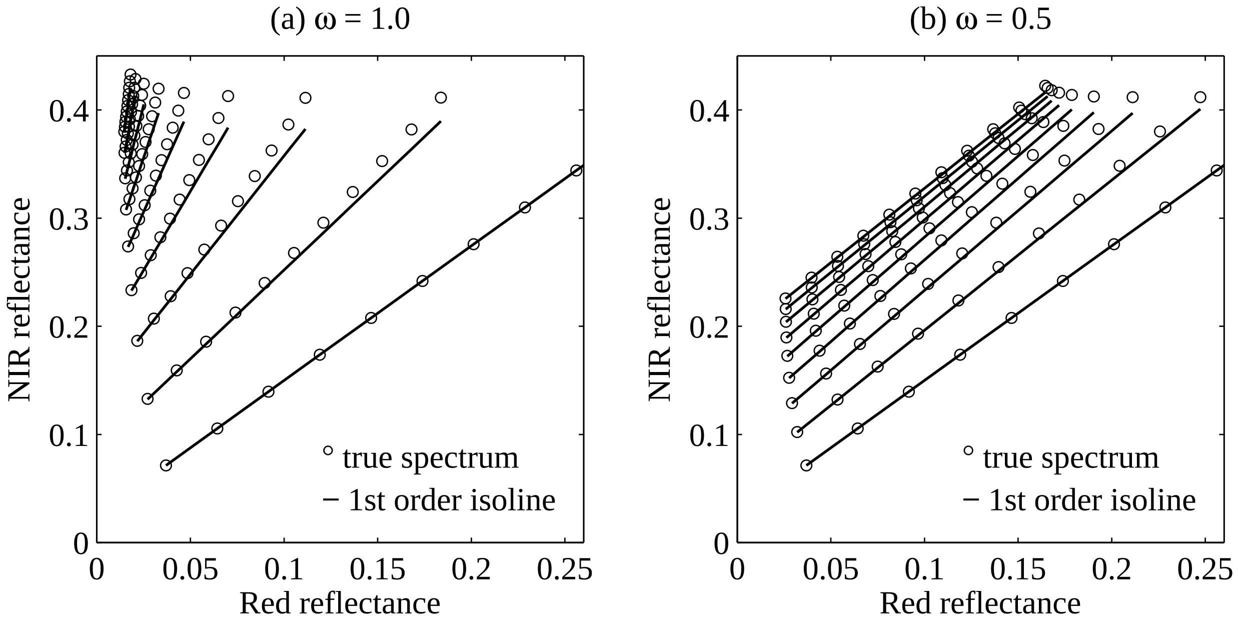

Figure 2.1: First-order vegetation isolines and simulated reflectance spectra obtained using PROSAIL. The value of the FVC represented by ω was assumed to be (a) unity, representing a fully covered case; or (b) 0.5, representing a partially covered case.

this influence first increased and then decreased as the canopy thickened.

The error could be reduced to some extent by adjusting the higher-order terms. The next section discusses the derivation steps used to obtain the second-order approximated reflectance and a new isoline equation referred to as the 'asymmetric order isoline' in this study.

2.3 Second-Order Approximation and Asymmetric Order Isoline

2.3.1 Parametric form of the second-order approximated reflectance spectra

The second-order interaction term could be explicitly separated from the higher-order term in Eq. (2.3) using the approach taken to separate the first-order term. Specifically, the interaction terms were retained up to the second order for both the

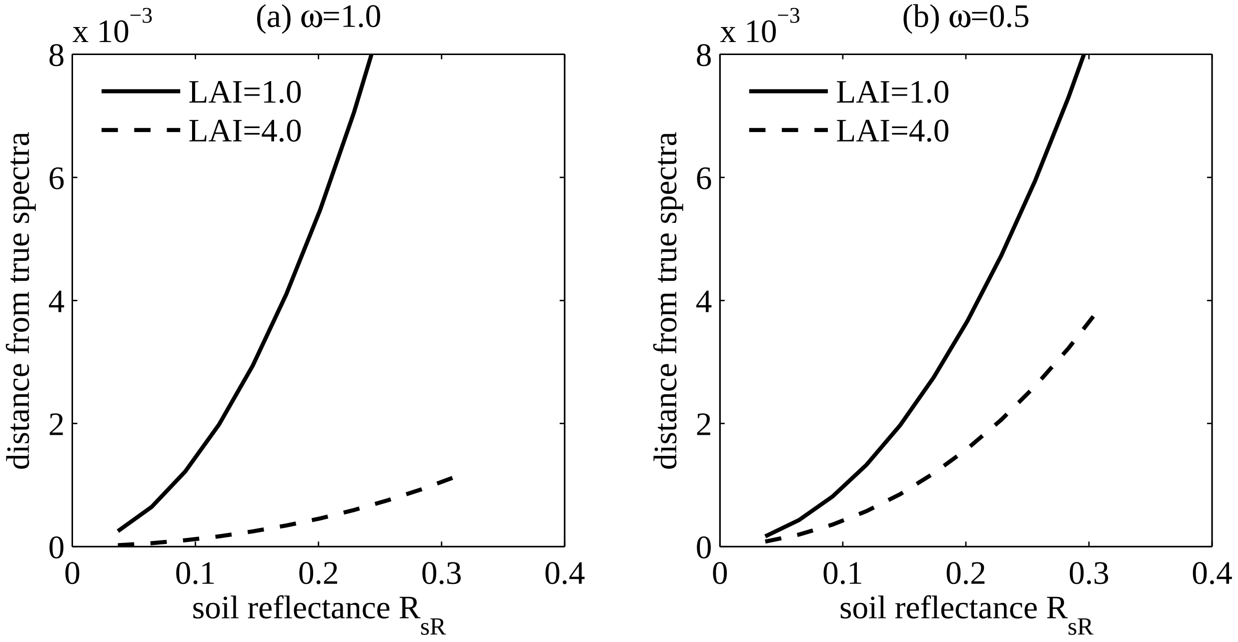

Figure 2.2: Distance between the first-order isoline and the true reflectance spectrum shown in Fig. 2.1 for (a) $\omega = 1.0$ and (b) $\omega = 0.5$.

red and NIR spectra in Eq. (2.3). The resulting equation then becomes

$$\rho_\lambda = \omega \rho_{v\lambda} + \overline{T_\lambda^2} R_{s\lambda} + \omega T_\lambda^2 R_{v\lambda} R_{s\lambda}^2 + \omega O(R_{s\lambda}^3), \tag{2.14}$$

where

$$O(R_{s\lambda}^3) = \frac{T_\lambda^2 R_{s\lambda}^3 R_{v\lambda}^2}{1 - R_{s\lambda} R_{v\lambda}}. \tag{2.15}$$

We next rewrote Eq. (2.14) to describe the red and NIR bands using the subscripts R and N to obtain

$$\rho_R = \omega \rho_{vR} + \overline{T_R^2} R_{sR} + \omega T_R^2 R_{vR} R_{sR}^2 + \omega O(R_{sR}^3), \tag{2.16}$$

$$\rho_N = \omega \rho_{vN} + \overline{T_N^2} R_{sN} + \omega T_N^2 R_{vN} R_{sN}^2 + \omega O(R_{sN}^3). \tag{2.17}$$

The soil line in Eq. (2.8) was used to obtain the reflectance spectrum to a second-order approximation, as represented by the following form with R_{sR} as a parasite parameter,

$$\begin{bmatrix}\rho_R\\ \rho_N\end{bmatrix} = \begin{bmatrix}\overline{T_R^2} & \omega T_R^2 R_{vR}\\ a\overline{T_N^2} + \omega 2ab T_N^2 R_{vN} & \omega a^2 T_N^2 R_{vN}\end{bmatrix}\begin{bmatrix}R_{sR}\\ R_{sR}^2\end{bmatrix} + \omega\begin{bmatrix}\rho_{vR}\\ \rho_{vN} + b\overline{T_N^2}/\omega + b^2 T_N^2 R_{vN}\end{bmatrix} + \omega\begin{bmatrix}O(R_{sR}^3)\\ O(R_{sN}^3)\end{bmatrix}. \tag{2.18}$$

The last term could be neglected to obtain a parametric representation of the approximated second-order spectrum. This form was used only in the numerical experiments to evaluate the isoline equation, as discussed in the following subsection.

2.3.2 Isoline equation obtained by asymmetrically truncating the higher-order interactions

The previous subsection discussed the retention of the higher-order interaction terms up to the second-order terms for both the red and NIR bands. In this subsection, we include the second-order interaction term only in the description of the NIR band, and the red band is approximated up to the first-order interaction term.

A system of equations was obtained using Eqs. (2.6), (2.17), and (2.8), in which the soil reflectances were eliminated. Algebraic manipulations yielded the final results,

$$\rho_N = a^2\zeta\rho_R^2 + a(\gamma_1 + \delta_1)\rho_R + D_1 + \delta_0 + \epsilon_2, \tag{2.19}$$

where

$$\zeta = \omega T_N^2 R_{vN}/(\overline{T_R^2})^2, \tag{2.20}$$

$$\delta_0 = \zeta\left(b\overline{T_R^2} - \omega a\rho_{vR}\right)^2, \tag{2.21}$$

$$\delta_1 = 2\zeta\left(b\overline{T_R^2} - \omega a\rho_{vR}\right), \tag{2.22}$$

$$\begin{aligned}\epsilon_2 &= \omega O(R_{sN}^3) + a^2\omega^2\zeta\left[O(R_{sR}^2)\right]^2\\ &\qquad - a\omega\left[2a\zeta\rho_R + \gamma_1 + 2\zeta\left(b\overline{T_R^2} - a\omega\rho_{vR}\right)\right]O(R_{sR}^2).\end{aligned} \tag{2.23}$$

Neglecting ϵ_2 from Eq. (2.19), we have

$$\rho_N \approx a^2\zeta\rho_R^2 + a\gamma_2\rho_R + D_2, \tag{2.24}$$

where

$$\gamma_2 = \gamma_1 + \delta_1, \tag{2.25}$$

$$D_2 = D_1 + \delta_0. \tag{2.26}$$

2.4 Results of the Numerical Simulations

2.4.1 Parameter settings used in the numerical experiments

A series of numerical experiments was conducted using the canopy radiative transfer model PROSAIL [72]. This model consists of the leaf model PROSPECT [75] and the canopy model SAIL [76]; thus, two types of input parameter were required. Numerical experiments were conducted using the set of input values provided with the code, except that the three input parameters LAI, leaf angle distribution (LAD), and soil factor, were set as follows. The soil factor was obtained from the mixture ratio of the wet and dry soil spectra provided with the code. The parameter ranges of the three parameters were as follows. LAI was varied from 0.0 to 4.0 at 0.5 intervals (9 levels), and the soil factor was varied from 0.0 to 1.0 at 0.1 intervals (11 levels). During the numerical experiments, six LAD models (planophile, erectophile, plagiophile, extremophile, spherical, and uniform distributions) were assumed. (The results section focuses on the case of a spherical LAD, as a representative case, for brevity.) Finally, the obtained reflectance spectra were linearly mixed with the pure soil reflectance spectra using the fraction of green cover (ω) as a weight. The parameter ω was varied from 0.0 to 1.0 in 0.1 intervals (11 levels). The total number of spectra used to model each LAD was 1089. In the analysis, we assumed that the reflectances at 655 nm and 865 nm provided representative values of the red and NIR bands in this study. This choice of wavelength pair corresponded to the center of the red and NIR bands obtained from the Landsat 8 operational land imager (OLI) sensor.

The other input parameters provided with the code were fixed as follows. For the SAIL part of the code, the parameter describing the hot spot (hspot) was set to 0.01. The solar zenith, observation zenith, and relative azimuth angle were set to 30, 10, and 0 degrees, respectively. For the PROSPECT part of the code, chlorophyll-a and -b, carotenoid, and the leaf mass per area were assumed to be 40, 8, and 0.009 in g/cm^2, respectively. The equivalent water thickness was set to 0.01 cm, and the brown pigment content was assumed to be zero. Finally, the leaf mesophyll structure (N) was assumed to be 1.5 (the equivalent number of layers).

2.4.2 Numerical procedure used for the isoline parameter retrieval and the error estimation

The isoline parameters used in Eqs. (2.9) and (2.19) were computed from $T_{v\lambda}^2$ and $\rho_{v\lambda}$, which were determined using the algorithm described in the reference [37]. This algorithm required two hypothetical simulations in which the soil was assumed to be 'spectrally flat', with a zero reflectance value, or the soil was assumed to have a medium reflectance value over the entire wavelength range. In addition to $T_{v\lambda}^2$ and $\rho_{v\lambda}$, the asymmetric order approximated isoline, Eq. (2.19), required a value of R_{vN} to define ζ. R_{vN} was determined by conducting an additional simulation in which the soil was assumed to be spectrally flat and even brighter than was assumed in the simulation used to determine $T_{v\lambda}^2$. The assumption of brighter soil increased the photon contributions of the higher-order interactions. The parameter R_{vN} was determined by solving Eq. (2.17) for R_{vN} and using T_{vN}^2 and ρ_{vN}, which were computed prior to R_{vN}. With these variables in hand, the isoline parameters γ_1, D_1, γ_2, D_2, ζ, δ_0, and δ_1 were obtained. In summary, three hypothetical simulations were conducted to determine the isoline parameters that corresponded to spectrally flat soil at three different brightness levels.

The errors in the isolines and the approximated reflectance spectra were estimated by computing the distance from the true spectra. Note that the error in the isolines should be equal to the distance between the true reflectance spectrum (which includes all higher-order interaction terms) and the 'isoline' represented by Eqs. (2.9) and (2.19), corresponding to the first-order and asymmetric order isolines, respectively. Even if a spectrum approximated using a model based on truncated higher-order terms were far from the true spectrum, the error could be zero provided that the 'isoline' passed through the point of the true spectrum in the red–NIR reflectance subspace. This distance was employed as a measure of the error because the error in the biophysical parameter retrieval obtained using the isoline reached zero numerically under conditions in which the true spectrum point coincided with the isoline. The goal of isoline determination is to identify the conditions under which the isoline coincides with the true spectra.

2.4.3 Comparison of the accuracy across the three approximations

The performances of the two types of isoline, namely, the first-order and second-order isolines, were compared with the true and second-order reflectance spectra obtained in the red-NIR reflectance subspace. Figure 2.3 represents the isolines as solid lines. The first- (Eq. (2.9)) and the asymmetric-order (Eq. (2.19)) isolines are plotted as black and red lines, respectively. The empty circle represents the true spectra obtained directly from PROSAIL and corresponds to the spectra represented by Eq. (2.1). The cross-mark was used to indicate the second-order approximated reflectance spectra, Eq. (2.18). The isolines were compared at two values of the vegetation cover: (a) $\omega = 1.0$ and (b) $\omega = 0.5$.

These figures reveal that the asymmetric isolines (red lines) provided much better approximates for the true spectra (empty circles) than the first-order isolines (black lines) over the entire LAI range. The error in the asymmetric order isoline was smaller than that obtained from the first-order isoline. Furthre analyses in this subsection (Table 1) and the next subsection (Fig. 6) indicated that the asymmetric isolines were even closer to the true spectra than the second-order approximated reflectance spectra (cross marks) over the full spectral range. This result is, to some extent, surprising because the error in the second-order approximated spectrum was expected to be smaller than the error obtained from the asymmetric isoline, in which one of the bands (the red band in this study) was approximated to the first order instead of to the second order. This result will be further discussed later in this section.

The errors obtained from the two isolines and the second-order reflectance spectra were directly compared, and the distance between these isolines and the spectra obtained from the true values (including all higher-order terms) are plotted as a function of the soil reflectance R_{sR} for the four combinations of LAI and ω (Fig. 2.4). The errors obtained from the first-order isoline, second-order reflectance, and asymmetric order isoline are denoted using different colors. Figures 2.4(a) and 2.4(b) show the results obtained for the fully covered case, with LAI=1.0 and 4.0, respectively. Figures 2.4(c) and 2.4(d) show the results obtained for the half-covered case. These figures indicated that (1) the error over R_{sR} was high at high values of R_{sR}, and (2) in most cases, the errors of the asymmetric isoline were the smallest among the three models over the range of R_{sR}. This result indicates that the accuracy of the asymmetric isoline dramatically improved over the entire range of R_{sR}. Again, recall that the asymmetric isoline used a first-order approximated reflectance to model the red band, whereas a second-order reflectance was used to model the second-order interaction terms in both the red and NIR bands. The error in the second-order reflectance (blue line) was expected to be smaller than the error obtained from the asymmetric isoline (red line). These results could be explained in terms of the relationship between the overcorrection and the truncation error. This mechanism is described in detail below.

Before discussing these surprising results, we will analyze the error trend by investigating the error distributions obtained from the simulations conducted using

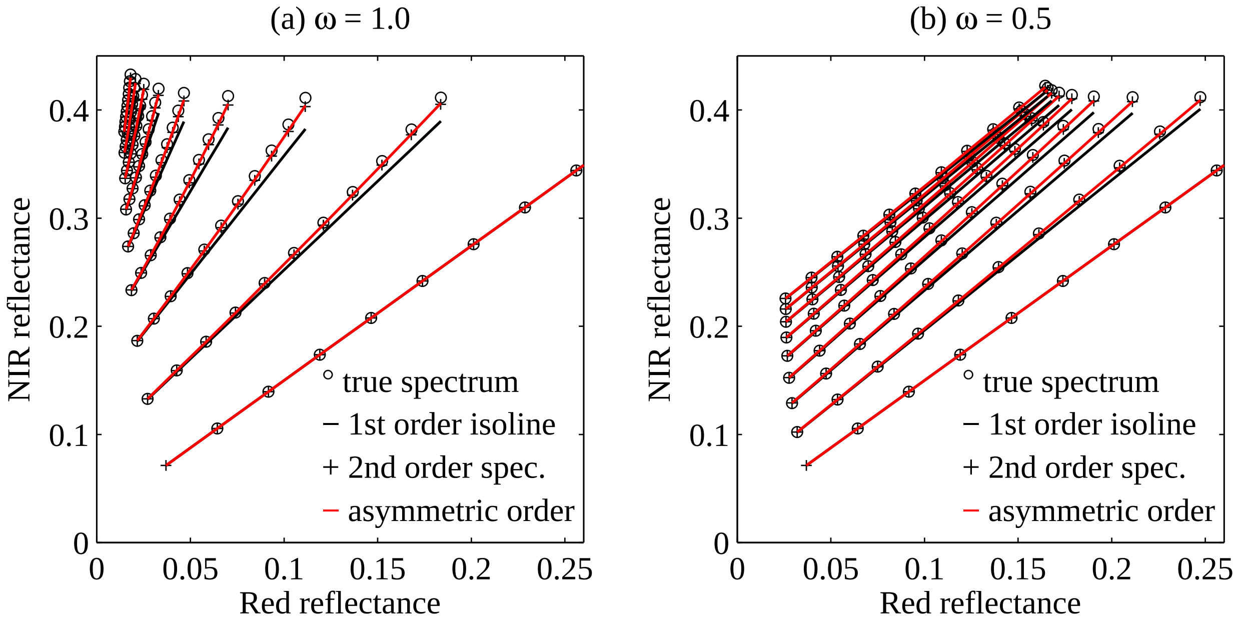

Figure 2.3: First-order isoline (black line) defined by Eq. (2.9), and the asymmetric isoline (red line) defined by Eq. (2.19), with the second-order reflectance spectra (cross mark) computed using Eq. (2.18) and the true spectra (empty circle) computed using PROSAIL. The value of the FVC represented by ω was assumed to be (a) unity, representing a fully covered case; or (b) 0.5, representing a partially covered case.

combinations of the three input parameters (LAI, fraction of vegetation cover ω, and soil reflectance R_{sR}) employed in this study. Figure 2.5 shows a histogram of the errors obtained from the three approximations. The figure reveals that the asymmetric order isoline errors were clustered at lower errors, unlike the errors of the other two approximations, and very few simulations provided errors of 1.0×10^{-3}. On the other hand, the errors of the first- and second-order isoline reflectance simulations were uniformly distributed at distances exceeding 1.0×10^{-3}. These results confirmed that the asymmetric order isoline outperformed the other two approximations.

The model performances were further validated by varying the leaf angle distribution (LAD). The experiments compared the results obtained by assuming six different LAD models: planophile, erectophile, plagiophile, extremophile, spherical, and uniform distributions. The error values were averaged over the entire range of the three parameters (LAI, ω, and R_{sR}). These results are summarized in Table 2.1, which lists the standard deviation and the maximum values obtained in all cases. The table indicates that the average error of the asymmetric order isoline was much smaller (by nearly one order of magnitude) than the average error of the first-order isoline for all LAD cases. The table also reveals that the performance of the asymmetric order isoline was better than that of the second-order reflectance in terms of the average, standard deviation, and the maximum value. Table 2.1 supports the above findings (e.g., that the asymmetric order isoline performed better than the other models), derived in Figs. 2.4 and 2.5. The next subsection analyzes the detailed mechanisms underlying this trend.

2.4.4 Error reduction mechanisms using the second-order isoline

The numerical results presented above indicate that the asymmetric order isoline model was more accurate than the reflectance approximated up to the second-order interaction terms, despite the fact that the latter included a greater number of terms in the red band than did the asymmetric order isoline. This trend is not easy to understand intuitively, but it appeared to result from the tendency of the model to overcorrect by a degree that was approximately equal to the order of magnitude of the truncation error in the isoline.

We further examined the model performances by plotting the four reflectance spectra: (1) the true spectrum computed directly using PROSAIL; (2) the first-order approximated reflectance; (3) the second-order approximated reflectance; and (4) the asymmetric order approximated reflectance using two types of vegetation isoline (first-order isoline and asymmetric order isoline). Figure 2.6 shows a limited region of the red-NIR reflectance subspace to illustrate the differences between the four predicted spectra. This part of the subspace corresponds to the results obtained at LAI=2.0 for the case of full canopy coverage.

Figure 2.6 reveals that the closest spectrum to the true spectrum (denoted by the circle) is the second-order approximated reflectance, denoted by the crosses. The asymmetric isoline represented by the red line is even closer to the true spectrum, whereas the asymmetric order approximated reflectance spectrum (triangle) is further from the true spectrum compared to the second-order approximated spectrum. Recall that the errors are measured as the distance between the true spectrum (circle) and the model spectra. Because the distance to the isoline (red line) was smaller than the distance between the true spectrum and the second-order approximated spectrum (cross), the error of the asymmetric isoline was surely smaller. Therefore, these results are consistent with the trend described in the previous subsection.

This trend could be understood as resulting from an overcorrection to the NIR band in the asymmetric approximation and the truncation error in the isoline. In the asymmetric case, the inclusion of a second-order term only in the NIR band over-corrected the spectrum upward in the direction from the first-order spectrum (square), as illustrated in Fig. 2.7. The overcorrection of the NIR band shifted the asymmetric order approximated spectrum (triangle) from the position of the first-order approximated spectrum (square) parallel to the NIR axis instead of toward the true reflectance spectrum (circle). Fortunately, this shift direction and distance compensated for the truncation error. As a result, the isoline of the asymmetric approximation (red line) ran through the subspace between the true (circle) and second-order approximated spectra (cross). In summary, the overcorrection of the NIR band and the truncation error in the NIR band nicely canceled each other out, thereby shifting the isoline (red) upward into the subspace to decrease the distance between the true spectrum and the isoline.

2.5 Discussion and Conclusions

The truncation of higher-order interaction terms presents a major limitation to isoline models based on a first-order approximation, although this truncation can simplify the final expression. The simplicity of the analytical form is advantageous for analytical and numerical investigations of parameter retrieval algorithms, such as the LAI, FVC, as well as of proximity measures, such as the spectral vegetation index. The accuracy of the vegetation isoline models may be increased by including the second-order interaction terms in both the red and NIR reflectances; however, the derived expression was rather complex, thereby reducing the utility of the model as a tool for analytical and numerical studies. This study took a unique approach: instead of including the second-order terms in both the red and NIR bands, this study included the term only in the NIR reflectance.

The final form of the derived asymmetric isoline is rather simple; thus, it can be easily altered, similar to the previously derived first-order isoline. This model, however, dramatically reduces the errors obtained in the first-order isoline, and the accuracy of the asymmetric case is even better than that obtained from the reflectance spectrum using the second-order term. With both simplicity and accuracy, the derived expression can contribute to a wide range of applications, from designing optimal spectral vegetation index sets to developing inversion algorithms in which the derived expression may be used as a constraint in the optimization algorithm.

This study focused on only the relationship between the red and NIR reflectances. Although overcorrections in the NIR band nicely compensated for the truncation errors inherent in the isoline equation, this compensation mechanism may not apply to other combinations of wavelengths. The applicability of this model to other combinations, e.g., the NIR and shortwave bands, will require more thorough investigations. The findings of this study are currently limited to the combination of red and NIR wavelengths.

Overcorrection by intentionally truncating more terms in the red band than in the NIR band compensated for the truncation errors of the higher-order term in a derivation of the vegetation isoline. These findings suggest that optimal control over the overcorrection level could further reduce the errors in the asymmetric isoline. This possibility is worth exploring in future studies.

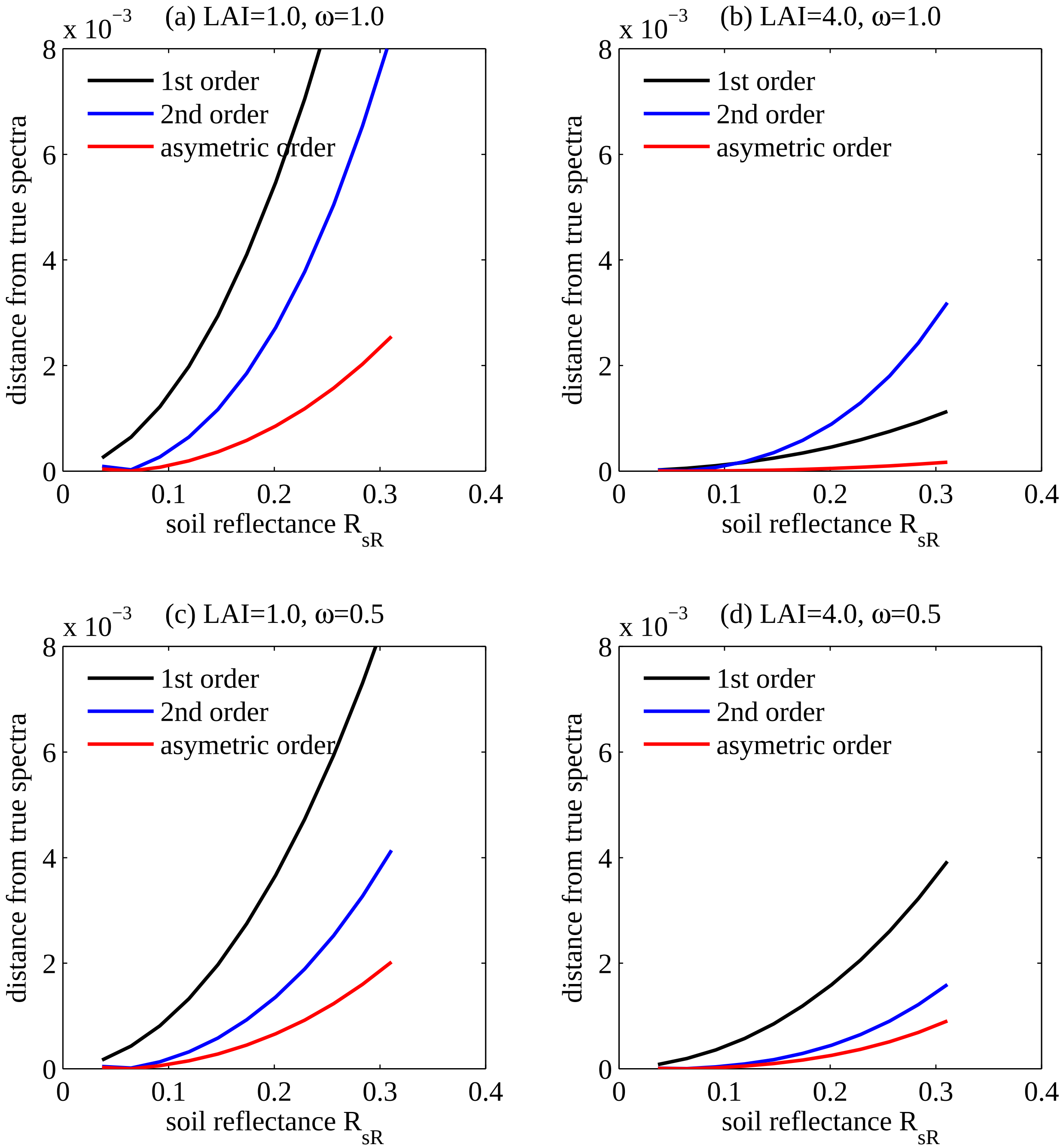

Figure 2.4: Distance between the first-order isoline, second-order reflectance spectrum, or the asymmetric isoline and the corresponding true reflectance spectra, as a measure of the error shown in Fig. 2.3 at four combinations of LAI and ω: (a) LAI=1.0, $\omega = 1.0$, (b) LAI=4.0, $\omega = 1.0$, (c) LAI=1.0, $\omega = 0.5$, and (d) LAI=4.0, $\omega = 0.5$.

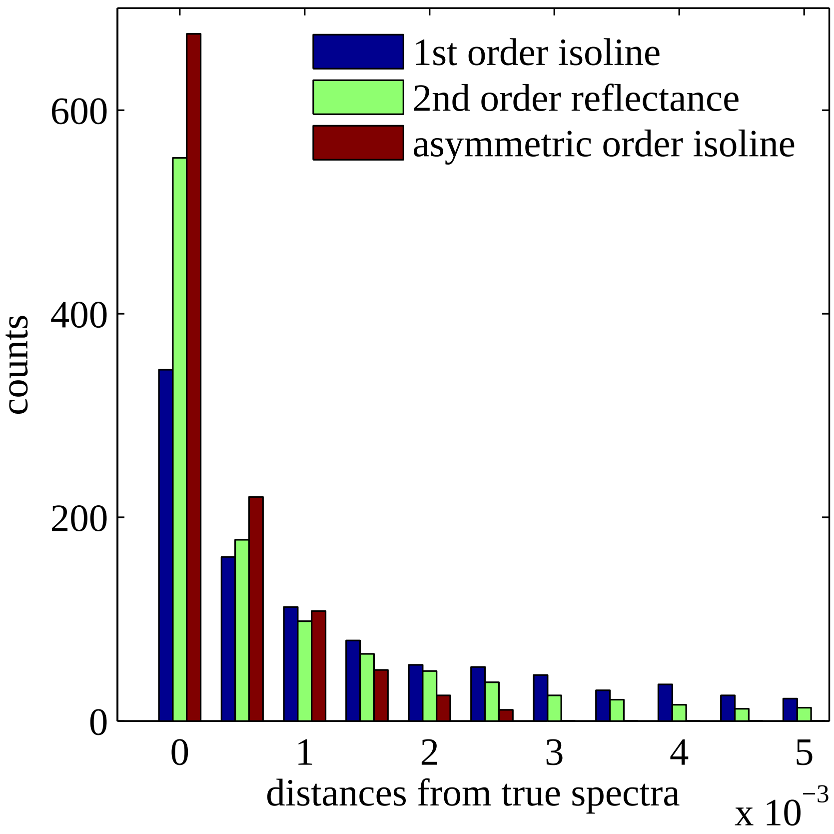

Figure 2.5: Histogram of the errors obtained from the first-order isoline, second order reflectance, and asymmetric order isoline. The total number of simulated cases was 1089 = (9 discrete values of LAI) × (11 values of FVC, ω) × (11 values of soil reflectance R_{sR}), assuming a spherical leaf angle distribution.

Table 2.1: Average, standard deviation, and maximum differences between the true reflectance spectra and the three cases of the isoline/reflectance spectra. The differences were computed by assuming six types of leaf angle distribution (LAD): planophile, erectophile, plagiophile, extremophile, spherical, and uniform distributions.

	LAD: Planophile		
	1st order isoline	2nd order spectrum	asymmetric isoline
Mean	1.93×10^{-3}	8.53×10^{-4}	3.46×10^{-4}
STD	2.47×10^{-3}	1.33×10^{-3}	5.06×10^{-4}
MAX	1.30×10^{-2}	8.08×10^{-3}	2.56×10^{-3}
	LAD: Erectophile		
	1st order isoline	2nd order spectrum	asymmetric isoline
Mean	2.93×10^{-3}	1.92×10^{-3}	8.44×10^{-4}
STD	3.68×10^{-3}	2.84×10^{-3}	1.16×10^{-3}
MAX	1.85×10^{-2}	1.60×10^{-2}	5.79×10^{-3}
	LAD: Plagiophile		
	1st order isoline	2nd order spectrum	asymmetric isoline
Mean	1.57×10^{-3}	5.53×10^{-4}	2.16×10^{-4}
STD	2.06×10^{-3}	8.89×10^{-4}	3.23×10^{-4}
MAX	1.10×10^{-2}	5.60×10^{-3}	1.62×10^{-3}
	LAD: Extremophile		
	1st order isoline	2nd order spectrum	asymmetric isoline
Mean	1.74×10^{-3}	6.33×10^{-4}	2.47×10^{-4}
STD	2.26×10^{-3}	1.01×10^{-3}	3.68×10^{-4}
MAX	1.18×10^{-2}	6.22×10^{-3}	1.84×10^{-3}
	LAD: Spherical		
	1st order isoline	2nd order spectrum	asymmetric isoline
Mean	1.95×10^{-3}	8.79×10^{-4}	3.57×10^{-4}
STD	2.51×10^{-3}	1.37×10^{-3}	5.21×10^{-4}
MAX	1.32×10^{-2}	8.31×10^{-3}	2.65×10^{-3}
	LAD: Uniform		
	1st order isoline	2nd order spectrum	asymmetric isoline
Mean	1.65×10^{-3}	5.85×10^{-4}	2.28×10^{-4}
STD	2.15×10^{-3}	9.38×10^{-4}	3.41×10^{-4}
MAX	1.13×10^{-2}	5.86×10^{-3}	1.71×10^{-3}

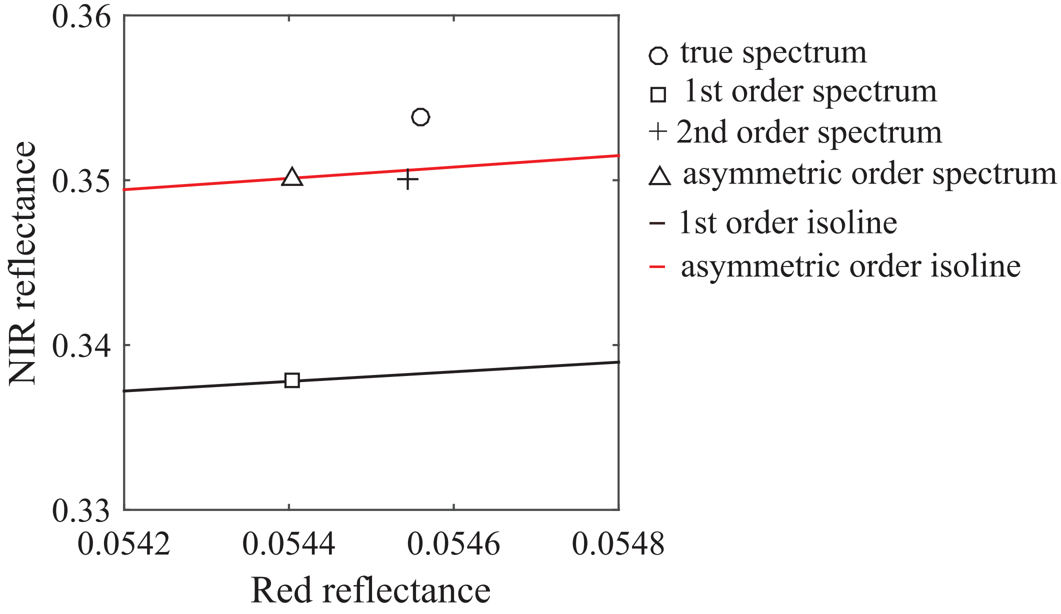

Figure 2.6: Comparison of the four approximated reflectance spectra: true spectrum calculated using PROSAIL (circle), first-order approximated spectrum (square), second-order approximated spectrum (cross), and asymmetric order approximated spectrum (triangle), with the two isolines (first-order, black line, and asymmetric order, red line.) The value of LAI=2.0 and full canopy coverage ($\omega = 1.0$) were assumed.

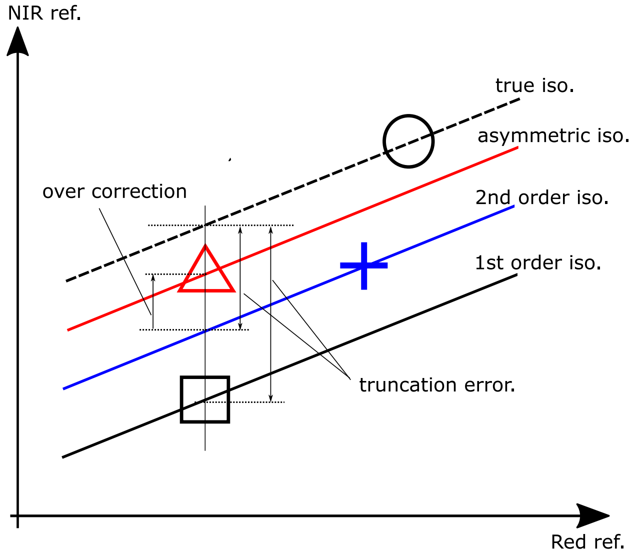

Figure 2.7: Illustration of the error reduction mechanism in the asymmetric order approximated isoline.

CHAPTER III

Improved Accuracy in the Asymmetric Second-Order Vegetation Isoline Equation over the Red–NIR Reflectance Space

3.1 Introduction

Estimation of biophysical parameters from remotely sensed reflectance requires calibration [77], inter-comparison of reflectance spectra [78] and derived data products [79]. Parameter retrieval based on those calibration efforts has been a major goal of land analysis disciplines [19]. The outcomes of such efforts provide crucial information about local and global areal coverage, that is used in a wide range of applications [80]. Although numerous investigations have reported the development and improvement of biophysical parameter retrieval algorithms, many of these algorithms involve simple algebraic band manipulations known as spectral vegetation indices (VIs) [45, 81]. A variety of VI models have been investigated for their robustness against both internal and external influences [23, 24, 26, 35, 47, 82–84].

A key component of VI model development is the relationship between two reflectances of different bands obtained under fixed biophysical parameter conditions. This relationship produces a reflectance spectrum trajectory in a reflectance subspace attributed to a fixed biophysical parameter value; therefore, this relationship is known as a vegetation isoline. The concept of a vegetation isoline has been used repeatedly to develop optimal VI models [23, 24, 34, 35] and to investigate their robustness against external factors [62, 65]. The isoline concept has been directly used to retrieve leaf area index and the fraction of vegetation cover [30, 66]. In recent years, the concept has been applied to the inter-sensor calibration of VIs [41, 42].

From the application point of view, understanding of band-to-band relationship would provide information about land cover dependency of calibration coefficients. In retrievals of biophysical parameter, an isoline equation with higher accuracy would lead to better results in retrieved parameters. Moreover, biophysical parameters vary along with the evolution of phenology, which eventually influence on reflectance spectra. Since the derived coefficients of the vegetation isoline depend on the biophysical parameters, the phenology is also related to the variation of the vegetation isoline.

Significant efforts have been devoted toward deriving useful analytical formulas based on a model of radiative energy transfer. These derivations used a representation of the top-of-canopy (TOC) reflectance spectrum consisting of photons that were directly reflected by the canopy layer. Because this portion of the reflectance spectrum does not reach the soil surface beneath the canopy, it is called the zero-th order interaction term. Photons that reached the soil surface and were reflected back to the canopy layer by the soil surface only once contributed to the measured reflectance. The 'one-time reflected' contributions comprised the first-order interaction term. Analogously, the reflectance spectrum consisting of photons reflected by the soil surface n times was defined as the n-th-order interaction term. The vegetation isoline equations were derived by truncating the second- and higher-order interaction terms. For this reason, the derived isolines are a first-order approximation of the vegetation isoline.

The approximation order determines the accuracy of the derived isoline equations. The accuracy of the isoline has been improved by deriving several approximations that considered the second-order terms. The accuracy has been improved by including higher-order terms. The drawback of this inclusion is that the analytical representation is complex. Complex representations hinder the employment of isoline formulations in applications of various types. It would be beneficial to identify ways of improving the isoline approximation accuracy while maintaining the simplicity of the derived formulation.

In a previous study, we proposed a derivation technique for satisfying these requirements simultaneously [85]. During the derivation, we included the second-order interaction term only in the near-infrared band instead of retaining the second-order term in the red band. This asymmetric approximation form dramatically improved the accuracy of the derived isoline equation.

This study advanced the investigation one step further. The objective was to introduce a technique for improving the accuracy of the asymmetric isoline equations by optimizing a single factor. The goal of this improvement was to reduce the errors in the vegetation isoline equivalent to a value equal to or smaller than the error induced by the inherent signal-to-noise ratio (SNR) of the existing sensors. The accuracy improvements obtained in this study were validated using a radiative transfer model of a system of vegetation and soil layers, the PROSAIL model [28, 72]. After optimizing a single factor in the asymmetric approximation of the vegetation isoline equation, the error levels of the improved isoline equations are discussed by comparing the resulting errors with those computed directly from the signal-to-noise ratios of four existing sensors.

3.2 Background

In this section, two forms of the vegetation isoline equation are introduced. The magnitudes of the errors in the isoline equations differed between the two equations and were characterized numerically.

3.2.1 Two approximations of the vegetation isoline equations

The simplest form of the vegetation isoline equation was derived by truncating the soil–canopy interaction terms at the first-order (single interaction) [37]. The resulting equation was simple, which is advantageous for various applications [41, 42, 62, 65–68, 70, 71, 86]. The first-order isoline equation may be written (with the truncation term ϵ_1) as:

$$\rho_N = a\gamma_1\rho_R + D_1 + \epsilon_1, \tag{3.1}$$

where γ_1 and D_1 are defined by:

$$\gamma_1 = \frac{\overline{T_N^2}}{\overline{T_R^2}}, \tag{3.2}$$

$$D_1 = b\overline{T_N^2} + \omega\left(\rho_{vN} - a\gamma_1\rho_{vR}\right). \tag{3.3}$$

The fraction of vegetation cover (FVC) is represented by ω, and the variables ρ_R and ρ_N represent the TOC reflectance in the red and NIR bands, respectively. The variables ρ_{vR} and ρ_{vN} represent the 'pure' canopy reflectances independent of the soil surface beneath the canopy layer. Finally, $\overline{T_R^2}$ and $\overline{T_N^2}$ represent the area-averaged two-way transmittances (T_R^2 and T_N^2), defined by:

$$\overline{T_R^2} = \omega T_R^2 + 1 - \omega, \tag{3.4}$$

$$\overline{T_N^2} = \omega T_N^2 + 1 - \omega. \tag{3.5}$$

These variables are explained in additional detail elsewhere [41, 62, 85].

The second form of the vegetation isoline was derived by only including the interaction terms up to the second-order in the NIR band. The interaction terms in the red band could be expressed using the first-order terms. The asymmetric-order of the approximation in the two bands significantly reduced the error in the isoline relative to the first-order form. The asymmetric form of the vegetation isoline may be written (with the truncation term ϵ_2) as

$$\rho_N = a^2 \zeta \rho_R^2 + a\gamma_2 \rho_R + D_2 + \epsilon_2, \tag{3.6}$$

using the definitions:

$$\zeta = \omega T_N^2 R_{vN} / (\overline{T_R^2})^2, \tag{3.7}$$

$$\gamma_2 = \gamma_1 + \delta_1, \tag{3.8}$$

$$D_2 = D_1 + \delta_0, \tag{3.9}$$

$$\delta_0 = \zeta \left(b\overline{T_R^2} - \omega a \rho_{vR} \right)^2, \tag{3.10}$$

$$\delta_1 = 2\zeta \left(b\overline{T_R^2} - \omega a \rho_{vR} \right). \tag{3.11}$$

The variable R_{vN} represents the bi-hemispherical reflectance of the canopy layers at the bottom surface, which appears only in the NIR band.

3.2.2 Errors in the vegetation isoline equations

The asymmetric approximation of the vegetation isoline achieved greater accuracy than the first-order approximation. This fact could be confirmed by conducting a set of numerical simulations and plotting the errors of the two approximated forms. The errors of the two approximated isolines (the first-order and asymmetric-order approximations) were computed assuming a fully covered vegetation canopy, where the value of FVC was set to unity. The PROSAIL model was used to simulate the TOC reflectance by varying the leaf area index (LAI) and soil reflectance spectra (from dark to bright soil). Figure 3.1(a), (b) show plots of the error in the first-order isoline and the asymmetric isoline, respectively, as a function of the LAI and soil reflectance. The error in the first-order isoline reached 0.01 in reflectance units as the soil reflectance increased. By contrast, the error in the asymmetric-order isoline was much smaller than that in the first-order approximation, nearly one order of magnitude smaller, as summarized in our previous study [85].

We next focused on testing whether the accuracy of the asymmetric approximation was satisfactory from a parameter retrieval point of view. This point was examined

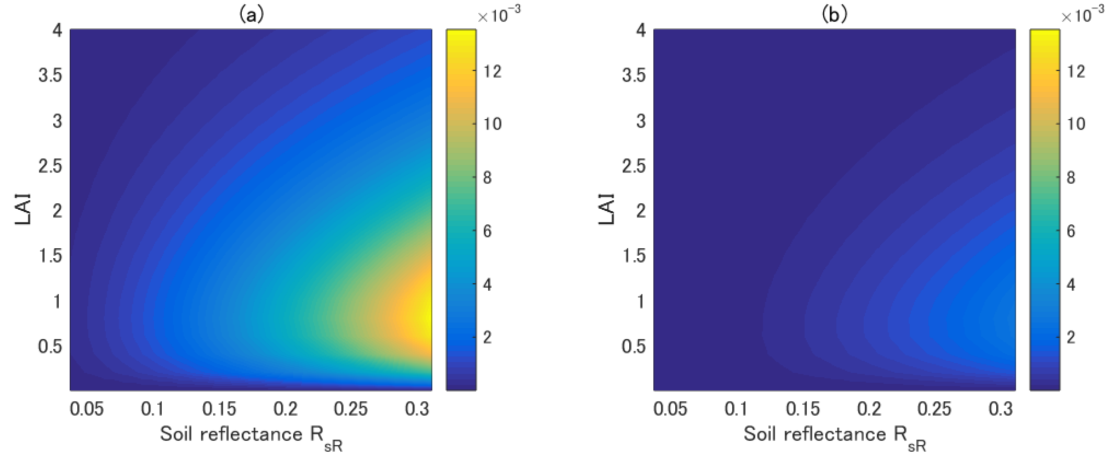

Figure 3.1: (**a**) Error in the first-order isoline; and (**b**) error in the asymmetric-order isoline. LAI: leaf area index

by comparing the isoline errors with an error equivalent to the noise level in the reflectance measurements. The comparison was implemented by assuming a simple scenario such that the value of the SNR in the NIR reflectance was 200 and the average value of the NIR reflectance was 0.1 over the entire parameter range. Although this assumption was made for the sake of simplicity, it was a rather conservative assumption because the averaged NIR reflectance is expected to exceed 0.1 in most cases. Under these assumptions, the noise equivalent error could be obtained as 0.0005 in reflectance units over the entire parameter range. With this quick estimate of the noise equivalent error, Figure 3.2 shows the contour plots of the errors in the first-order approximation (left) and in the asymmetric-order approximation (right). The contour lines that corresponded to the value of 0.0005 are emphasized by thicker black lines in the figures. These results indicated that the error in the first-order approximated isoline mostly exceeded the noise equivalent error for the majority of the cases (represented by the combinations of the LAI and the soil reflectance). Although the error in the asymmetric-order approximation became much smaller than that of the first-order approximation, the errors still exceeded 0.0005, especially at higher soil reflectances. These results suggested that if the asymmetric-order approximated isoline was used for parameter retrieval, the errors in the retrieved results would be larger than the error introduced by the sensor noise. These results indicated that the accuracy of the asymmetric-order approximation required further improvement.

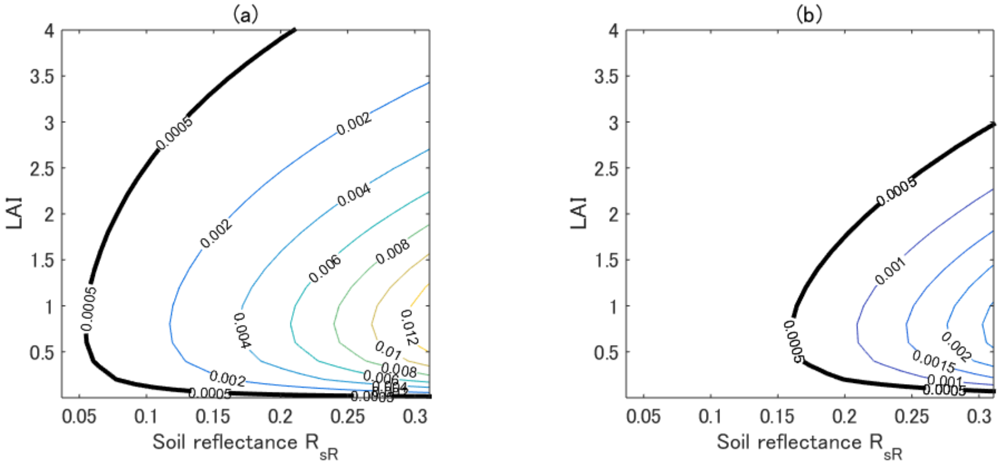

Figure 3.2: Comparison of the errors in the vegetation isolines with the error (0.0005) computed from the noise corresponding to a signal-to-noise ration (SNR) of 200 at the NIR reflectance of 0.1. The thick solid lines indicate the contour lines corresponding to 0.0005.

3.3 Approaches

Improved accuracy was achieved by including the second-order interaction term only in the NIR band. This modification shifted the first-order approximated isoline upward in the reflectance subspace. Figure 3.3 illustrates this shifting process and the mechanism by which the accuracy was improved via the asymmetric-order approximation. The degree of shifting from the first-order isoline is illustrated as the difference, along the NIR axis, between the blue line and the red line in the figure. This difference remained smaller than the difference between the first-order isoline and the true vegetation isoline (illustrated as the difference between the blue line and the black line). The gap between the asymmetric-order isoline (red line) and the true isoline (black line) must be minimized to achieve the highest accuracy, which this study attempts to address.

This gap could be analytically evaluated by clarifying the difference between the first-order and the asymmetric-order isoline equations. The asymmetric-order approximation form of the vegetation isoline was obtained by neglecting the higher-order interaction term ϵ_2 from Equation (3.6). The definition of γ_2, Equation (3.8), was used to express the isoline equation as:

$$\rho_N \approx a^2\zeta\rho_R^2 + a\gamma_1\rho_R + a\delta_1\rho_R + D_1 + \delta_0. \tag{3.12}$$

After rearranging Equation (3.12) by noting the form of the first-order isoline

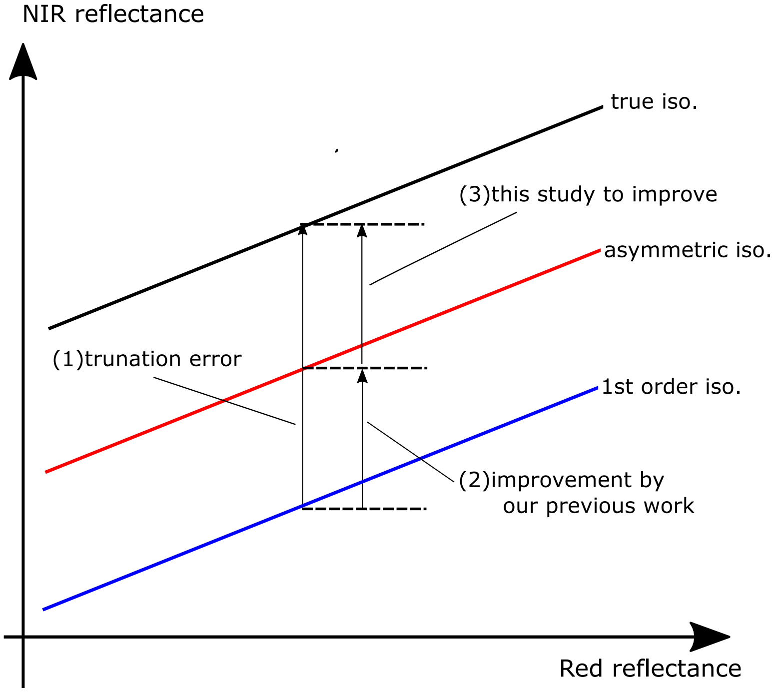

Figure 3.3: Illustration of the truncation error in the vegetation isoline equations and its improvement by this and previous studies.

Equation (3.1), the above equation could be transformed to

$$\rho_N \approx a\gamma_1\rho_R + D_1 + \left(a^2\zeta\rho_R^2 + a\delta_1\rho_R + \delta_0\right). \tag{3.13}$$

The term in the parentheses on the right-hand-side represents the contribution of the asymmetric second-order term, illustrated as the distance between the blue line and the red line in Figure 3.3. Equation (3.13) suggests that an adjustment to this distance (overcorrection term) could fill the gap between the red line and the black line, further improving its accuracy.

One way to adjust the overcorrection term is to introduce a factor into the last term of Equation (3.13). The factor (represented by k) introduced into the last term of Equation (3.13) could be explicitly introduced in the equation,

$$\rho_N \approx a\gamma_1\rho_R + D_1 + k\left(a^2\zeta\rho_R^2 + a\delta_1\rho_R + \delta_0\right). \tag{3.14}$$

Solving Equation (3.14) for k, we have:

$$k = \frac{\rho_N - (a\gamma_1\rho_R + D_1)}{a^2\zeta\rho_R^2 + a\delta_1\rho_R + \delta_0}. \tag{3.15}$$

The value of k could be computed from Equation (3.15) for each combination of the model input parameter used for the reflectance simulation. For example, selecting LAI, FVC, and the soil reflectance of the red band R_{sR} as the set of parameters to be varied during the simulation, with the number of grids for each parameter set to 21, a total of 9261 distinctive values of k will be obtained. Because k depends on a set of parameters, the most accurate way to adjust this scenario is to model the variations in k as a function of all parameters. Such an algorithm, however, is not practical to implement at this stage of investigation because one must estimate all input parameters prior to determining k. Specifically, LAI, FVC, and the soil reflectance must be estimated to determine k. The adjustment approach may be made more practical by determining the optimum constant for k according to the following approach, finding a constant value for k that minimizes the error of the adjusted isoline, Equation (3.14), over the entire range of the input parameters. This constant is considered to be the optimum value of k, denoted by k_{opt} in this study.

3.4 Results of the Numerical Simulations

3.4.1 Parameter settings for the numerical experiments

The variables used in a series of numerical simulations were computed using the canopy radiative transfer code, PROSAIL [72], which consists of the leaf optical properties model (PROSPECT) [75] and the canopy reflectance model (SAIL) [87]. The parameter settings in the simulations are summarized in Table 3.1. LAI, FVC, and the soil brightness (soil factor) were varied in this study. LAI was varied from 0.0 to 4.0 in 0.2 increments (21 intervals). The soil factor was varied from 0.0 to 1.0 in 0.05 increments (21 variations), which were used to change the mixture ratio of the reflectance spectra of the wet and dry soil provided with the code. The canopy reflectance spectra obtained using PROSAIL were linearly mixed with the soil spectra using the fraction of vegetation cover (FVC), ω, as the weight that was varied from 0.0 to 1.0 in 0.05 increments (21 intervals). The results section focuses on the use of a Spherical model to represent the leaf angle distribution (LAD), with the exception of the simulations presented in Section 3.4.6, which employs five LAD models (planophile, erectophile, plagiophile, extremophile, and uniform) to examine the effects of the LAD on our simulations. The input parameters in PROSAIL, including the other parameters fixed in this study, are listed in Table 3.1. The total number of spectra was 9261 (21×21×21) for a single LAD. (The parameter grids are finer than in our previous study [85].) We employed 655 nm and 865 nm reflectance spectra for the red and NIR wavelength regions, which corresponded to the center of the red and

NIR bands in the Landsat 8 Operational Land Imager (OLI).

Table 3.1: Input parameters used in the numerical simulations.

Geometry	
Solar zenith angle	30°
Observation zenith angle	10°
Relative azimuth angle	0°
Pixel Heterogeneous Property	
Fraction of vegetation cover (FVC)	0.0–1.0
Canopy Properties	
Leaf area index (LAI)	0.0–4.0
Hotspot size parameter	0.01
Leaf Structural and Chemical Properties	
Leaf angle distribution (LAD)	Spherical, Planophile, Erectophile Plagiophile, Extremophile, Uniform
Leaf mesophyll structure	1.5
Chlorophyll-a and -b	40 $\mu g/cm^2$
Carotenoid content	8 $\mu g/cm^2$
Leaf mass per area	0.009 g/cm^2
Equivalent water thickness	0.01 cm
Brown pigment content	0
Soil Properties	
Wet soil reflectances at 655 and 865 nm	0.037 and 0.071
Dry soil reflectances at 655 and 865 nm	0.311 and 0.412
Soil factor (mixture ratio of wet and dry soils)	0.0–1.0 [0.0: wet soil; 1.0: dry soil]

3.4.2 Numerical procedure used for the isoline parameter retrieval

The parameters in the isoline equations were computed according to the procedures reported previously [37, 85]. $T_{v\lambda}^2$ and $\rho_{v\lambda}$ were determined based on two hypothetical simulations. First, $\rho_{v\lambda}$ was computed using spectrally flat zero reflectances of the soil surface. Subsequently, $T_{v\lambda}$ was approximated using simulated reflectances and a median reflectance of the soil surface, and $\rho_{v\lambda}$ was computed in previous step [37]. The parameter R_{vN}, which was required for the computation of ξ, was obtained by conducting an additional simulation in which the soil spectrum was even brighter than was assumed in the simulation used to compute $T_{v\lambda}$. The soil spectrum was also spectrally flat in this case [85]. In the simulation, the TOC canopy reflectances in the NIR were approximated using first- and second-order interaction terms between the canopy layer and the soil surface,

$$\rho_N \approx \omega \rho_{vN} + \overline{T_N^2} R_{sN} + \omega T_N^2 R_{vN} R_{sN}^2. \tag{3.16}$$

where R_{sN} represents the bi-hemispherical reflectance of the soil surface for the NIR band. R_{vN} was then derived by solving Equation (3.16) for R_{vN}. The isoline parameters for the canopy layer were obtained using these variables. The slope and offset of the soil line equation over the red and NIR reflectance spaces used in the isoline parameters were obtained from a linear regression of the reflectance spectra for the wet and dry soils, shown in Table 3.1 ($a = 1.24$ and $b = 0.026$).

3.4.3 Variations in k

The dependences of LAI, FVC, and R_{sR} on k were analyzed based on numerical experiments in which the k-value was computed in the previous step using Equation (3.15). Three experimental conditions were applied to compute k: (1) FVC was varied using three pairs of fixed LAI and R_{sR} values; (2) LAI was varied using three pairs of fixed FVC and R_{sR} values; and (3) R_{sR} was varied using three pairs of fixed FVC and LAI values. The results of the first case are shown in Figure 3.4(a). The k-values are plotted against FVC for "LAI = 1.0 and R_{sR}=0.1", "LAI = 2.0 and R_{sR} = 0.1", and "LAI = 2.0 and R_{sR} = 0.2", denoted by the solid, dashed, and dotted lines, respectively. The k-values were relatively insensitive to the changes in FVC. The differences between the k values for FVC = 0.0 and FVC = 0.9 were less than 1%, and the differences for FVC = 0.0 and FVC = 1.0 were less than 3% for each pair of LAI and R_{sR}. The strong dependence of R_{sR} on k was identified from the large differences between the k-value curves obtained at R_{sR} = 0.1 and = 0.2.

Similarly, the k-values were relatively insensitive to LAI, as shown in Figure 3.4(b) (results are shown for the second experimental case). These k-values are plotted against LAI for "FVC = 0.3 and R_{sR} = 0.1", "FVC = 1.0 and R_{sR} = 0.1", and "FVC = 1.0 and R_{sR} = 0.2", respectively. The differences between the k-values for LAI = 0.0 and LAI = 4.0 were less than 5%. The differences between the results obtained for R_{sR} = 0.1 and = 0.2 were similarly large, as shown in Figure 3.4(a).

Figure 3.4(c) presents the results obtained from the third case, which described the k-values along R_{sR} for "FVC = 0.3 and LAI = 1.0", "FVC = 0.3 and LAI = 2.0", and "FVC = 1.0 and LAI = 2.0", respectively. The k-values showed an approximately 50% increase (from 0.90 to 1.35) with increasing R_{sR}. The differences among the three pairs of LAI and FVC affected the k-value to a much smaller degree than did the differences between the maximum and minimum R_{sR} values. These results indicated that the k-values depended heavily on R_{sR} but were nearly independent of FVC and LAI (greenness level of the vegetation canopy).

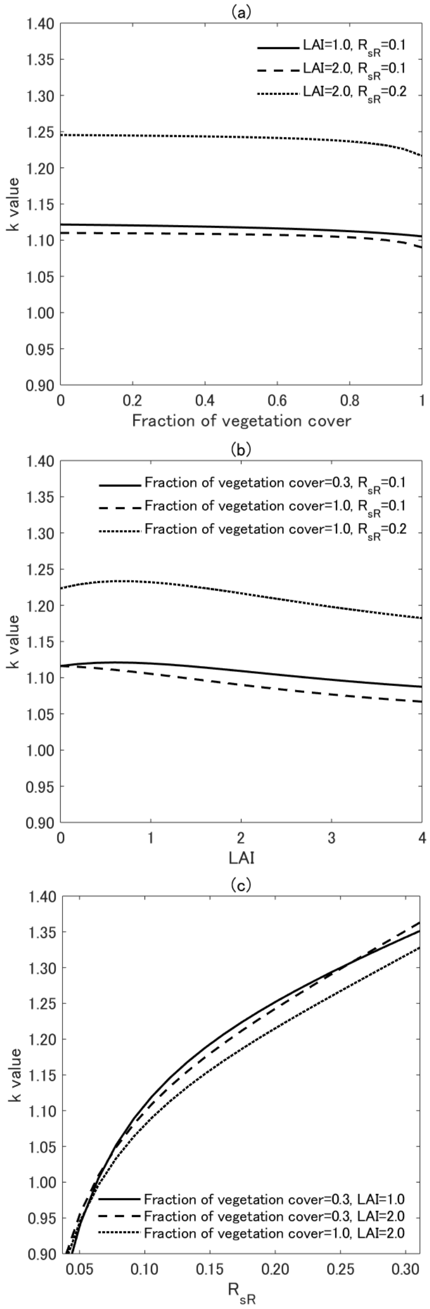

Figure 3.4: (**a**) Plot of the k-values along with the FVC over three pairs of fixed LAI and R_{sR} (LAI = 1.0 and $R_{sR} = 0.1$, LAI = 2.0 and $R_{sR} = 0.1$, and LAI = 2.0 and $R_{sR} = 0.2$); (**b**) Plot of the k-values along with LAI over three pairs of fixed FVC and R_{sR} (FVC = 0.3 and $R_{sR} = 0.1$, FVC = 1.0 and $R_{sR} = 0.1$, and FVC = 1.0 and $R_{sR} = 0.2$); (**c**) Plot of the k-values along with R_{sR} over three pairs of fixed FVC and LAI (FVC = 0.3 and LAI = 1.0, FVC = 0.3 and LAI = 2.0, and FVC = 1.0 and LAI = 2.0).

3.4.4 Optimum k-values (k_{opt})

The k-values were computed using all possible pairs of the input parameters (FVC, LAI, and R_{sR} were changed; LAD was fixed to a spherical model; and all other input parameters were fixed, as shown in Table 3.1). The optimum value of k was then determined by computing the distances (ϵ) as the errors between the true spectra $\boldsymbol{\rho}$ (including all the higher-order terms) and the vegetation isolines (the adjusted asymmetric isolines by Equation (3.14)),

$$\epsilon(k) = min(\|\boldsymbol{\rho} - \hat{\boldsymbol{\rho}}(k)\|_2), \tag{3.17}$$

where $\hat{\boldsymbol{\rho}}(k)$ denotes the spectra on the vegetation isolines for the k-value as the input. Note that $\epsilon(k)$ for $k = 0$ and $k = 1$ corresponds to the error of the first-order vegetation isoline and the asymmetric-order vegetation isoline without optimization, respectively. More than 9261 values of k were obtained using Equation (3.15), and each k was used to compute ϵ for 9261 patterns of the reflectance spectra. A two-dimensional array of ϵ values with a size of 9261 (spectral dimension) × 9261 (k-value dimension) was obtained. Figure 3.5 plots the values of ϵ averaged along the spectral dimensions as a function of the k-values. The error ϵ decreased until the k-value reached 1.25–1.30 and changed to an increasing function upon further increases in the k-value.

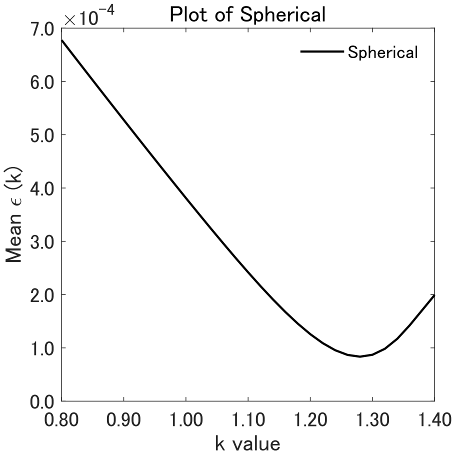

Figure 3.5: Plot of the mean value of ϵ versus the k-value.

The optimum values of k, k_{opt} were identified as follows: Six variations in the k-value were assumed: 1.25, 1.26, 1.27, 1.28, 1.29, and 1.30; the errors were approximated using the 9261 spectral patterns, that is, ϵ were computed for each k-value. The mean, standard deviation (STD), and maximum of ϵ for each k-value were computed and are summarized in Table 3.2. The minimum values of the mean ϵ were 8.35×10^{-5} for $k = 1.28$. The values of the STD for $k = 1.29$ were, however, smaller than those obtained for $k = 1.28$. The same applied to the maximum. Accordingly, the optimum k-value, k_{opt}, was determined to be 1.29 for the Spherical LAD in this study.

Table 3.2: Statistics of $\epsilon(k)$ for k = 1.25, 1.26, 1.27, 1.28, 1.29, and 1.30. STD: standard deviation.

	LAD: Spherical					
	1.25	1.26	1.27	1.28	1.29	1.30
Mean	9.06×10^{-5}	8.68×10^{-5}	8.44×10^{-5}	8.35×10^{-5}	8.43×10^{-5}	8.71×10^{-5}
STD	1.08×10^{-4}	9.54×10^{-5}	8.44×10^{-5}	7.58×10^{-5}	7.05×10^{-5}	6.89×10^{-5}
MAX	7.05×10^{-4}	6.36×10^{-4}	5.66×10^{-4}	4.97×10^{-4}	4.31×10^{-4}	3.66×10^{-4}

3.4.5 Evaluation of $k_{opt} = 1.29$

The validity of using $k_{opt} = 1.29$ was then evaluated using contour plots of ϵ over LAI and R_{sR} space, holding FVC fixed at unity. Four variations of k (1.00, 1.25, 1.29, and 1.30) were considered. In Figure 3.6(a), the minimum value of ϵ for $k = 1.0$ was 0.0002, and the errors were greater than those obtained under other conditions, as shown in Figure 3.6. Figure 3.6(b) presents results obtained for $k = 1.25$ and reveals that ϵ was less than 0.00015 for R_{sR} <0.26. ϵ, however, it increased with increasing R_{sR}, especially for $R_{sR} > 0.26$ and for LAI approaching 1.0. Figure 3.6(c) shows that for $k = 1.29$, the maximum of ϵ was approximately 0.00025. Overall, ϵ was small across the entire parameter space. The results of ϵ obtained for $k = 1.30$ were slightly larger than the values obtained for $k = 1.29$ although ϵ was small for $R_{sR} > 0.26$.

The error across the entire parameter space (e.g., the mean value of ϵ) was smallest for $k = 1.29$ (Figure 3.6(c) and Table 3.2), although ϵ for $k = 1.25$ was less than the value obtained for other k-values for R_{sR} <0.26 (Figure 3.6(b)), and ϵ was smallest for $k = 1.30$ for R_{sR} >0.26 (Figure 3.6(d)). This experiment, therefore, validated the use of the optimum k-value, k_{opt} (=1.29) for minimizing the overall error in the predicted NIR reflectances based on the adjusted asymmetric isoline equation. Furthermore, the value of ϵ for $k_{opt} = 1.29$, as shown in Figure 3.6(c), was small relative to the noise equivalent error (0.0005).

We next computed the statistical profile of the errors in the first-order, the asymmetric-order, and the adjusted asymmetric-order ($k_{opt} = 1.29$) isoline equations.

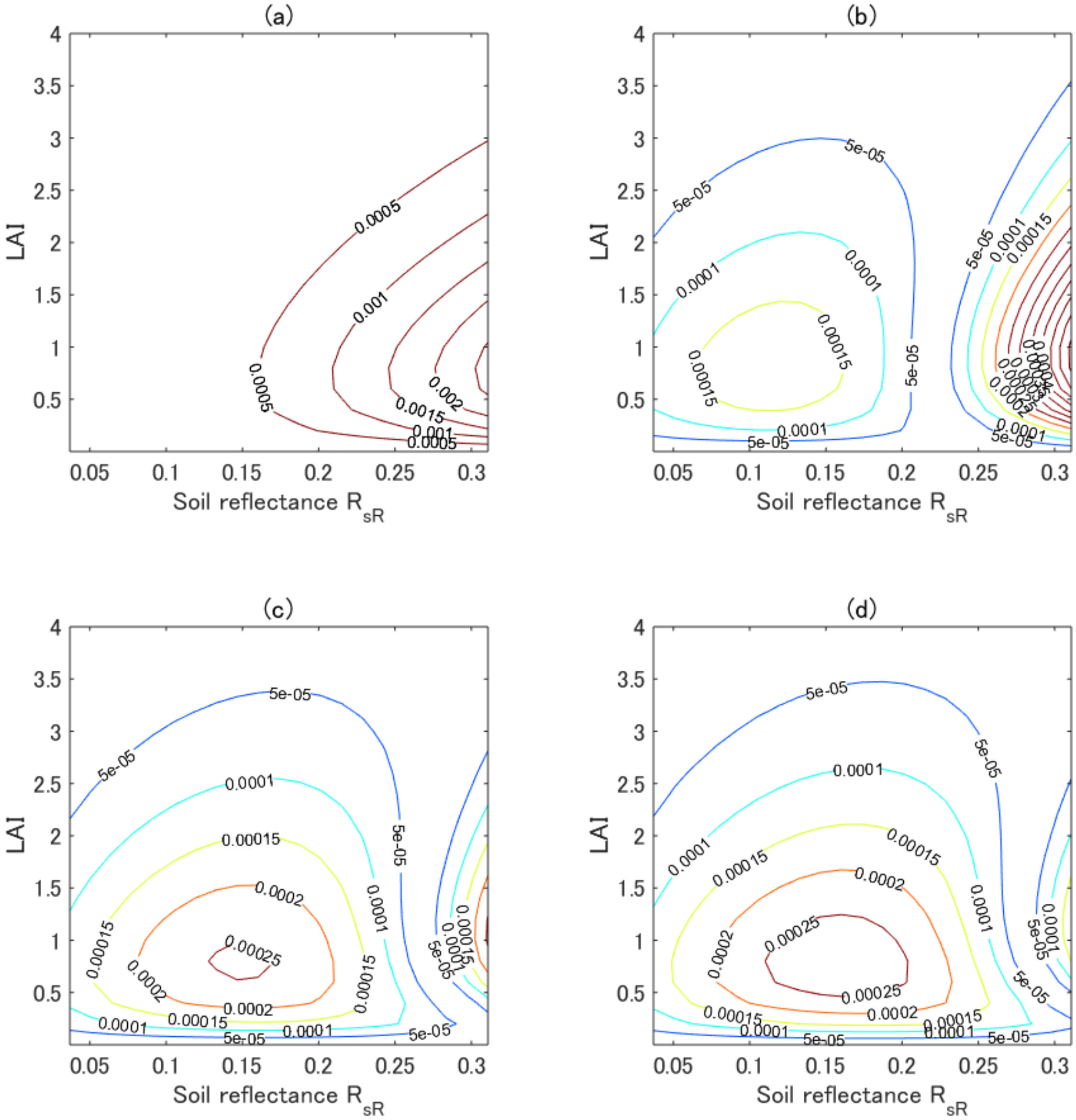

Figure 3.6: (**a**) Contour plot of ϵ over LAI and R_{sR} space for $k = 1.00$; (**b**) Contour plot of ϵ for $k = 1.25$; (**c**) Contour plot of ϵ for $k = 1.29$; (**d**) Contour plot of ϵ for $k = 1.30$.

Table 3.3 lists the mean, STD, and maximum approximation error in the isoline equations. The mean values of the errors for the adjusted asymmetric-order isoline equations were reduced to 4% and 22% of the value obtained from the first-order and the asymmetric-order isoline equations. Likewise, the STD and maximum of the errors in the adjusted asymmetric-order isoline equations were much smaller than those obtained from other isoline equations. The statistical distribution of the errors in the adjusted asymmetric isoline equations did not exceed the noise equivalent errors (0.0005), even in the case of the maximum error.

Table 3.3: Statistics of the errors in first-order, asymmetric-order, and adjusted asymmetric-order ($k_{opt} = 1.29$) isoline equations.

	LAD: Spherical				
	First-Order	**Asymmetric**	**Adjusted Asymmetric**	**adj./first**	**adj./asym.**
Mean	2.10×10^{-3}	3.81×10^{-4}	8.43×10^{-5}	4.0%	22.1%
STD	2.43×10^{-3}	5.06×10^{-4}	7.05×10^{-5}	2.9%	13.9%
MAX	1.35×10^{-2}	2.67×10^{-3}	4.31×10^{-4}	3.2%	16.1%

3.4.6 Evaluation of $k_{opt} = 1.29$ for various LADs and variations in the optimum k-value

The performances of the derived isoline equations for $k_{opt} = 1.29$ were evaluated over various LADs in PROSAIL, including planophile, erectophile, plagiophile, extremophile, and uniform distributions, respectively. Table 3.4 lists the statistical analysis associated with approximating errors in the isoline equations (mean, STD, and maximum). The statistical distribution of the planophile was nearly identical to that of the Spherical model, as shown in Table 3.3. In other LADs, the statistical distributions of the derived equations were nearly equal to or more than half of the corresponding distributions of the other isoline equations. Also, although the maximum errors could exceed the noise equivalent error (0.0005), the mean values of the errors were less than 0.0004 for all LADs. This fact indicated that the adjusted asymmetric isoline equations with $k_{opt} = 1.29$ provided acceptable results, regardless of the choice of LAD.

The optimum values of k for the various LADs were explored using the algorithm presented in Section 3.4.4. The approximation errors ϵ with size of 9261 (spectral dimension) × 9261 (k-value dimension) were computed for each LAD, and the values of ϵ averaged along the spectral dimensions were computed and plotted as a function of the k-value for each LAD. Figure 3.7 plots the mean ϵ versus k-value for the various LADs. The k-values that provided the minimum value of the mean ϵ were approximately 1.2–1.3, except for the erectophile model, indicating that the minimum value of the mean ϵ occurred for $k > 1.5$.

Table 3.5 lists the optimum k-value and mean, STD, and maximum ϵ, where $\hat{\rho}_N$ was computed using the optimum k-value for each LAD obtained in our simulations. The mean values of the errors were approximately equal to or smaller than 0.0001. The magnitude of the STD of the errors was similar to that of mean. The maximum value of the errors was less than the noise equivalent error (0.0005), except for the erectophile model. The appropriate selection of the optimum k-value thus led to an accurate prediction of the NIR reflectances, but the use of $k_{opt} = 1.29$ provided an acceptable accuracy in terms of the SNR, even though this accuracy was not optimal for each LAD.

3.4.7 Comparison with the noise-equivalent errors in satellite sensors

This study sought to decrease the errors associated with predicting the NIR reflectances by using red reflectances in the vegetation isoline equations. The goal was to decrease the errors to the level of the intrinsic errors of the sensor SNR values. Therefore, the errors in the first-order, the asymmetric-order, and the adjusted asymmetric isoline equations with $k_{opt} = 1.29$ were compared with the error arising from the SNR of the Earth observation sensors currently in space orbit. We employed the SNRs of four sensors, including the Aqua-Moderate Resolution Imaging Spectroradiometer (MODIS) [88], the Landsat 8-Operational Land Imager (OLI) [89], the Greenhouse Gases Observing Satellite (GOSAT)-Cloud and Aerosol Imager (CAI) [90], and the Suomi National Polar-orbiting Partnership (SNPP)-Visible Infrared Imaging Radiometer Suite (VIIRS) [91], as summarized in Table 3.6.

The ratio of the relative errors in the isoline equations to the sensor SNR (r) was computed according to:

$$r = \frac{\epsilon(k)}{(\rho_N/SNR)} \tag{3.18}$$

The isoline equations were superior to the noise equivalent errors for values of less than unity, whereas the equations were inferior to the noise equivalent errors for values greater than unity. For comparison, the FVC and LAD were fixed, respectively, to unity and spherical.

Figure 3.8 plots r over the LAI-R_{sR} space. Thicker black lines correspond to r = 1.0. MODIS, OLI, CAI, and VIIRS correspond to the four rows of Figure 3.8

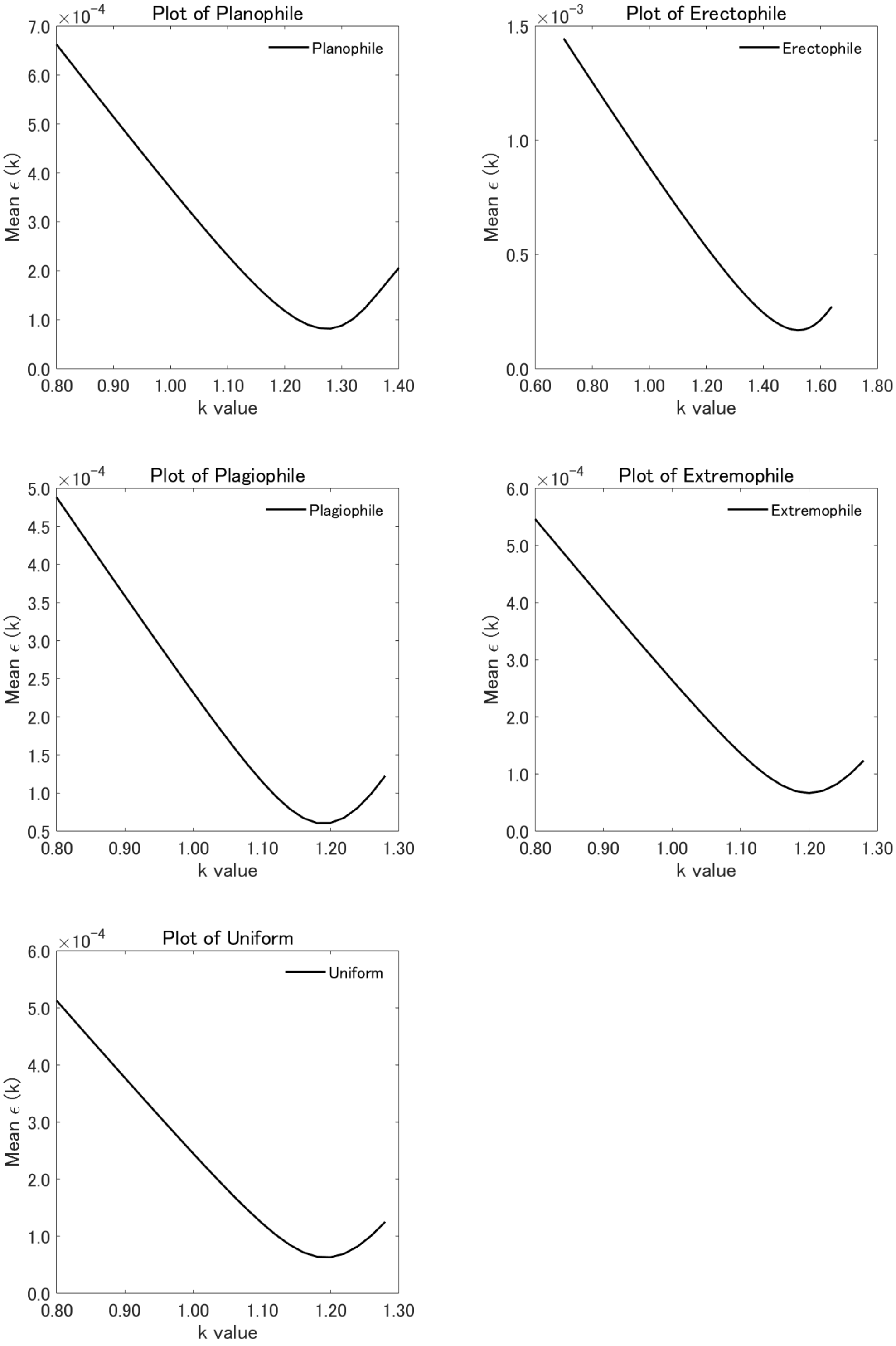

Figure 3.7: Plot of the mean ϵ as a function of the k-value for the planophile, erectophile, plagiophile, extremophile, and uniform LADs, respectively.

Table 3.4: Statistical distributions of the errors in the first-order, asymmetric-order, and adjusted aymmetric-order ($k_{opt} = 1.29$) isoline equations for the five LADs, including planophile, erectophile, plagiophile, extremophile, and uniform distributions.

	LAD: Planophile				
	first-order isoline	asymmetric isoline	adjusted isoline	adj./1st	adj./asym.
Mean	2.07×10^{-3}	3.69×10^{-4}	8.39×10^{-5}	4.1%	22.7%
STD	2.40×10^{-3}	4.91×10^{-4}	6.76×10^{-5}	2.8%	13.8%
MAX	1.34×10^{-2}	2.59×10^{-3}	3.79×10^{-4}	2.8%	14.6%
	LAD: Erectophile				
	first-order isoline	asymmetric isoline	adjusted isoline	adj./1st	adj./asym.
Mean	3.08×10^{-3}	8.83×10^{-4}	3.89×10^{-4}	12.6%	44.1%
STD	3.54×10^{-3}	1.12×10^{-3}	5.53×10^{-4}	15.6%	49.4%
MAX	1.87×10^{-2}	5.79×10^{-3}	2.95×10^{-3}	15.8%	50.9%
	LAD: Plagiophile				
	first-order isoline	asymmetric isoline	adjusted isoline	adj./1st	adj./asym.
Mean	1.71×10^{-3}	2.31×10^{-4}	1.35×10^{-4}	7.9%	58.4%
STD	2.00×10^{-3}	3.15×10^{-4}	1.24×10^{-4}	6.2%	39.4%
MAX	1.13×10^{-2}	1.62×10^{-3}	7.78×10^{-4}	6.9%	48.0%
	LAD: Extremophile				
	first-order isoline	asymmetric isoline	adjusted isoline	adj./1st	adj./asym.
Mean	1.89×10^{-3}	2.64×10^{-4}	1.37×10^{-4}	7.2%	51.9%
STD	2.19×10^{-3}	3.57×10^{-4}	1.20×10^{-4}	5.5%	33.6%
MAX	1.23×10^{-2}	1.84×10^{-3}	7.04×10^{-4}	5.7%	38.3%
	LAD: Uniform				
	first-order isoline	asymmetric isoline	adjusted isoline	adj./1st	adj./asym.
Mean	1.79×10^{-3}	2.44×10^{-4}	1.38×10^{-4}	7.7%	56.6%
STD	2.09×10^{-3}	3.32×10^{-4}	1.24×10^{-4}	5.9%	37.3%
MAX	1.17×10^{-2}	1.71×10^{-3}	7.60×10^{-4}	6.5%	44.4%

from the top to the bottom. From the left to the right column, the results of the first-order, asymmetric-order, and adjusted asymmetric-order isoline equations are plotted. The results of first-order isoline equations (Figure 3.8(a),(d),(g),(j)) indicate that r exceeded unity over a large area of parameter space. The asymmetric-order isoline equations resulted in smaller values of r and exceeded unity for relatively large values of R_{sR}; however, the areas of these parts were significantly smaller than the area observed in the first-order isoline, as shown in Figure 3.8(b),(e),(h),(k). Finally, the results of r obtained from the adjusted asymmetric-order isoline equations (Figure 3.8(c),(f),(i),(l)) revealed that r never exceeded unity, and the maximum values of r were less than 0.5 for all sensors. In summary, the errors in the adjusted asymmetric

Table 3.5: Optimum k-value and statistical distributions of the errors in the adjusted asymmetric isoline equations, with the optimal k-values for each of the five LADs, including the planophile, erectophile, plagiophile, extremophile, and uniform distributions.

LAD	**Optimum k**	**Mean**	**STD**	**MAX**
Planophile	1.28	8.17×10^{-5}	7.03×10^{-5}	4.44×10^{-4}
Erectophile	1.53	1.69×10^{-4}	1.39×10^{-4}	8.31×10^{-4}
Plagiophile	1.19	5.99×10^{-5}	6.23×10^{-5}	4.08×10^{-4}
Extremophile	1.2	6.65×10^{-5}	6.67×10^{-5}	4.40×10^{-4}
Uniform	1.20	6.31×10^{-5}	6.01×10^{-5}	3.81×10^{-4}

Table 3.6: SNR in the red and NIR bands for the Aqua-Moderate Resolution Imaging Spectroradiometer (Aqua-MODIS) [92], Landsat 8-Operational Land Imager (Landsat 8 OLI) [93], Greenhouse Gases Observing Satellite (GOSAT)-Cloud and Aerosol Imager (CAI) [94], and Suomi National Polar-orbiting Partnership (NPP)-Visible Infrared Imaging Radiometer Suite (VIIRS) [95]. SNR for MODIS band1 (red) was derived by calculating 128 (sensor design requirement) × 1.57 (ratio of measured SNR in-orbit to sensor design requirement) and SNR for MODIS band 2 (NIR) was derived by 201× 2.64 [92]. Similaly, SNR for VIIRS I1 and I2 bands (red and NIR) were derived by caluculating 119 × 1.76 and 150 × 1.5, respectively [95].

	MODIS	**Landsat8 OLI**	**GOSAT-CAI**	**VIIRS**
Red band	201	227	200	209
NIR band	530	201	200	225

isoline equations with $k_{opt} = 1.29$ were smaller than the error arising from the SNR of the four Earth observation sensors.

3.5 Discussion and Conclusions

The asymmetric-order isoline equations, derived from a previous study, were reformulated as first-order isoline equations plus a correction term multiplied by a parameter k. The derived equations with optimized k (as a constant) improved the accuracy of the asymmetric-order isoline equations while retaining the simplicity of the equations. The k-value was assumed to be a function of LAI, FVC, and R_{sR}, and the influences of R_{sR} on k were much greater than the influences of LAI and FVC such that k could be considered primarily to be a function of R_{sR}. One advantage of the isoline equations was that the parameters in the equations were independent of the soil brightness, i.e., R_{sR}; therefore, we fixed the k-value to an optimum instead of varying this parameter as a function of R_{sR}.

The errors in the adjusted asymmetric-order isoline equations were computed using k_{opt}. The errors in the reflectances predicted by the adjusted asymmetric-order isoline equations with k_{opt} were 4% and 22% of the errors predicted using the first-order and asymmetric-order isoline equations, respectively.

The value of k_{opt} was optimal for the Spherical LAD. The adjusted asymmetric-order isoline equations with k_{opt} reduced the errors significantly in the reflectances calculated using any of the six LADs defined in this study (less than half of the errors for the asymmetric-order isoline equations), although the use of the optimal k-value along with each LAD reduced the errors more significantly. In addition, the errors in the adjusted asymmetric-order isoline equations were small over the entire parameter space relative to the noise equivalent errors computed from the SNR of the satellite sensors currently in orbit (Aqua-MODIS, Landsat 8-OLI, SNPP-VIIRS, and GOSAT-CAI). The first-order and asymmetric-order isoline equations displayed both superiority and inferiority to the noise equivalent errors by relying on the canopy and soil conditions.

This study achieved its goal of reducing the error in the adjusted asymmetric-order isoline equations using a fixed k-value, yielding an error that was less than the noise equivalent errors based on the SNRs of some major satellite sensors, without complicating the isoline equations. Validation of the derived equations would require additional numerical experiments involving the application of other radiative transfer models of the vegetation canopy. Improved accuracy in the equations may be necessary if the sensor's SNR were to increase as a result of technological advancements in the sensor instrument design.

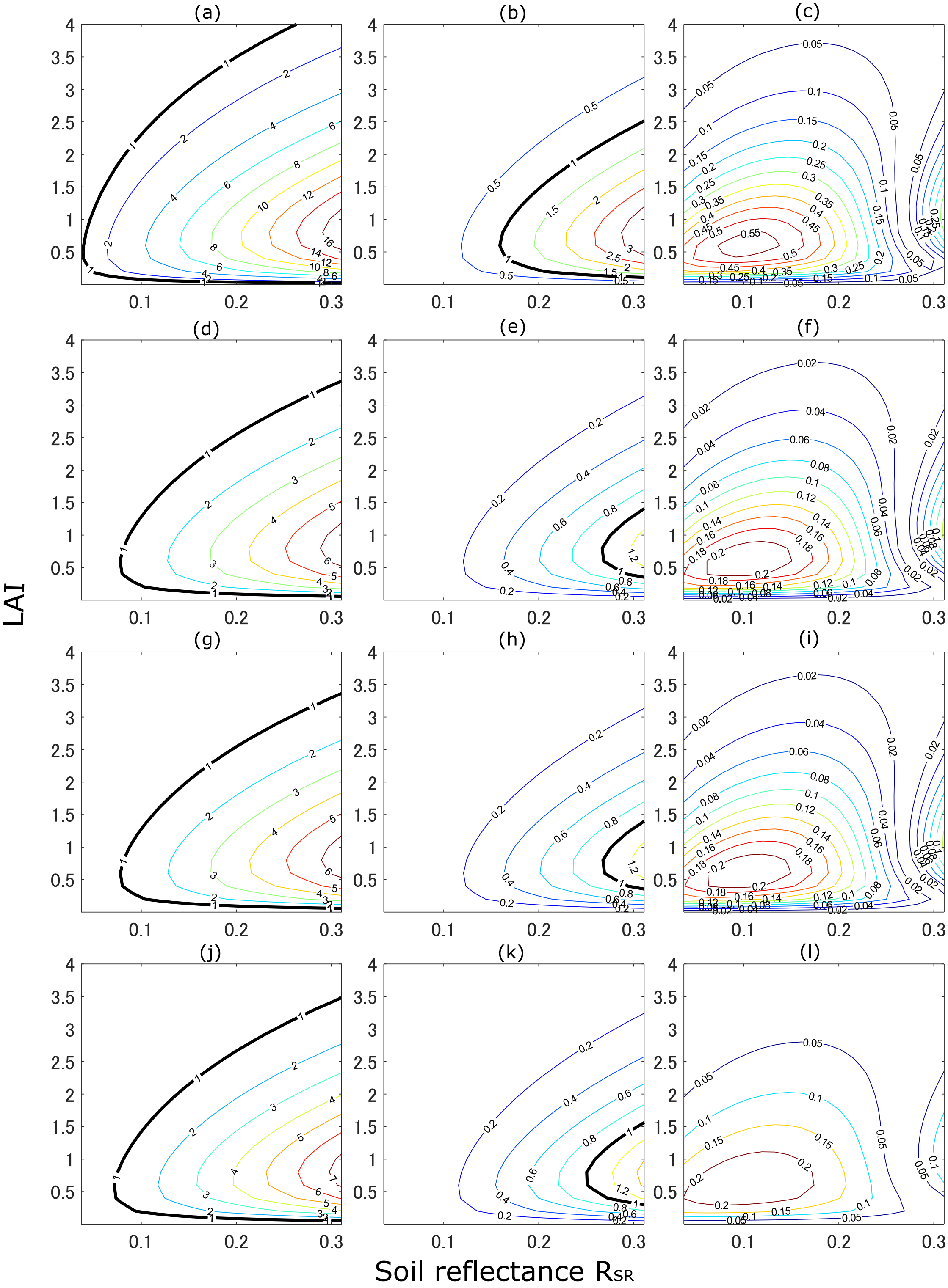

Figure 3.8: Contour plots of r over LAI-R_{sr} space. From the top to the bottom, each plot correspond to the MODIS, OLI, CAI, and VIIRS sensors, respectively. From the left to right column, each plot corresponds to the first-order, asymmetric-order, and adjusted asymmetric-order ($k_{opt} = 1.29$) isoline equations, respectively. The bold line indicates $r = 1.0$.

CHAPTER IV

Optimization Technique of Asymmetric-Order Vegetation Isoline Equations

4.1 Introduction

Remotely sensed reflectance spectra have been used to estimate biophysical parameters on terrestrial vegetation. The relationships between reflectances of two bands (e.g., red and NIR bands) are key information in the parameter retrievals and are unique to the parameters such as LAI and chlorophyll content in a leaf. Several band algebra called vegetation index (VI) based on the inter-band relationships have been developed and theoretically analyzed in previous studies that are proximity measure of biophysical parameters[23, 24, 34]. In addition, inter-band relationships have been investigated by analytical methods using vegetation isoilne equations. The vegetation isoline equations provide analytical relationships between reflectances of two bands and are capable of describing LAI isoline over two-dimensional reflectance space. The isoline equations could be used to directly retrieve biophysical parameters such as the fraction of green cover[30], LAI, and the chlorophyll content[44]. Additional applications of the inter-band relationship described by vegetation isoilne equations have been reported by numerous studies for analytically relating the VIs collected by different sensors in inter-calibration studies[42, 79].

The canopy model used for deriving vegetation isoline equations consists of a turbid medium, and top-of-canopy reflectances are represented by the adding method. The vegetation isoline equations were derived by truncating the second- and higher-order interaction terms between vegetation canopy and soil surfaces[23, 37]. The isoline equation including only the first-order interaction term is referred to as the first-order vegetation isoline equation, and its accuracy deteriorates as the brightness of the soil surface increases. In our works introduced in previous chapters, efforts have been applied toward improving the accuracy of the isoline equation while retaining its simplicity. The first step of the efforts provided asymmetric-order approximation of the vegetation isoline equations by retaining the second-order interaction term only in the NIR band [85], and the next step added only one factor to asymmetric-order vegetation isoline equation and the factor was optimized using various conditions of canopy and soil[96]. This equation with the optimized factor is called the optimized asymmetric-order vegetation isoline equation. Errors in the optimized asymmetric-order isoline equation were reduced to approximately 4% of the error of the first-order isoline equation[85] and approximately 20% of the error of the asymmetric-order isoline equation[96]. In addition, the errors in the optimized asymmetric-order isoline equations were smaller for all the conditions assumed in the previous study relative to the noise equivalent errors computed from SNR of the satellite sensors.

Accuracy improvements and evaluations of the vegetation isoline equations reported in the previous chapters were limited to the pair of red and NIR bands (central wavelengths were 655 nm and 865 nm, respectively). However, in recent years, hyperspectral sensors are available for remote sensing of Earth environment, and several hyperspectral missions are currently planned for global observations for environmental and geological remote sensing[97–100]. Such hyperspectral sensors allows us to process more than one hundred bands and to improve the accuracy of remote sensing applications. Performances of vegetation isoline equations should be evaluated to several pairs of spectral bands in solar reflective wavelength ranges in order to explorer the potential utilities and evaluate accuracy in the isoline equations for parameter retrievals on environmental applications. In this chapter, accuracy of vegetation isoline equations derived in previous chapters is evaluated in the wavelength range between 400 nm and 1200 nm using numerical simulations.

4.2 A Series of Derived Vegetation Isoline Equations

4.2.1 Vegetation isoline equations

The vegetation isoline equations derived in previous studies included first-order, asymmetric-order, and optimized asymmetric-order vegetation isoline equations as the followings.

First-order vegetation isoline equation

In first-order vegetation isoline, the second- and higher-order interaction terms were truncated in two bands (λ_1 and λ_2). The isoline equation is expressed by

$$\rho_{\lambda_2} = a\gamma_1\rho_{\lambda_1} + D_1 + \epsilon_1, \tag{4.1}$$

and γ_1 and D_1 are defined by

$$\gamma_1 = \frac{\overline{T^2_{\lambda_2}}}{\overline{T^2_{\lambda_1}}}, \tag{4.2}$$

$$D_1 = b\overline{T^2_{\lambda_2}} + \omega\left(\rho_{v\lambda_2} - a\gamma_1\rho_{v\lambda_1}\right), \tag{4.3}$$

where ω is the fraction of vegetation cover (FVC). ρ_{λ_1} and ρ_{λ_2} are top-of-canopy reflectances in the two wavelengths. $\rho_{v\lambda_1}$ and $\rho_{v\lambda_2}$ are the 'pure' canopy reflectances independent of the soil surface beneath the canopy layer. $T^2_{\lambda_1}$ and $T^2_{\lambda_2}$ represent the two-way transmittances of the vegetation canopy. The two constants, a and b, stand for the soil line slope and offset, respectively.

Asymmetric-order vegetation isoline equation

The asymmetric-order form was derived by including the interaction terms up to the second-order term in λ_2 while including the terms up to the first-order interaction in λ_1[85]. This expression is written by

$$\rho_{\lambda_2} = a^2\zeta\rho^2_{\lambda_1} + a\gamma_2\rho_{\lambda_1} + D_2 + \epsilon_2, \tag{4.4}$$

using the following definitions

$$\zeta = \omega T^2_{\lambda_2} R_{v\lambda_2} / (\overline{T^2_{\lambda_1}})^2, \tag{4.5}$$

$$\gamma_2 = \gamma_1 + \delta_1, \tag{4.6}$$

$$D_2 = D_1 + \delta_0, \tag{4.7}$$

$$\delta_0 = \zeta\left(b\overline{T^2_{\lambda_1}} - \omega a\rho_{v\lambda_1}\right)^2, \tag{4.8}$$

$$\delta_1 = 2\zeta\left(b\overline{T^2_{\lambda_1}} - \omega a\rho_{v\lambda_1}\right), \tag{4.9}$$

where $R_{v\lambda_2}$ is the bi-hemispherical reflectance of the canopy layers at the bottom surface, which appeared only in the destination band, λ_2.

Optimized asymmetric-order vegetation isoline equation

The asymmetric-order form was obtained by neglecting the higher-order interaction term ϵ_2 in Eq. (4.4),

$$\rho_{\lambda_2} \approx a^2\zeta\rho_{\lambda_1}^2 + a\gamma_1\rho_{\lambda_1} + a\delta_1\rho_{\lambda_1} + D_1 + \delta_0. \tag{4.10}$$

After rearranging Eq. (4.10) by noting the form of the first-order isoline (Eq. (4.1)), the above equation could be transformed to

$$\rho_{\lambda_2} \approx a\gamma_1\rho_{\lambda_1} + D_1 + \left(a^2\zeta\rho_{\lambda_1}^2 + a\delta_1\rho_{\lambda_1} + \delta_0\right). \tag{4.11}$$

We introduced a factor k into the last term of the right-hand-side of Eq. (4.11) to have the optimized asymmetric-order vegetation isoline as

$$\rho_{\lambda_2} \approx a\gamma_1\rho_{\lambda_1} + D_1 + k\left(a^2\zeta\rho_{\lambda_1}^2 + a\delta_1\rho_{\lambda_1} + \delta_0\right). \tag{4.12}$$

Note that the factor k will be optimized prior to evaluation for accuracy of the vegetation isoline equation, although it is variable at this point.

4.2.2 Errors in the vegetation isoline equations

The errors potentially included in three isoline equations were simulated by numerical experiments in which λ_1 and λ_2 correspond to red and NIR bands, respectively. The PROSAIL model was used to simulate the spectral reflectances and transmittances as a function of the leaf area index (LAI) and soil reflectance spectra (from dark to bright soil). Figure.4.1 shows the errors for three forms of isolines (top, middle, and bottom plots correspond to first-order, asymmetric-order, and optimized symmetric order forms, respectively.) The results for FVC=1.0 and FVC=0.5 correspond to left and right column in Fig. 4.1, respectively. The errors observed in the asymmetric-order form was smaller than that of the first-order form but increases with increasing soil brightness. The errors in the optimized asymmetric-order form were much smaller than that of other forms even if the soil brightness increases. This accuracy improvement was observed because of a single factor added and optimized into the asymmetric-order vegetation isoline equation.

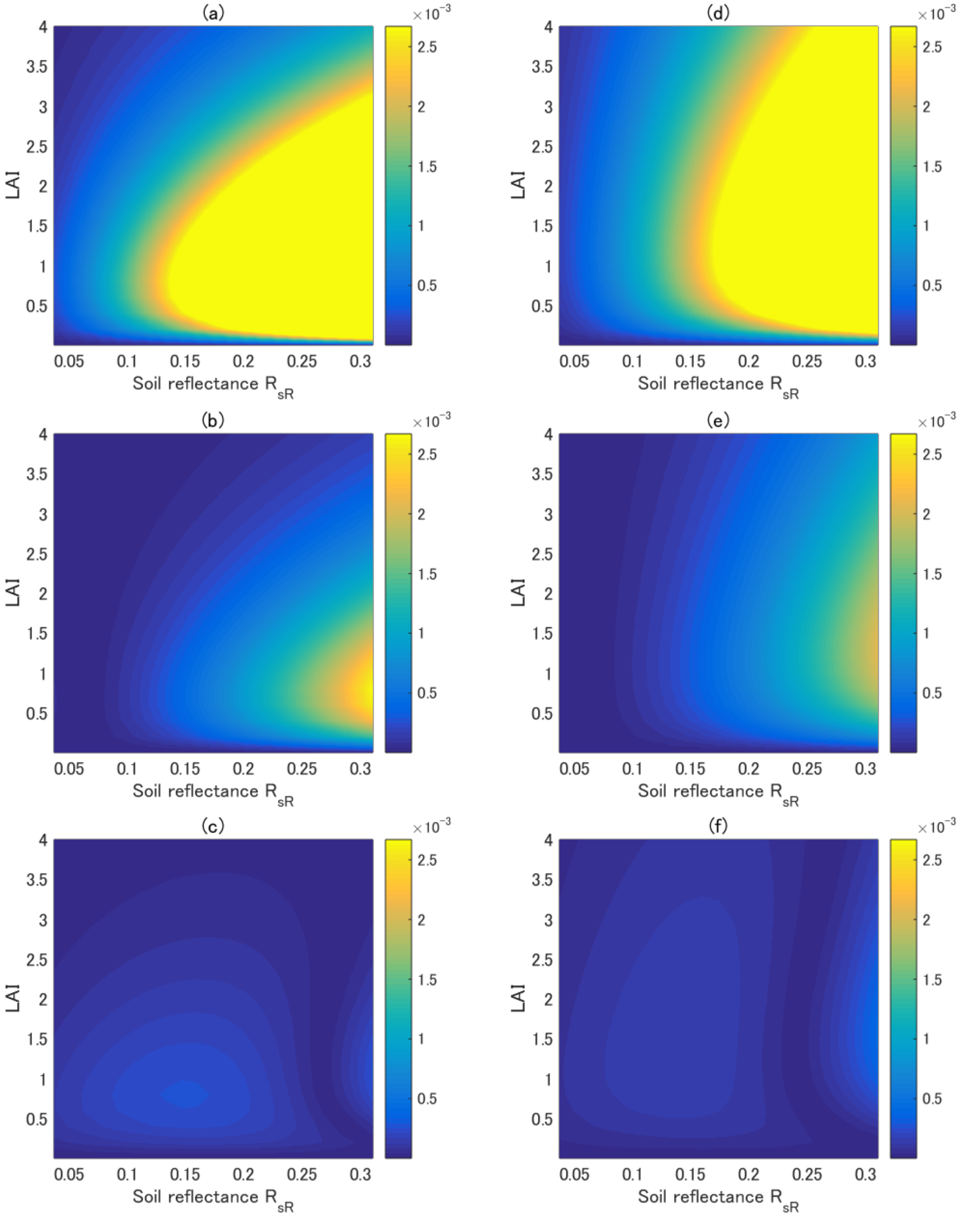

Figure 4.1: Errors in first-order (upper panels), asymmetric-order (middle panels), and optimized asymmetric-order isoline equations (bottom panels) for red and NIR wavelength pairs as a function of LAI and soil reflectances when FVC was 1.0 (left panels) and 0.5 (right panels).

4.3 Method

4.3.1 Analytical expression of k and finding optimum k for each wavelength pair

The factor, k added in the asymmetric-order isoline equation can be derived by solving Eq. (4.12) for k,

$$k = \frac{\rho_{\lambda_2} - (a\gamma_1\rho_{\lambda_1} + D_1)}{a^2\zeta\rho_{\lambda_1}^2 + a\delta_1\rho_{\lambda_1} + \delta_0}, \tag{4.13}$$

where the symbol for approximations originally included in Eq. (4.12) was replaced by the equal sign. Eq. (4.13) implies that the factor k depends on biophysical parameters as well as soil line parameters, and thus, k is not a constant. It indicates that there would be an optimum value for k that relies on biophysical and soil conditions and that such k can minimize the error in the asymmetric-order vegetation isoline.

k in Eq.(4.13) depends on the biophysical and soil line parameters; however, it is not realistic to find biophysical- and soil-condition dependent k on actual satellite data due to the difficulty in accurately estimating such parameters. Therefore, our approach for tackling this problem is to find a single value of k for each wavelength pair that minimizes the error of the isoline equation with k for various conditions of biophysical and soil line parameters using numerical simulations.

4.3.2 Parameter setting and approximation of isoline parameter in numerical experiments

Numerical simulations of vegetation isoline equations (Eqs.(4.1), (4.4), and (4.12)) were conducted with various conditions of LAI, FVC, and soil factor (soil brightness) for various wavelength pairs. The spectral band-dependent variables used in numerical simulaltions were computed using the canopy radiative transfer code, PROSAIL [72], which combined PROSPECT leaf optical properties model[75] and SAIL canopy bidirectional reflectance model[87]. The parameter settings in the simulations are shown in Table4.1. LAI was varied from 0.0 to 4.0 in 0.8 increments (6 variations). The soil factor was varied from 0.0 to 1.0 in 0.2 increments (6 variations), which were used to change the mixture ratio of the reflectance spectra of the wet and dry soil provided with the code. The canopy reflectance spectra obtained using PROSAIL were linearly mixed with the soil spectra using FVC, ω, as the weight that was varied from 0.0 to 1.0 in 0.2 increments (6 variations). The present study uses the Spherical model for leaf angle distribution (LAD). The other input parameters in PROSAIL fixed in this study, are listed in Table4.1. The total number of condition was thus 216 (6×6×6). Isoline equations for these conditions were simulated for various pairs of wavelength, λ_1 and λ_2 where λ_2 varies from 400 nm to 1200 nm in 10 nm increments while λ_1 varies from 400 nm to λ_2 minus 10 nm in 10 nm increments.

Table 4.1: Input parameters used in the numerical simulations.

Geometry	
Solar zenith angle	30°
Observation zenith angle	10°
Relative azimuth angle	0°
Pixel heterogeneous property	
Fraction of vegetation cover (FVC)	0.0-1.0
Canopy properties	
Leaf area index (LAI)	0.0-4.0
Hotspot size parameter	0.01
Leaf structural and chemical properties	
Leaf angle distribution (LAD)	Spherical
Leaf mesophyll structure	1.5
Chlorophyll-a and -b	40 $\mu g/cm^2$
Carotenoid content	8 $\mu g/cm^2$
Leaf mass per area	0.009 g/cm^2
Equivalent water thickness	0.01 cm
Brown pigment content	0
Soil properties	
Soil factor (mixture ratio of wet and dry soils)	0.0–1.0 [0.0: wet soil; 1.0: dry soil]

The algorithm for computing parameters in vegetation isoline equations is identical to that used in the previous studies for simulating vegetation isolines [37],[85],[96]. The parameter for canopy reflectance, $\rho_{v\lambda}$ was computed using spectrally flat zero reflectance of the soil surface. The two-way transmittances for vegetation canopy, $T^2_{v\lambda}$ was approximated using simulated TOC reflectance with a median reflectance of the soil surface where $\rho_{v\lambda}$ was computed in previous step[96]. In the simulation, the TOC canopy reflectances in the λ_2 were approximated using first- and second-order interaction terms between the canopy layer and the soil surface,

$$\rho_{\lambda_2} \approx \omega \rho_{v\lambda_2} + \overline{T^2_{\lambda_2}} R_{s\lambda_2} + \omega T^2_{\lambda_2} R_{v\lambda_2} R^2_{s\lambda_2}. \tag{4.14}$$

where $R_{s\lambda_2}$ represents the bi-hemispherical reflectance of the soil surface for the λ_2 band. The spherical albedo of canopy layer, $R_{v\lambda_2}$ was obtained by solving Eq. (4.14) for $R_{v\lambda_2}$ in which a soil spectrum was brighter than that for the simulation used to compute T_λ^2. The soil spectrum was also spectrally flat in this case [85]. The slope and offset of the soil line equation over the λ_1 and λ_2 reflectance spaces were obtained from a linear regression of the reflectance spectra for the wet and dry soils, shown in Table 4.1. The TOC reflectance spectra used for describing true isolines were simply the output of the PROSAIL.

4.3.3 Errors in isoline equations and finding optimum k

Errors of vegetation isoline equations were measured using the distance between true and approximated isolines ($\epsilon(k)$),

$$\epsilon(k) = ||\hat{\rho}(k) - \rho||_2, \tag{4.15}$$

where $\hat{\rho}(k)$ denotes the spectrum derived by asymmetric-order vegetation isoline equations with k. ρ denotes the spectrum on the vegetation isoline including all the higher-order interaction terms, i.e., the true spectrum. Note that first-order and asymmetric-order isoline equations corresponds to $k = 0$ and $k = 1$ in Eq.(4.12) so that errors in three isoline equations can be measured by Eq.(4.15).

The optimum value of k in Eq.(4.12) for each wavelength pair was explored based on $\epsilon(k)$. First, values of $\epsilon(k)$ in Eq.(4.15) were computed along 216 k values and 216 conditions of the surface. Therefore, the dimension of the $\epsilon(k)$ was 216 (k value variations) by 216 (surface condition variations). The two-dimensional matrix of the $\epsilon(k)$ was averaged to provide an array of the means of $\epsilon(k)$ as a function of k value, and the optimum k value, referred to as k_{opt} was determined by selecting the k value that minimized the mean of $\epsilon(k)$[96],[101].

In consequences, errors in the optimized asymmetric-order isoline equation can be evaluate by computing $\epsilon(k_{opt})$.

4.4 Results and Discussions

4.4.1 Analysis of k_{opt}

Figure 4.2 depicts values of k_{opt} as a function of λ_1 and λ_2. k_{opt} was larger than 1 when λ_1 fell in 400-710 nm and λ_2 fell in 710-1200 nm. k_{opt} was lower than 0 when λ_1 fell in 520-660 nm and λ_2 fell in 560-690 nm as well as when λ_1 fell in 1070-1150 and λ_2 fell in 1130-1200 nm. Other wavelength pairs in Fig. 4.2 resulted in k_{opt} that lies between 0 to 1.

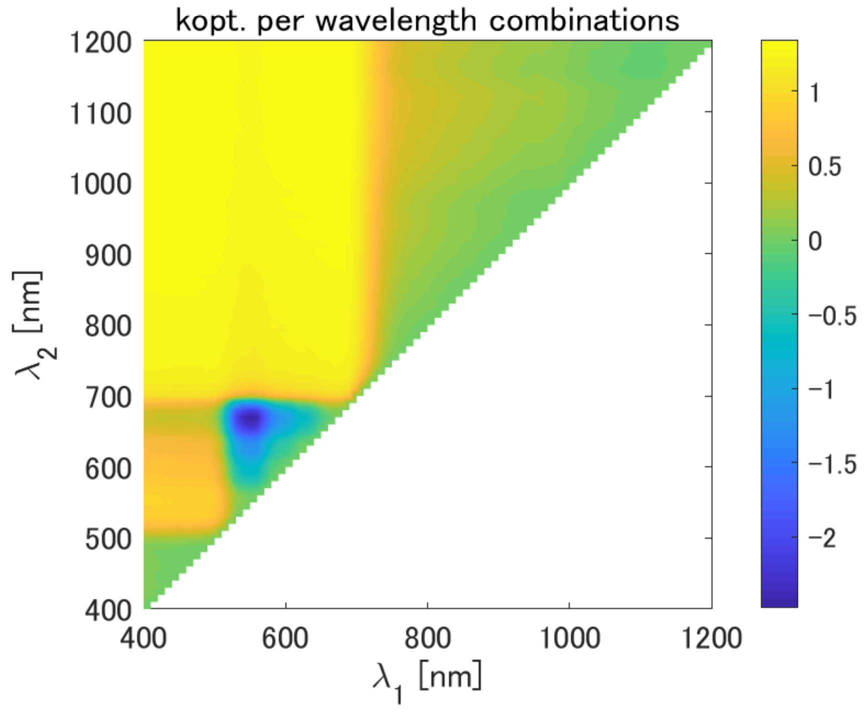

Figure 4.2: k_{opt} as a function of λ_1 and λ_2.

Figure 4.3 shows k_{opt} as a function of λ_1 for four λ_2 (800, 860, 920 and 970 nm). These wavelengths for λ_2 were selected based on bandpass filters of NIR band for Earth observation sensors. Figure 4.3(a) shows results for 400 nm $\leq \lambda_1 \leq$ 1000 nm and Figure 4.3(b) shows results for 400 nm $\leq \lambda_1 \leq$ 700 nm. k_{opt} values ranged from 1.2 to 1.4 when λ_1 was less than 700 nm, and k_{opt} rapidly decreased at approximately 700 nm and approached 0 with increasing wavelength.

Figure 4.4 shows k_{opt} as a function of λ_2 for four λ_1 (470, 510, 640, and 860 nm). Note that λ_2 was selected for horizontal axis in this case. Wavelengths chosen for λ_1 correspond to visible to near-infrared band for Japanese geostationary satellite sensor, Himawari-8 Advanced Himawari Imager (AHI). In general, a non-linear function of k_{opt} along λ_2 was observed in the results. The value of k_{opt} fell in -0.5 to 1.4 when λ_1 corresponds to visible band while k_{opt} fell in 0-0.35 when λ_1 corresponds to NIR band (Figs.4.4). Local maximum and minimum were found in the results in Fig.4.4 for the case of $\lambda_1 = 470$. The local maximum was 0.92 at about 550 nm and local minimum was 0.36 at about 670 nm. Similarly, the local maximum and minimum for $\lambda_1 = 510$ were found in the same wavelengths to $\lambda_1 = 470$, and values of the maximum and minimum were 0.73 and -0.24, respectively. No local maximum was found for $\lambda_1 = 640$ and local minimum at 670 nm was -0.49. The local maximum and minimum were observed for $\lambda_1 = 860$ but wavelengths of these extreme values were

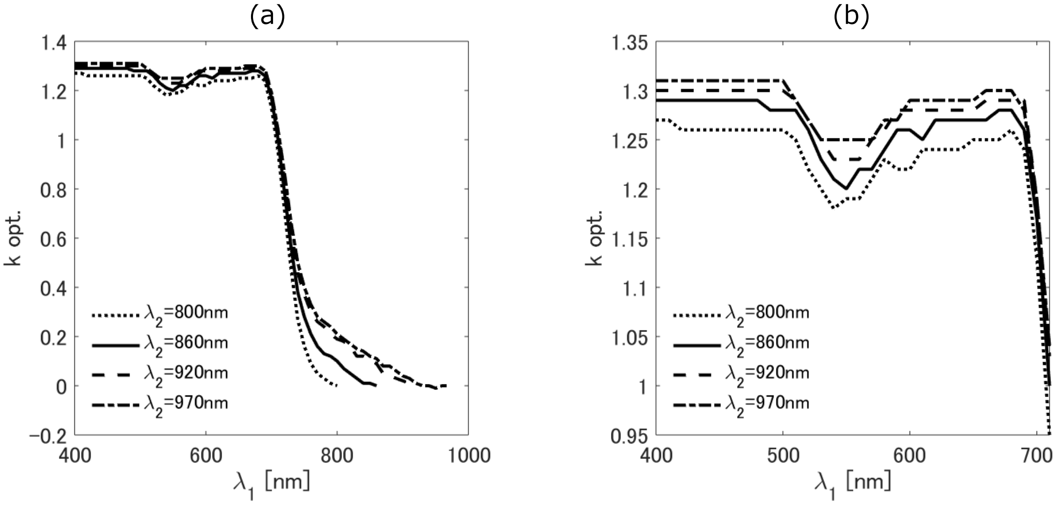

Figure 4.3: k_{opt} as a function of λ_1 for four λ_2(800, 860, 920, and 970 nm).

located at more than 1000 nm.

There were relationships between k_{opt} and TOC reflectance values that depends on the pair of wavelengths. k_{opt} was greater than 1 when TOC reflectances for λ_2 was greater than that for λ_1. Such case appears when λ_1 and λ_2 correspond to visible and NIR bands, respectively. For example, Fig.4.5(a) and 4.5(b) show TOC reflectances for various LAI on bright and dark soils, respectively, and reflectances for visible bands were much lower than NIR bands. On contrary, k_{opt} was less than 0 when TOC reflectances for λ_2 was less than that for λ_1. k_{opt} fell in 0-1 when TOC reflectances of two wavelengths were similar.

4.4.2 Comparison of errors in three vegetation isolines

Accuracies of three vegetation isoline equations, i.e., first-order, asymmetric-order, and optimized asymmetric-order vegetation isoline equations were evaluated. Comparisons of the accuracy were performed based on the averaged value of the $\epsilon(k)$ computed using the 216 conditions for each wavelength pair. The averaged value of the $\epsilon(k)$ is called ‘mean epsilon’.

Figure 4.6 shows the mean epsilon as a function of λ_1 and λ_2 for first-order, asymmetric-order, and optimized asymmetric-order (4.6a, 4.6b, and 4.6c). The mean epsilon of asymmetric-order vegatation isoline equation was smaller than fist-order vegataion isoline equation when λ_1 fell in 400-710 nm and λ_2 fell in 710-1200 nm. In contrast, the mean epsilon of asymmetric-order vegatation isoline equation was greater than fist-order vegataion isoline equation for the case that both λ_1 and λ_2

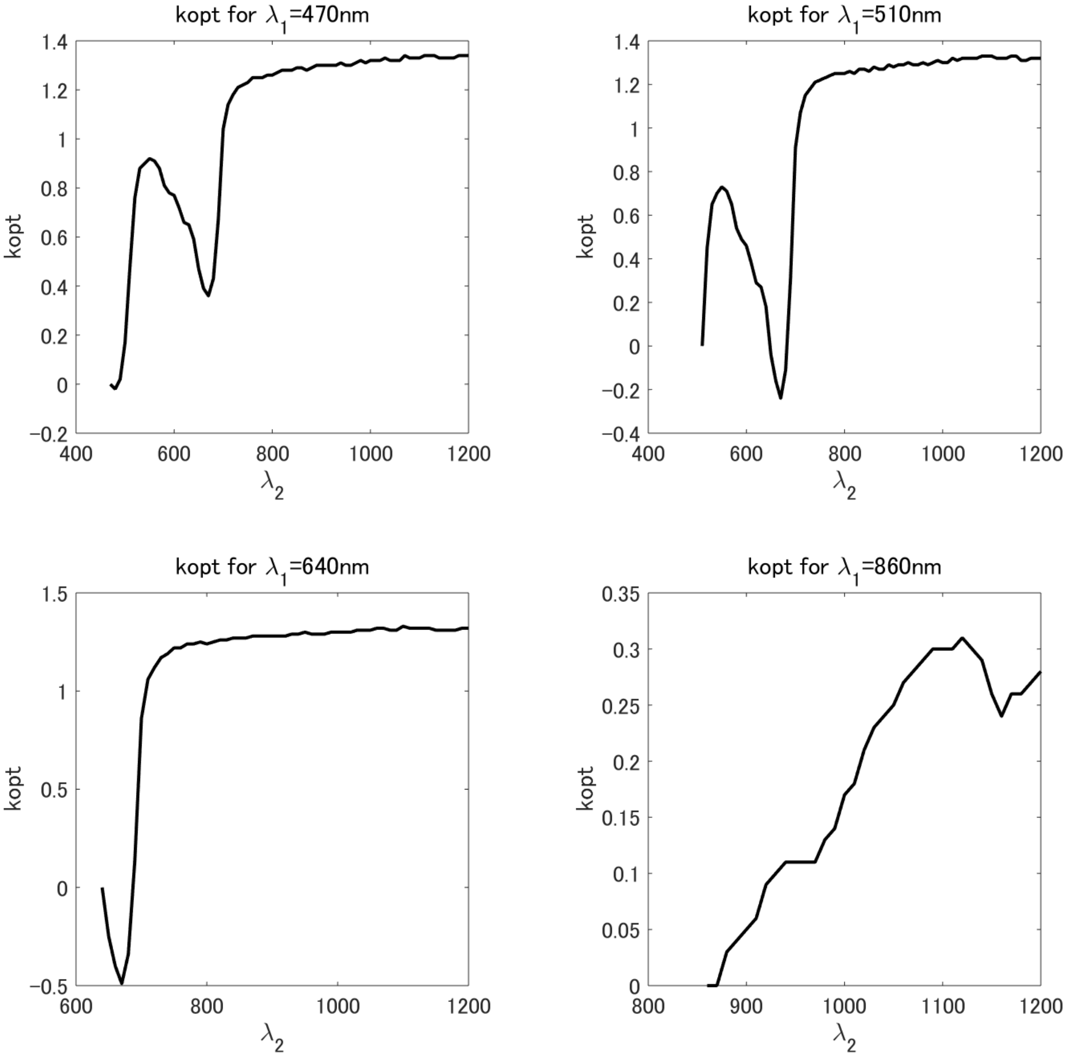

Figure 4.4: k_{opt} as a function of λ_2 for four λ_1 (470, 510, 640, and 860 nm).

fell in 720-1200 nm. The mean epsilon of asymmetric-order isoline equation was approximately equal to that of the first-order isoline equation when both λ_1 and λ_2 fell in 400-700 nm. The optimized asymmetric-order vegetation isoline equation resulted in that mean epsilon is less than 0.001 and much smaller than that of other two isoline equations for all the pair of wavelength.

The mean epsilons of three isolines were directly compared for the wavelength pairs of nearly continuous λ_1's (10 nm increments) and four λ_2's. Figure 4.7 shows plots of the mean epsilon for the pair of four λ_2's (800, 860, 920, and 970 nm) and λ_1 (400 nm-λ_2 with 10 nm increments). The mean epsilon of first-order isoline equation was greater than other isoline equations when λ_1 was less than approximately 700

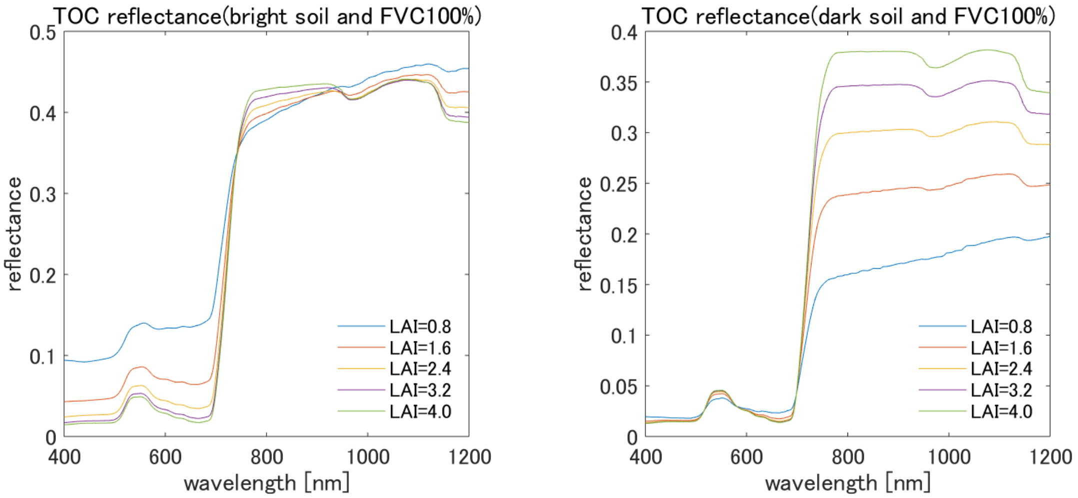

Figure 4.5: Top-of-canopy (TOC) reclectances for various LAI for bright soil (a) and dark soil (b).

nm for four λ_2's. However, the smaller the difference between λ_1 band and λ_2 band ($\lambda_1 > 700$ nm), first-order vegetation isoline error decrease. The mean epsilon of first-order isoline equation showed smaller values than that of asymmetric-order isoline equation when λ_1 was greater than approximately 750 nm. The mean epsilon of asymmetric-order vegetation isoline equation showed 2.0-3.0$\times 10^{-4}$ for $\lambda_1 < 700$ nm but the mean epsilon increased rapidly for $\lambda_1 > 700$ nm. The optimized asymmetric-order vegetation isoline resulted in smallest values of the mean epsilon for the pair of four λ_2's and λ_1 (400 nm-λ_2). These results indicate that superiority among first- and asymmetric-order isoline equations depends on the pair of wavelength and that optimized asymmetric-order isoline equations was most accurate among three isoline equations.

The accuracy of three isoline equations for the pair of four λ_1's and nearly continuous λ_2's was evaluated in Fig. 4.8. The figure shows plots of the mean epsilon along λ_2 for four λ_1's ,460, 510, 640, 860 nm, respectively. The mean epsilon of three isolines was close to 0 when λ_1 corresponds to the visible band and λ_2 was less than about 700 nm (Fig4.8(a), 4.8(b), and 4.8(c)) while the mean epsilon showed increasing trends until about 1100 nm when λ_2 was greater than 700 nm where the mean epsilon of first-order isoline was greatest among three isolines, followed by asymmetric-order isolines and optimized asymmetric-order ones. The mean epsilon of asymmetric-order isoline equation, however, showed the largest mean epsilon among three isolines when λ_1 is 860 nm (Fig.4.8(d)).

4.4.3 On the inverse proportion of the number of higher order terms and the accuracy of vegetation isoline equations

The results in Fig.4.7 indicated that first-order isoline equations could be more accurate than asymmetric-order isoline equations in specific pairs of wavelength. The reason for this unexpected results is carefully investigated here.

Figure 4.9 shows true vegetation isoline and spectra predicted by three vegetation isoline equations over λ_1 and λ_2 band reflectance space. The wavelengths of 860 nm was employed for λ_2. λ_1 used in Fig.4.9 was 690, 710, 730, and 850 nm, respectively. The wavelength used for λ_1 in plot located in lower right in Fig. 4.9 was λ_2 minus 10 nm. The wavelengths for λ_1 (690, 710, 730, and λ_2 minus 10 nm) were chosen based on results in Fig.4.7(b) where first-order isoline showed large errors at about 670 nm, asymmetric-order isoline showed smallest errors at 710 nm, first- and asymmetric-order isolines showed similar level of errors at 730 nm, and first-order isoline showed smallest errors at λ_2 minus 10 nm. LAI and FVC values used in simulations for Fig. 4.9 were 1.6 and 1.0, respectively. Blue circles in Fig.4.9 depict first-order isoline equation, red dashed line depicts asymmetric-order isoline equation, green cross depicts optimized asymmetric-order isoline equation, and black line is the true spectrum. Figure 4.9(a) indicates that accuracy of asymmetric-order vegetation isoline is higher than first-order vegetation isoline, since the asymmetric one is closer to true isoline. The asymmetric-order isoline in Fig.4.9(b) was much closer to true one relative to that in Fig.4.9(a). However, spectra approximated by asymmetric-order isoline exceeded true isoline in Fig.4.9(c) and the distance between true isoline and asymmetric-order isoline was almost identical to distance between true isoline and first-order isoline. The distance between true isoline and asymmetric-order isoline become larger and first-order isoline was likely described on true isoline in Fig.4.9(d). The shifting trends of asymmetric- and first-order isolines indicates that isoline equations that includes higher-order terms asymmetrically were not necessarily accurate and that higher-order terms in vegetation isoline could over-correct the errors in some pair of wavelength. In other words, including the higher-order terms asymmetrically can shift ρ_{λ_2} upper direction more than necessary (this fact can be more clearly understood in Fig.4.10.) The optimized asymmetric-order isoline, however, showed most accurate results among three isolines, that is, the isoline was closest to true isoline for four cases in Fig.4.9. It implies that k_{opt} in the optimized asymmetric-order isoline worked properly for correcting errors in the vegetation isoline equation for any pair of wavelength.

4.5 Conclusions

Numerical simulations were conducted for characterizing k_{opt} included in optimized asymmetric-order isoline equations as well as evaluations of accuracy for first-order, asymmetric-order, and optimized asymmetric-order isoline equations using various pairs of wavelength spanning between 400 nm and 1200 nm.

The factor k added in asymmetric-order isoline equations was simulated using various conditions for each pair of wavelength, and its optimum value, k_{opt} was computed for each wavelength pair. The value of k_{opt} depended on the wavelength pair, but the value was not necessarily unique to the pair. In general, there exist relationships between k_{opt} and characteristics of reflectances of two bands. k_{opt} was greater than 1 when reflectances of λ_2 was greater than that of λ_1, k_{opt} fell between 0 and 1 when reflelctances of λ_1 and λ_2 were nearly identical, and k_{opt} was less than 0 when reflectances of λ_2 was less than that of λ_1.

The optimized asymmetric-order isoline equation was most accurate among three isoline equations for all the wavelength pairs evaluated in this study. The asymmetric-order isoline equation, in general, showed accurate results relative to the first-order isolin equation, but the relation was not observed in specific pairs of wavelength; for example, asymmetric-order isoline equation was more accurate than first-order isoline equation when reflectances for λ_2 were greater than that of λ_1. However, the asymmetric-order isoline equation was not necessarily superior to the first-order isoline equation when reflectances of two bands were mostly identical. This could be caused by the effects of over-correction term that is only included in λ_2 band.

Further investigation of k_{opt} and accuracy assessment of isoline equations are required by expanding conditions of numerical simulations and for evaluating potential utilities of the optimized asymmetric isoline equations on inter-sensor calibration of VI as well as inversion of biophysical retrievals in future works.

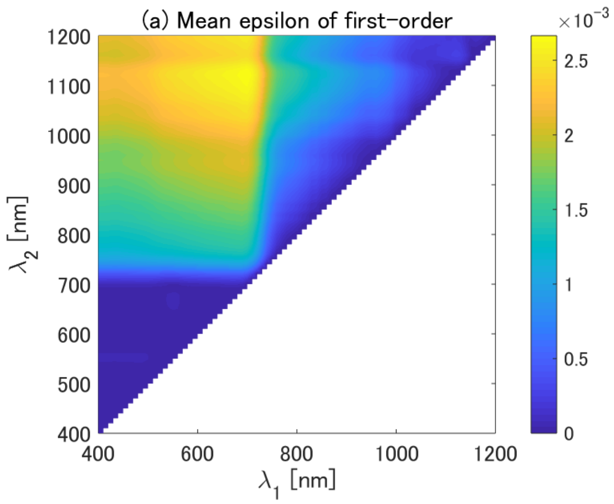

(a) Mean epsilon of first-order

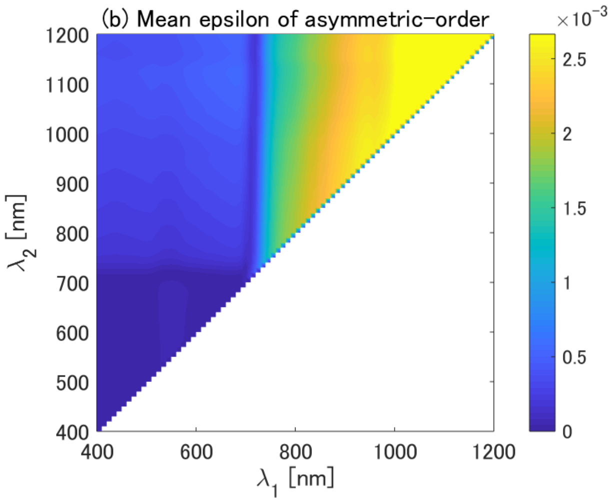

(b) Mean epsilon of asymmetric-order

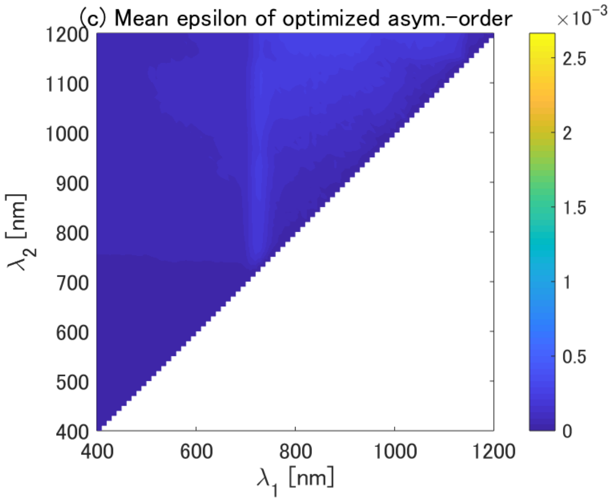

(c) Mean epsilon of optimized asym.-order

Figure 4.6: Mean epsilon for (a) first-order, (b) asymmetric-order, and (c) optimized asymmetric-order isoline equations (ϵ $(k = 0)$, ϵ $(k = 1)$, and ϵ $(k = k_{opt})$) as a function of λ_1 and λ_2.

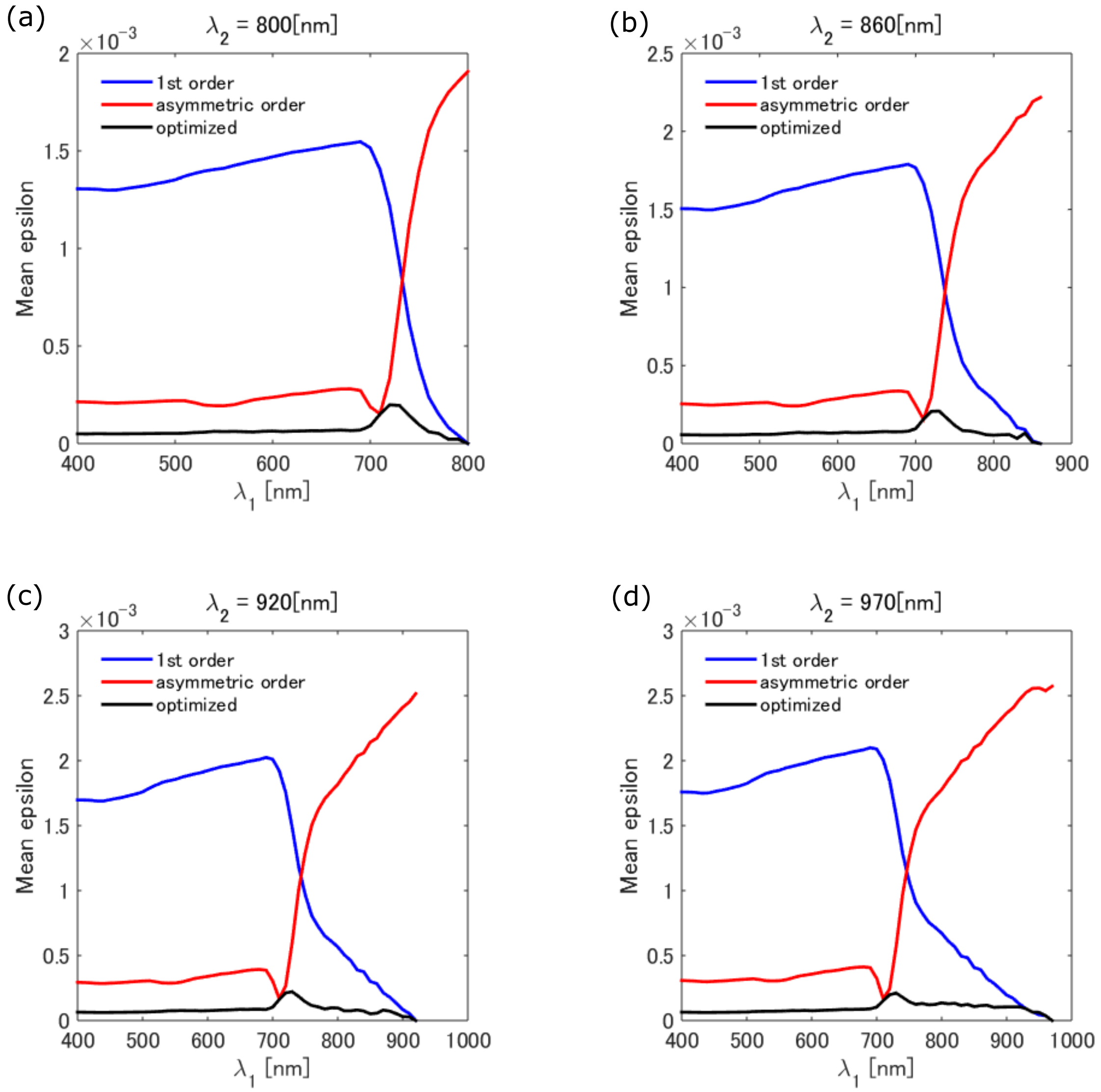

Figure 4.7: Plot of mean epsilon for first-order, asymmetric-order, and optimized asymmetric-order isoline equations (ϵ $(k = 0)$, ϵ $(k = 1)$, and ϵ $(k = k_{opt})$) as a function of λ_1 for four λ_2's ((a) 800 nm, (b) 860 nm, (c) 920 nm, (d) 970 nm).

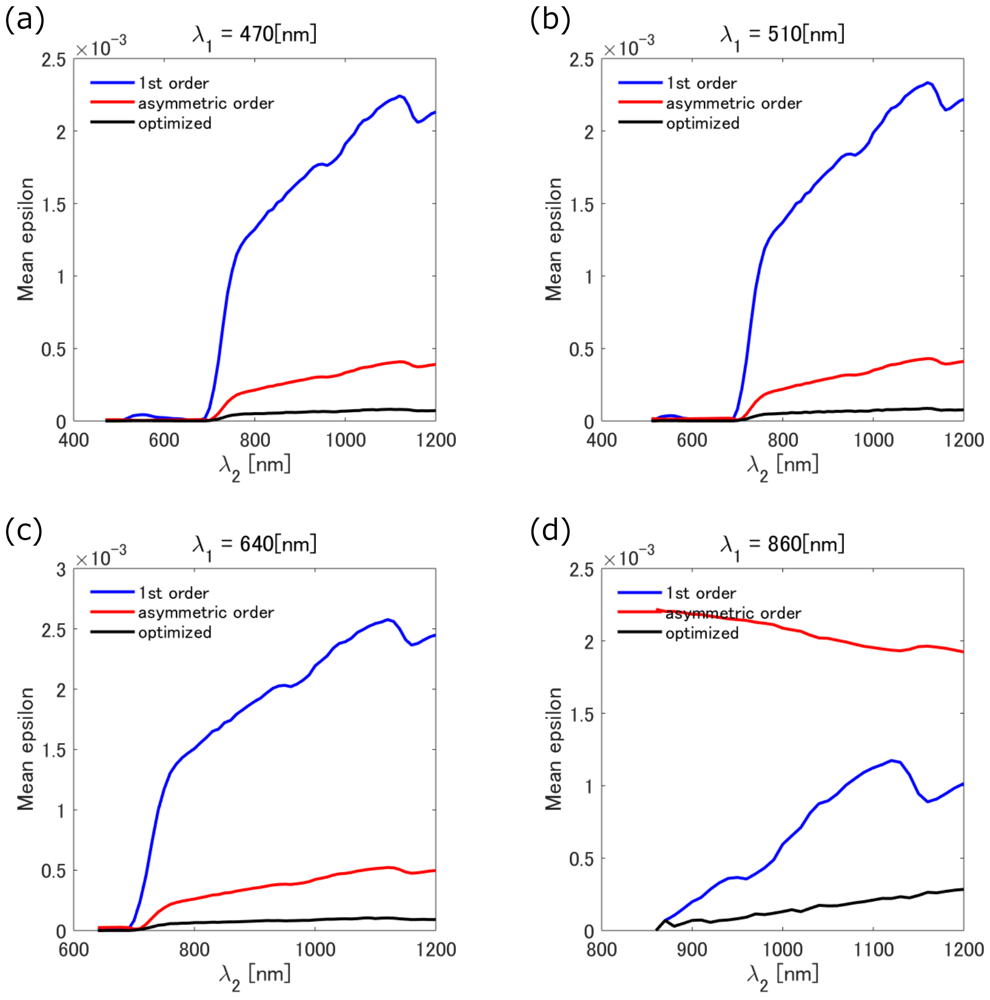

Figure 4.8: Plot of mean epsilon for first-order, asymmetric-order, and optimized asymmetric-order isoline equations (ϵ $(k = 0)$, ϵ $(k = 1)$, and ϵ $(k = k_{opt})$) as a function of λ_2 for four λ_1's ((a) 460 nm, (b) 510 nm, (c) 640 nm, (d) 860 nm).

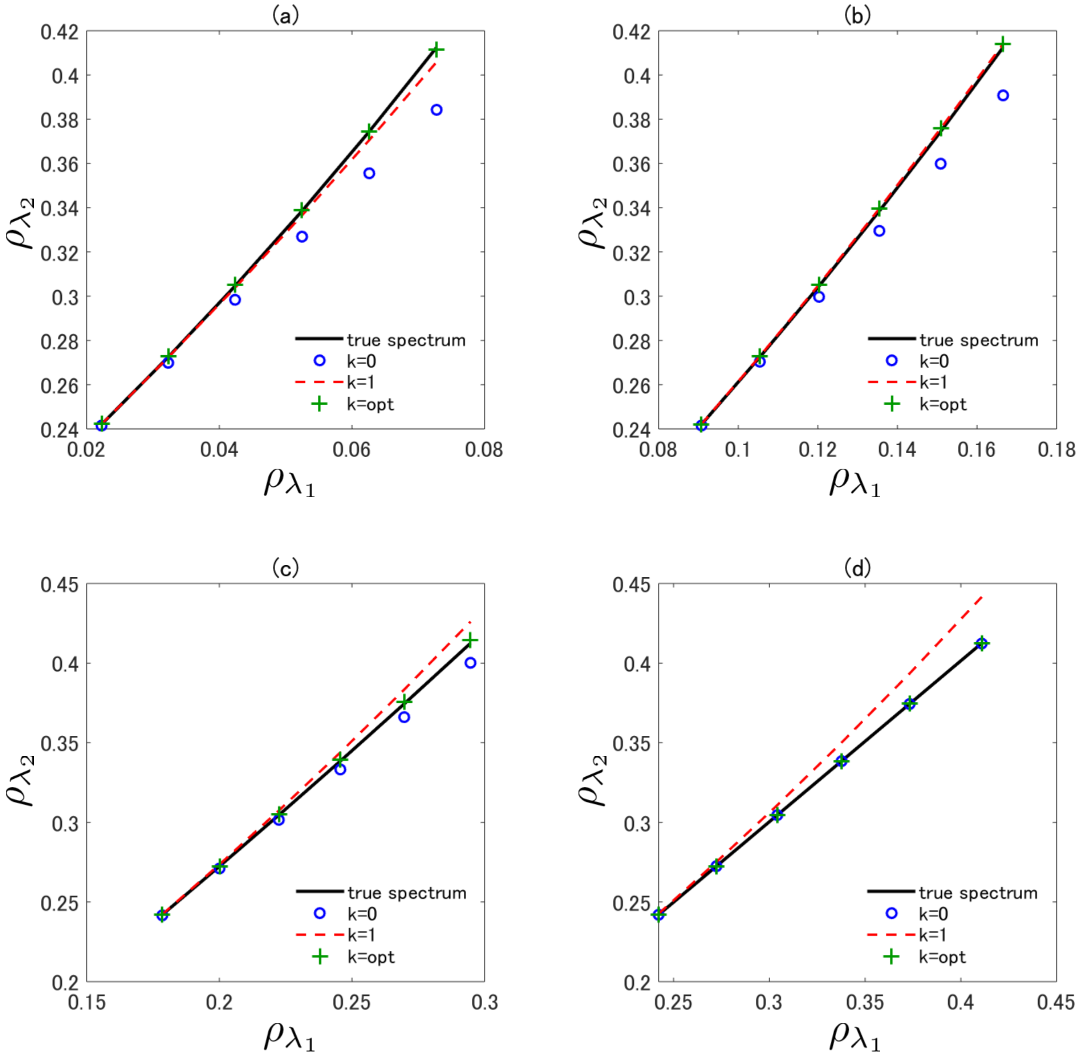

Figure 4.9: Plot of the true spectrum, first-order, asymmetric-order, and optimized asymmetric-order vegetation isoline equations, in which λ_2 is 860nm, and λ_1 are 690, 710, 730, and λ_2 minus 10 nm, respectively ((a), (b), (c), and (d)).

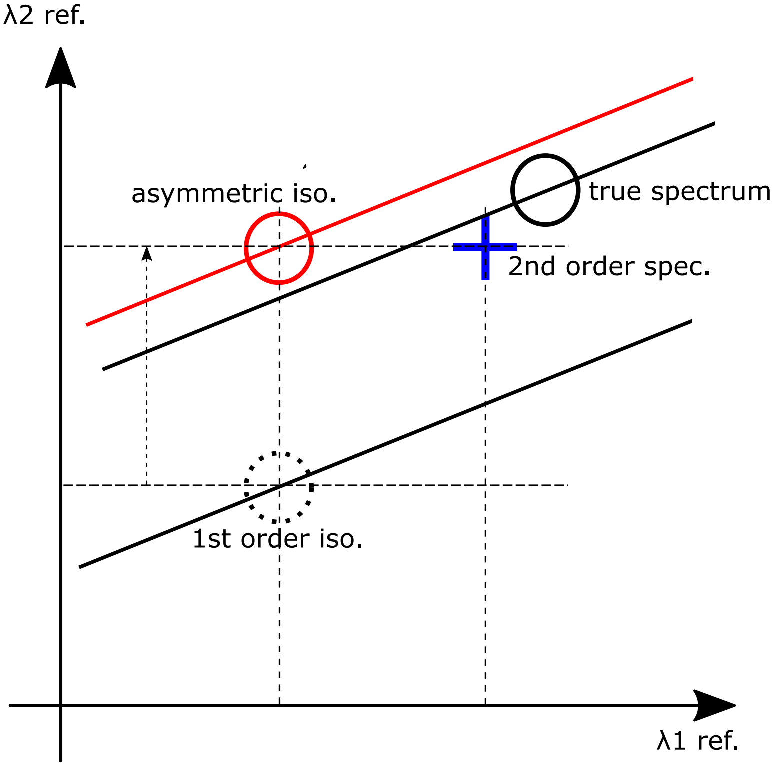

Figure 4.10: Outline on mechanisms of over-correction of asymmetric-order vegetation isoline equation.

CHAPTER V

Conclusions

This study attempted accuracy improvement of vegetation isoline equations which represent a relationship between reflectances of two distinctive wavelengths. Original form of the isoline equation was derived by assuming a single interaction of photon between the canopy and soil layer. The major external influence that causes variations of reflectance spectra is soil brightness underneath the canopy layer. This influence was considered, during the derivation, in terms of soil line which is a well-known concept and hence used frequently to model soil spectral variation in this field of study. The derived relationship was named as the first-order approximated vegetation isoline equation.

The first-order vegetation isoline is simple as a form which is considered as a strong advantage of the formulation. This advantage is resulted from the truncation of the second- and the higher- order interaction terms: The derived form of vegetation isoline equation becomes linear. Although the first-order form has attracted researchers in its applications of various purposes, the accuracy of the isoline equation is known to be deteriorated when the soil brightness becomes high. This relatively large error prevented us from further use of the derived expression when the accuracy requirement of such applications is higher than the error of the derived isoline. Note that the same order of truncation was applied for both red and NIR wavelength during this derivation. Since the truncation order is the same for both wavelengths, we considered this truncation as ‘symmetric’ approximation.

Again, the accuracy loss is due to the truncation of higher-order interaction terms. This study tried to improve the accuracy of the vegetation isolines by including higher-order interaction terms, while maintaining its simplicity of the derived expression. Since the simplicity and accuracy improvement are trade-off, it was a challenging theme to achieve both high accuracy and simplicity at the same time. This study overcame this difficulty by analyzing the mechanism of how the errors of vegetation isolines was brought by truncation of the higher-order interaction terms. The analyses implied an important fact that the spectral shift caused by the truncation is not symmetric. In other words, the accuracy of vegetation isoline may be improved by truncating the higher-order interaction term 'asymmetrically' instead of retaining the same order of interaction terms for both wavelengths. This study explored this fundamental insight both analytically and numerically.

This study set the first objective to derive a new vegetation isoline equation which is higher accuracy than that of the first-order approximation. The accuracy improvement was achieved by including the second-order interaction term only in the NIR wavelength. By doing so, the accuracy was dramatically improved while retaining its simplicity in the analytical form. The derived formula becomes quadratic instead of linear. The errors of the asymmetric-order vegetation isoline equation were reduced to 20% of the value obtained from the first-order vegetation isoline equation. In Chapter II, the derivation steps of the asymmetric-order vegetation isoline equation were explained precisely. Its accuracy improvement was also confirmed by conducting a series of numerical simulations. In this Chapter, we concluded that the vegetation isoline equations can be improved by truncating the higher-order interaction terms asymmetrically.

In Chapter III, the focus of this study was shifted forward to further improvement of the derived asymmetric-order vegetation isoline to meet a standard accuracy requirement. In general, an accuracy requirement that is posed to satellite data products is considered based on signal-to-noise ratio (SNR) of designated sensors. Although the asymmetric-order vegetation isoline shows better accuracy than the first-order ones, it is still greater than the errors compared to SNR of existing sensors. In order to achieve these criteria, a single factor was introduced in the asymmetric-order vegetation isoline. Then, the factor was optimized numerically with the canopy radiative transfer model over certain ranges of biophysical parameters and soil brightness. As a result, it was confirmed that the error in the asymmetric-order vegetation isoline is dramatically reduced by optimizing the factor over the parameter ranges. Specifically, the error obtained from optimized asymmetric-order vegetation isoline equation was reduced to 4% and 22% of the values obtained from first-order vegetation isoline and asymmetric-order vegetation isoline, respectively. Compared with the numerical goal set in chapter III, improved accuracy was confirmed all the condition and compared with SNR of typical multi spectral sensor, it was found that the accuracy of optimized asymmetric-order vegetation isoline equation exceeds SN ratios. It was concluded that use of a single factor appropriately can raise the accuracy of the isoline high enough to meet the general accuracy requirement of satellite data products.

All the numerical validations and discussion up to Chapter III have been carried out only for the specific pair of wavelengths: one from the red (655 nm) and the other from the NIR (865 nm) wavelength. This limitation was attempted to extended in Chapter IV. The wavelength range considered in this chapter was from 400 nm to 1200 nm. This study investigated how the optimized factor (k_{opt}) varies as the selection of wavelength changes. The results of numerical experiments showed that the optimized factor changes nicely to minimize the errors induced in the asymmetric-order vegetation isoline. Furthermore, the results showed that its error is smaller than the errors before the optimization for the entire wavelength range considered in this study. It was confirmed that the optimized asymmetric-order vegetation isoline equation meets the general accuracy requirement of satellite data products for any wavelength combinations.

This study derived an asymmetric-order vegetation isoline equations and also showed optimization technique by introducing a single factor. It was also showed that the introduced technique can also be applicable to the wide wavelength range. Overall, this study concluded that the derived asymmetric-order vegetation isoline equation meets accuracy requirements of broad applications and also applicable to the wide range of wavelength. Use of the derived isoline equation in a context of biophysical parameter retrieval remains undone, which needs to be explored in the future to further confirm its accuracy improvement at the level of satellite data product.

BIBLIOGRAPHY

BIBLIOGRAPHY

[1] 環境省, “IPCC第5次評価報告書の概要-第1作業部会(自然科学的根拠)[2014年12月改訂],” 2014.

[2] T. F. Stocker, D. Qin, G.-K. Plattner, M. Tignor, S. K. Allen, J. Boschung, A. Nauels, Y. Xia, V. Bex, P. M. Midgley *et al.*, “Climate change 2013: The physical science basis,” 2013.

[3] C. B. Field, *Climate change 2014–Impacts, adaptation and vulnerability: Regional aspects.* Cambridge University Press, 2014.

[4] 環境省, “IPCC第5次評価報告書の概要-第2作業部会(影響・適応・脆弱性)[2014年12月改定],” 2014.

[5] 環境省, “IPCC第5次評価報告書の概要-第3作業部会(気候変動の緩和)[2015年4月改定],” 2015.

[6] 第6期地球観測推進部会, “今後10年の我が国の地球観測方針 第4章課題解決型の地球観測,” 2015.

[7] D. Zhu, K. Xiong, H. Xiao, and J. Lan, “Comparison of rocky desertification detection ability of GF-1 and Landsat-OLI based on vegetation index” (in Chinese),” *J. Nat. Resour.*, vol. 31, no. 11, pp. 1949–1957, 2016.

[8] XQ. Wei, XF. Gu, QY. Meng, T. Yu, K. Jia, YL. Zhan, and CM. Wang, “Cross-comparative analysis of GF-1 wide field view and Landsat-7 Enhanced Thematic Mapper plus data,” *Journal of Applied Spectroscopy*, vol. 84, no. 5, pp. 829–836, 2017.

[9] B. Zhong, A. Yang, S. Wu, J. Li, S. Liu, and Q. Liu, “Cross-calibration of reflective bands of major moderate resolution remotely sensed data,” *Remote Sensing of Environment*, vol. 204, pp. 412–423, 2018.

[10] C. Yu, D. Liu, and X. Yang, “Comparisons of band reflectance and normalized difference vegetation index between FY-3A/MERSI and Terra/MODIS,” *J. North-East Forestry Univ.*, vol. 40, no. 9, pp. 124–127, 2012.

[11] M. Ge, J. Zhao, B. Zhong, and A. Yang, “Comparison of the vegetation indexes between FY-3/VIRR FY-3/MERSI and EOS/MODIS data,” *Remote Sens. Technol. Appl.*, vol. 32, no. 2, pp. 262–273, 2017.

[12] R. Feng, R. Ji, J. Wu, Y. Zhang, H. Wang, P. Chen, W. Yu, and S. Zhang, “Analysis on difference between FY3/MERSI-NDVI and EOS/MODIS-NDVI,” *Chin. Agricult. Sci. Bull. Bejing*, vol. 26, pp. 359–362, 2010.

[13] X. Zhang and Q. Tian, “Comparison of spectral characteristics between EO-1 ALI and IRS-P6 LISS-III imagery,” *Current Science*, pp. 954–960, 2015.

[14] N. Singh, K. Chaudhari, and K. Manjunath, “Comparison of citrus orchard inventory using LISS-III and LISS-IV data,” in *Multispectral, Hyperspectral, and Ultraspectral Remote Sensing Technology, Techniques and Applications VI*, vol. 9880. SPIE, 2016, pp. 557–564.

[15] C. Rao, J. Malleswara Rao, A. Senthil Kumar, B. Lakshmi, and V. Dadhwal, “Expansion of LISS III swath using AWiFS wider swath data and contourlet coefficients learning,” *GIScience and Remote Sensing*, vol. 52, no. 1, pp. 78–93, 2015.

[16] N. Phongaksorn, N. K. Tripathi, S. Kumar, and P. Soni, “Inter-sensor comparison between THEOS and Landsat 5 TM data in a study of two crops related to biofuel in Thailand,” *Remote Sensing*, vol. 4, no. 2, pp. 354–376, 2012.

[17] 高橋幸弘, “超小型衛星プラットフォームと液晶スペクトルカメラ,” 計測と制御, vol. 55, no. 9, pp. 792–796, 2016.

[18] 文部科学省 研究開発局宇宙開発利用課, “宇宙開発利用 地球観測衛星,” 2014.

[19] Z. Zhu, J. Bi, Y. Pan, S. Ganguly, A. Anav, L. Xu, A. Samanta, S. Piao, R. Nemani, and R. Myneni, “Global data sets of vegetation leaf area index (LAI) 3g and fraction of photosynthetically active radiation (FPAR) 3g derived from global inventory modeling and mapping studies (GIMMS) normalized difference vegetation index (NDVI3g) for the period 1981 to 2011,” *Remote Sensing*, vol. 5, no. 2, pp. 927–948, 2013.

[20] A. Bannari, D. Morin, F. Bonn, and A. Huete, “A review of vegetation indices,” *Remote Sensing Reviews*, vol. 13, no. 1-2, pp. 95–120, 1995.

[21] C. J. Tucker, “Red and photographic infrared linear combinations for monitoring vegetation,” *Remote Sensing of Environment*, vol. 8, no. 2, pp. 127–150, 1979.

[22] J. E. Colwell, “Vegetation canopy reflectance,” *Remote Sensing of Environment*, vol. 3, no. 3, pp. 175–183, 1974.

[23] A. Huete, “A soil-adjusted vegetation index,” *Remote Sensing of Environment*, 1988.

[24] F. Baret, G. Guyot, and D. Major, “TSAVI: a vegetation index which minimizes soil brightness effects on LAI and APAR estimation,” in *12th Canadian*

Symposium on Remote Sensing Geoscience and Remote Sensing Symposium. IEEE, 1989, pp. 1355–1358.

[25] J. Qi, A. Chehbouni, A. Huete, Y. Kerr, and S. Sorooshian, "A modified soil adjusted vegetation index," *Remote Sensing of Environment*, vol. 48, no. 2, pp. 119–126, 1994.

[26] Y. J. Kaufman and D. Tanre, "Atmospherically resistant vegetation index (ARVI) for EOS-MODIS," *IEEE Transactions on Geoscience and Remote Sensing*, vol. 30, no. 2, pp. 261–270, 1992.

[27] R. Houborg, H. Soegaard, and E. Boegh, "Combining vegetation index and model inversion methods for the extraction of key vegetation biophysical parameters using Terra and Aqua MODIS reflectance data," *Remote Sensing of Environment*, vol. 106, no. 1, pp. 39–58, 2007.

[28] S. Jacquemoud, F. Baret, B. Andrieu, F. Danson, and K. Jaggard, "Extraction of vegetation biophysical parameters by inversion of the PROSPECT+ SAIL models on sugar beet canopy reflectance data. application to TM and AVIRIS sensors," *Remote Sensing of Environment*, vol. 52, no. 3, pp. 163–172, 1995.

[29] D. Kimes, Y. Knyazikhin, J. Privette, A. Abuelgasim, and F. Gao, "Inversion methods for physically-based models," *Remote Sensing Reviews*, vol. 18, no. 2-4, pp. 381–439, 2000.

[30] A. Kallel, S. Le Hégarat-Mascle, C. Ottlé, and L. Hubert-Moy, "Determination of vegetation cover fraction by inversion of a four-parameter model based on isoline parametrization," *Remote Sensing of Environment*, vol. 111, no. 4, pp. 553–566, 2007.

[31] A. Huete, R. Jackson, and D. Post, "Spectral response of a plant canopy with different soil backgrounds," *Remote Sensing of Environment*, vol. 17, no. 1, pp. 37–53, 1985.

[32] A. Huete and R. Jackson, "Suitability of spectral indices for evaluating vegetation characteristics on arid rangelands," *Remote Sensing of Environment*, vol. 23, no. 2, pp. 213–IN8, 1987.

[33] A. Huete, "Soil-dependent spectral response in a developing plant canopy," *Agronomy Journal*, vol. 79, no. 1, pp. 61–68, 1987.

[34] M. M. Verstraete and B. Pinty, "Designing optimal spectral indexes for remote sensing applications," *IEEE Transactions on Geoscience and Remote Sensing*, vol. 34, no. 5, pp. 1254–1265, 1996.

[35] M. Gilabert, J. González-Piqueras, F. Garcıa-Haro, and J. Meliá, "A generalized soil-adjusted vegetation index," *Remote Sensing of Environment*, vol. 82, no. 2, pp. 303–310, 2002.

[36] Z. Jiang, A. R. Huete, J. Li, and J. Qi, "Interpretation of the modified soil-adjusted vegetation index isolines in red-NIR reflectance space," *Journal of Applied Remote Sensing*, vol. 1, no. 1, p. 013503, 2007.

[37] H. Yoshioka, A. R. Huete, and T. Miura, "Derivation of vegetation isoline equations in red-NIR reflectance space," *IEEE Transactions on Geoscience and Remote Sensing*, vol. 38, no. 2, pp. 838–848, 2000.

[38] A. P. Trishchenko, J. Cihlar, and Z. Li, "Effects of spectral response function on surface reflectance and NDVI measured with moderate resolution satellite sensors," *Remote Sensing of Environment*, vol. 81, no. 1, pp. 1–18, 2002.

[39] A. A. Gitelson and Y. J. Kaufman, "MODIS NDVI optimization to fit the AVHRR data series-spectral considerations," *Remote Sensing of Environment*, vol. 66, no. 3, pp. 343–350, 1998.

[40] B.-C. Gao, "A practical method for simulating AVHRR-consistent NDVI data series using narrow MODIS channels in the 0.5-1.0 μm spectral range," *IEEE transactions on Geoscience and Remote Sensing*, vol. 38, no. 4, pp. 1969–1975, 2000.

[41] H. Yoshioka, T. Miura, and K. Obata, "Derivation of relationships between spectral vegetation indices from multiple sensors based on vegetation isolines," *Remote Sensing*, vol. 4, no. 3, pp. 583–597, 2012.

[42] K. Obata, T. Miura, H. Yoshioka, and A. R. Huete, "Derivation of a MODIS-compatible enhanced vegetation index from visible infrared imaging radiometer suite spectral reflectances using vegetation isoline equations," *Journal of Applied Remote Sensing*, vol. 7, no. 1, pp. 073467, 2013.

[43] X. Fan and Y. Liu, "Multisensor normalized difference vegetation index intercalibration: A comprehensive overview of the causes of and solutions for multisensor differences," *IEEE Geoscience and Remote Sensing Magazine*, vol. 6, no. 4, pp. 23–45, 2018.

[44] K. Okuda, K. Taniguchi, M. Miura, K. Obata, and H. Yoshioka, "Application of vegetation isoline equations for simultaneous retrieval of leaf area index and leaf chlorophyll content using reflectance of red edge band," in *SPIE Optical Engineering+ Applications*. International Society for Optics and Photonics, 2016, pp.87–93.

[45] J. Qin, S. Liang, X. Li, and J. Wang, "Development of the adjoint model of a canopy radiative transfer model for sensitivity study and inversion of leaf area index," *IEEE Transactions on Geoscience and Remote Sensing*, vol. 46, no. 7, pp. 2028–2037, 2008.

[46] D. Major, F. Baret, and G. Guyot, "A ratio vegetation index adjusted for soil brightness," *International Journal of Remote Sensing*, vol. 11, no. 5, pp. 727–740, 1990.

[47] Z. Jiang, A. R. Huete, K. Didan, and T. Miura, "Development of a two-band enhanced vegetation index without a blue band," *Remote Sensing of Environment*, vol. 112, no. 10, pp. 3833–3845, 2008.

[48] R. B. Myneni, S. Hoffman, Y. Knyazikhin, J. Privette, J. Glassy, Y. Tian, Y. Wang, X. Song, Y. Zhang, G. Smith *et al.*, "Global products of vegetation leaf area and fraction absorbed PAR from year one of MODIS data," *Remote Sensing of Environment*, vol. 83, no. 1-2, pp. 214–231, 2002.

[49] R. Darvishzadeh, A. Skidmore, M. Schlerf, and C. Atzberger, "Inversion of a radiative transfer model for estimating vegetation LAI and chlorophyll in a heterogeneous grassland," *Remote Sensing of Environment*, vol. 112, no. 5, pp. 2592–2604, 2008.

[50] J. A. Smith, "LAI inversion using a back-propagation neural network trained with a multiple scattering model," *IEEE Transactions on Geoscience and Remote Sensing*, vol. 31, no. 5, pp. 1102–1106, 1993.

[51] C. Bacour, F. Baret, D. Béal, M. Weiss, and K. Pavageau, "Neural network estimation of LAI, fAPAR, fCover and LAI× Cab, from top of canopy MERIS reflectance data: Principles and validation," *Remote Sensing of Environment*, vol. 105, no. 4, pp. 313–325, 2006.

[52] F. Baret, O. Hagolle, B. Geiger, P. Bicheron, B. Miras, M. Huc, B. Berthelot, F. Niño, M. Weiss, O. Samain *et al.*, "LAI, fAPAR and fCover CYCLOPES global products derived from VEGETATION: Part 1: Principles of the algorithm," *Remote Sensing of Environment*, vol. 110, no. 3, pp. 275–286, 2007.

[53] R. B. Myneni, R. Ramakrishna, R. Nemani, and S. W. Running, "Estimation of global leaf area index and absorbed PAR using radiative transfer models," *IEEE Transactions on Geoscience and Remote Sensing*, vol. 35, no. 6, pp. 1380–1393, 1997.

[54] Y. Knyazikhin, J. Martonchik, R. B. Myneni, D. Diner, and S. W. Running, "Synergistic algorithm for estimating vegetation canopy leaf area index and fraction of absorbed photosynthetically active radiation from MODIS and MISR data," *Journal of Geophysical Research: Atmospheres*, vol. 103, no. D24, pp. 32 257–32 275, 1998.

[55] R. D. Jackson and A. R. Huete, "Interpreting vegetation indices," *Preventive Veterinary Medicine*, vol. 11, no. 3-4, pp. 185–200, 1991.

[56] F. Baret and G. Guyot, "Potentials and limits of vegetation indices for LAI and APAR assessment," *Remote Sensing of Environment*, vol. 35, no. 2, pp. 161–173, 1991.

[57] M. M. Verstraete, B. Pinty, and R. B. Myneni, "Potential and limitations of information extraction on the terrestrial biosphere from satellite remote sensing," *Remote Sensing of Environment*, vol. 58, no. 2, pp. 201–214, 1996.

[58] J. Hanes, *Biophysical applications of satellite remote sensing.* Springer Science & Business Media, 2013.

[59] R. Myneni and D. Williams, “On the relationship between FAPAR and NDVI,” *Remote Sensing of Environment*, vol. 49, no. 3, pp. 200–211, 1994.

[60] G. Asrar and G. Asra, *Theory and applications of optical remote sensing.* Wiley New York, 1989.

[61] N. Gobron, B. Pinty, and M. M. Verstraete, “Theoretical limits to the estimation of the leaf area index on the basis of visible and near-infrared remote sensing data,” *IEEE Transactions on Geoscience and Remote Sensing*, vol. 35, no. 6, pp. 1438–1445, 1997.

[62] H. Yoshioka, T. Miura, A. Huete, and B. D. Ganapol, “Analysis of vegetation isolines in red-NIR reflectance space,” *Remote Sensing of Environment*, vol. 74, no. 2, pp. 313–326, 2000.

[63] N. H. Broge and E. Leblanc, “Comparing prediction power and stability of broadband and hyperspectral vegetation indices for estimation of green leaf area index and canopy chlorophyll density,” *Remote Sensing of Environment*, vol. 76, no. 2, pp. 156–172, 2001.

[64] Z. Jiang, A. R. Huete, J. Chen, Y. Chen, J. Li, G. Yan, and X. Zhang, “Analysis of NDVI and scaled difference vegetation index retrievals of vegetation fraction,” *Remote Sensing of Environment*, vol. 101, no. 3, pp. 366–378, 2006.

[65] H. Yoshioka, T. Miura, J. A. Demattê, K. Batchily, and A. R. Huete, “Derivation of soil line influence on two-band vegetation indices and vegetation isolines,” *Remote Sensing*, vol. 1, no. 4, pp. 842–857, 2009.

[66] H. Yoshioka, H. Yamamoto, and T. Miura, “Use of an isoline-based inversion technique to retrieve a leaf area index for inter-sensor calibration of spectral vegetation index,” in *2002 IEEE International Geoscience and Remote Sensing Symposium.* IEEE, 2002, pp. 1639–1641.

[67] H. Yoshioka, T. Miura, and A. R. Huete, “An isoline-based translation technique of spectral vegetation index using EO-1 hyperion data,” *IEEE Transactions on Geoscience and Remote Sensing*, vol. 41, no. 6, pp. 1363–1372, 2003.

[68] H. Yoshioka, “Vegetation isoline equations for an atmosphere-canopy-soil system,” *IEEE Transactions on Geoscience and Remote Sensing*, vol. 42, no. 1, pp. 166–175, 2004.

[69] M. Miura and H. Yoshioka, “Vegetation isoline equations with higher order interaction terms to improve accuracy in retrieval of vegetation biophysical parameters,” in *2008 IEEE International Geoscience and Remote Sensing Symposium.* IEEE, 2008, pp. III–1056.

[70] M. Miura, K. Obata, and H. Yoshioka, "Vegetation isoline equations for analysis of hyper-spectral data with higher order interaction terms," in *2010 IEEE International Geoscience and Remote Sensing Symposium* . IEEE, 2010, pp. 1031–1034.

[71] M. Miura, K. Obata, and H. Yoshioka, "Vegetation isoline equations for atmosphere-canopy-soil system of layer with second order interaction term," in *Remote Sensing and Modeling of Ecosystems for Sustainability VII*, vol. 7809. International Society for Optics and Photonics, 2010, p. 780906.

[72] S. Jacquemoud, W. Verhoef, F. Baret, C. Bacour, P. J. Zarco-Tejada, G. P. Asner, C. François, and S. L. Ustin, "PROSPECT+ SAIL models: A review of use for vegetation characterization," *Remote Sensing of Environment*, vol. 113, pp. S56–S66, 2009.

[73] K. Cooper, J. Smith, and D. Pitts, "Reflectance of a vegetation canopy using the adding method," *Applied Optics*, vol. 21, no. 22, pp. 4112–4118, 1982.

[74] F. Baret, S. Jacquemoud, and J. Hanocq, "The soil line concept in remote sensing," *Remote Sensing Reviews*, vol. 7, no. 1, pp. 65–82, 1993.

[75] S. Jacquemoud and F. Baret, "PROSPECT: A model of leaf optical properties spectra," *Remote Sensing of Environment*, vol. 34, no. 2, pp. 75–91, 1990.

[76] W. Verhoef, "Earth observation modeling based on layer scattering matrices," *Remote Sensing of Environment*, vol. 17, no. 2, pp. 165–178, 1985.

[77] T. Miura and A. Huete, "Performance of three reflectance calibration methods for airborne hyperspectral spectrometer data," *Sensors*, vol. 9, no. 2, pp. 794–813, 2009.

[78] T. Miura, H. Yoshioka, K. Fujiwara, and H. Yamamoto, "Inter-comparison of ASTER and MODIS surface reflectance and vegetation index products for synergistic applications to natural resource monitoring," *Sensors*, vol. 8, no. 4, pp. 2480–2499, 2008.

[79] X. Fan and Y. Liu, "A generalized model for intersensor NDVI calibration and its comparison with regression approaches," *IEEE Transactions on Geoscience and Remote Sensing*, vol. 55, no. 3, pp. 1842–1852, 2016.

[80] M. C. Hansen, P. V. Potapov, R. Moore, M. Hancher, S. Turubanova, A. Tyukavina, D. Thau, S. Stehman, S. Goetz, T. R. Loveland *et al.*, "High-resolution global maps of 21st-century forest cover change," *Science*, vol. 342, no. 6160, pp. 850–853, 2013.

[81] A. Viña, A. A. Gitelson, A. L. Nguy-Robertson, and Y. Peng, "Comparison of different vegetation indices for the remote assessment of green leaf area index of crops," *Remote Sensing of Environment*, vol. 115, no. 12, pp. 3468–3478, 2011.

[82] A. Huete, C. Justice, and H. Liu, "Development of vegetation and soil indices for MODIS-EOS," *Remote Sensing of Environment*, vol. 49, no. 3, pp. 224–234, 1994.

[83] D. Chen, J. Huang, and T. J. Jackson, "Vegetation water content estimation for corn and soybeans using spectral indices derived from MODIS near-and short-wave infrared bands," *Remote Sensing of Environment*, vol. 98, no. 2-3, pp. 225–236, 2005.

[84] B. Matsushita, W. Yang, J. Chen, Y. Onda, and G. Qiu, "Sensitivity of the enhanced vegetation index (EVI) and normalized difference vegetation index (NDVI) to topographic effects: a case study in high-density cypress forest," *Sensors*, vol. 7, no. 11, pp. 2636–2651, 2007.

[85] M. Miura, K. Obata, and H. Yoshioka, "Vegetation isoline equations with first- and second-order interaction terms for modeling a canopy-soil system of layers in the red and near-infrared reflectance space," *Journal of Applied Remote Sensing*, vol. 9, no. 1, p. 095987, 2015.

[86] K. Obata, T. Miura, H. Yoshioka, A. Huete, and M. Vargas, "Spectral cross-calibration of VIIRS enhanced vegetation index with MODIS: A case study using year-long global data," *Remote Sensing*, vol. 8, no. 1, p. 34, 2016.

[87] W. Verhoef, "Light scattering by leaf layers with application to canopy reflectance modeling: the SAIL model," *Remote Sensing of Environment*, vol. 16, no. 2, pp. 125–141, 1984.

[88] C. O. Justice, E. Vermote, J. R. Townshend, R. Defries, D. P. Roy, D. K. Hall, V. V. Salomonson, J. L. Privette, G. Riggs, A. Strahler *et al.*, "The moderate resolution imaging spectroradiometer (MODIS): Land remote sensing for global change research," *IEEE Transactions on Geoscience and Remote Sensing*, vol. 36, no. 4, pp. 1228–1249, 1998.

[89] D. P. Roy, M. A. Wulder, T. R. Loveland, C. Woodcock, R. G. Allen, M. C. Anderson, D. Helder, J. R. Irons, D. M. Johnson, R. Kennedy *et al.*, "Landsat-8: Science and product vision for terrestrial global change research," *Remote Sensing of Environment*, vol. 145, pp. 154–172, 2014.

[90] T. Yokota, Y. Yoshida, N. Eguchi, Y. Ota, T. Tanaka, H. Watanabe, and S. Maksyutov, "Global concentrations of CO2 and CH4 retrieved from GOSAT: First preliminary results," *SOLA*, vol. 5, pp. 160–163, 2009.

[91] C. Cao, J. Xiong, S. Blonski, Q. Liu, S. Uprety, X. Shao, Y. Bai, and F. Weng, "Suomi NPP VIIRS sensor data record verification, validation, and long-term performance monitoring," *Journal of Geophysical Research: Atmospheres*, vol. 118, no. 20, pp. 11–664, 2013.

[92] X. Xiong, J. Sun, X. Xie, W. L. Barnes, and V. V. Salomonson, “On-orbit calibration and performance of Aqua MODIS reflective solar bands,” *IEEE Transactions on Geoscience and Remote Sensing*, vol. 48, no. 1, pp. 535–546, 2009.

[93] R. Morfitt, J. Barsi, R. Levy, B. Markham, E. Micijevic, L. Ong, P. Scaramuzza, and K. Vanderwerff, “Landsat-8 operational land imager (OLI) radiometric performance on-orbit,” *Remote Sensing*, vol. 7, no. 2, pp. 2208–2237, 2015.

[94] S. Fukuda, T. Nakajima, H. Takenaka, A. Higurashi, N. Kikuchi, T. Y. Nakajima, and H. Ishida, “New approaches to removing cloud shadows and evaluating the 380 nm surface reflectance for improved aerosol optical thickness retrievals from the GOSAT/TANSO-Cloud and Aerosol Imager,” *Journal of Geophysical Research: Atmospheres*, vol. 118, no. 24, pp. 13–520, 2013.

[95] X. Xiong, J. Butler, K. Chiang, B. Efremova, J. Fulbright, N. Lei, J. McIntire, H. Oudrari, J. Sun, Z. Wang *et al.*, “VIIRS on-orbit calibration methodology and performance,” *Journal of Geophysical Research: Atmospheres*, vol. 119, no. 9, pp. 5065–5078, 2014.

[96] M. Miura, K. Obata, K. Taniguchi, and H. Yoshioka, “Improved accuracy of the asymmetric second-order vegetation isoline equation over the red–NIR reflectance space,” *Sensors*, vol. 17, no. 3, p. 450, 2017.

[97] A. Iwasaki, N. Ohgi, J. Tanii, T. Kawashima, and H. Inada, “Hyperspectral imager suite (HISUI)-japanese hyper-multi spectral radiometer,” in *2011 IEEE International Geoscience and Remote Sensing Symposium.* IEEE, 2011, pp. 1025–1028.

[98] K. Obata, S. Tsuchida, I. Nagatani, H. Yamamoto, T. Kouyama, Y. Yamada, Y. Yamaguchi, and J. Ishii, “An overview of ISS HISUI hyperspectral imager radiometric calibration,” in *2016 IEEE International Geoscience and Remote Sensing Symposium.* IEEE, 2016, pp. 1924–1927.

[99] T. Matsunaga, A. Iwasaki, S. Tsuchida, K. Iwao, R. Nakamura, H. Yamamoto, S. Kato, K. Obata, O. Kashimura, J. Tanii *et al.*, “HISUI status toward FY2019 launch,” in *2018 IEEE International Geoscience and Remote Sensing Symposium.* IEEE, 2018, pp. 160–163.

[100] K. Obata, “Sensitivity analysis method for spectral band adjustment between hyperspectral sensors: A case study using the CLARREO Pathfinder and HISUI,” *Remote Sensing*, vol. 11, no. 11, p. 1367, 2019.

[101] M. Miura, K. Obata, K. Taniguchi, and H. Yoshioka, “Optimization technique of asymmetric-order vegetation isoline equations,” in *2017 IEEE International Geoscience and Remote Sensing Symposium.* IEEE, 2017, pp. 2923–2926.

LIST OF PUBLICATIONS

Journals

1. M. Miura, K. Obata and H. Yoshioka. "Vegetation isoline equation with first- and second-order interaction terms for modeling a canopy-soil system of layers in red and near-infrared reflectance space," *Journal of Applied Remote Sensing*, 9(1), 095987, November 2015. (Chapter 2)
2. M. Miura, K. Obata, K. Taniguchi and H. Yoshioka. "Improved accuracy in the asymmetric second-order vegetation isoline equation over the red-NIR reflectance space," *Sensors*, 17(3), 450, February 2017. (Chapter 3)

Proceedings(Peer reviewed)

1. M. Miura, K. Obata, K. Taniguchi, and H. Yoshioka, "Optimization technique of asymmetric-order vegetation isoline equations," *in 2017 IEEE International Geoscience and Remote Sensing Symposium* , Fort Worth, Texas, USA, July 2017. (Chapter 4)
2. M. Miura, K. Obata and H. Yoshioka, "Vegetation isoline equation for atmosphere-canopy-soil system of layer with second order interaction term," *SPIE Optics+Photonics2010*, 7 pages, San Diego, USA, August 2010. (Chapter 2)
3. M. Miura, K. Obata and H. Yoshioka, "Vegetation isoline equation for analysis of hyper-spectral data with higher order interaction terms," *in 2010 IEEE International Geoscience and Remote Sensing Symposium* , pp.1031-1034, Hawaii, USA, July 2010. (Chapter 4)
4. M. Miura and H. Yoshioka, "Vegetation isoline equation with higher order interaction terms to improve accuracy in retrieval of vegetation biophysical parameter," *in 2008 IEEE International Geoscience and Remote Sensing Symposium* , pp.1056-1059, Boston, USA, July 2008. (Chapter 2)